FRONTIERS OF PHYSICS

TOPICAL REVIEW
Volume 19 / Issue 4 / 42501 / 2024

Twistronics and moiré excitonic physics in van der Waals heterostructures

Siwei Li (李思维)[1], Ke Wei (韦可)[2,†], Qirui Liu (刘祺瑞)[1], Yuxiang Tang (唐宇翔)[2], Tian Jiang (江天)[2,‡]

1 College of Advanced Interdisciplinary Studies, National University of Defense Technology, Changsha 410073, China
2 Institute for Quantum Science and Technology, National University of Defense Technology, Changsha 410073, China
Corresponding authors. E-mail: †weikeaep@163.com, ‡tjiang@nudt.edu.cn
Received August 20, 2023; accepted October 11, 2023

ABSTRACT

Heterostructures composed of two-dimensional van der Waals (vdW) materials allow highly controllable stacking, where interlayer twist angles introduce a continuous degree of freedom to alter the electronic band structures and excitonic physics. Motivated by the discovery of Mott insulating states and superconductivity in magic-angle bilayer graphene, the emerging research fields of "twistronics" and moiré physics have aroused great academic interests in the engineering of optoelectronic properties and the exploration of new quantum phenomena, in which moiré superlattice provides a pathway for the realization of artificial excitonic crystals. Here we systematically summarize the current achievements in twistronics and moiré excitonic physics, with emphasis on the roles of lattice rotational mismatches and atomic registries. Firstly, we review the effects of the interlayer twist on electronic and photonic physics, particularly on exciton properties such as dipole moment and spin-valley polarization, through interlayer interactions and electronic band structures. We also discuss the exciton dynamics in vdW heterostructures with different twist angles, like formation, transport and relaxation processes, whose mechanisms are complicated and still need further investigations. Subsequently, we review the theoretical analysis and experimental observations of moiré superlattice and moiré modulated excitons. Various exotic moiré effects are also shown, including periodic potential, moiré miniband, and varying wave function symmetry, which result in exciton localization, emergent exciton peaks and spatially alternating optical selection rule. We further introduce the expanded properties of moiré systems with external modulation factors such as electric field, doping and strain, showing that moiré lattice is a promising platform with high tunability for optoelectronic applications and in-depth study on frontier physics. Lastly, we focus on the rapidly developing field of correlated electron physics based on the moiré system, which is potentially related to the emerging quantum phenomena.

Keywords moiré superlattice, twistronics, van der Waals heterostructure, moiré exciton, correlated electronic state

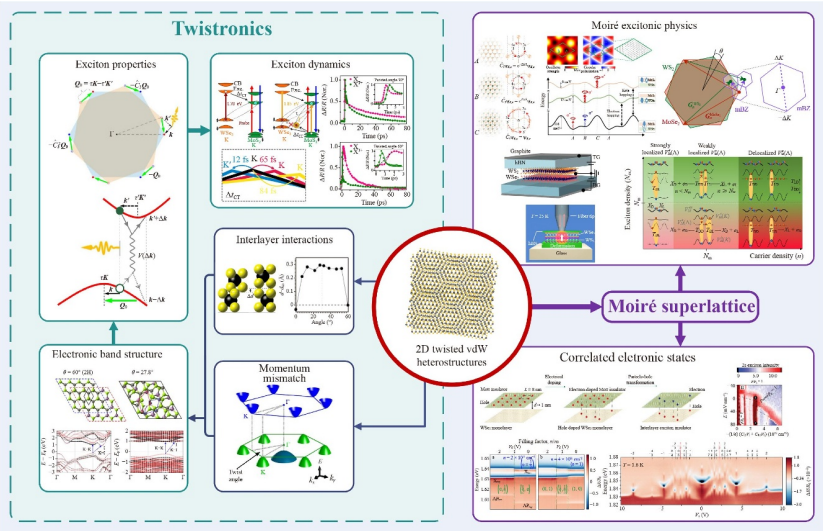

Higher Education Press

*Special Topic: Photophysics in 2D Materials, Heterostructures and Moiré Superlattices (Eds.: Qihua Xiong, Tian Jiang, Luyi Yang & Haiming Zhu).

https://doi.org/10.1007/s11467-023-1355-6

Contents

1 Introduction

Two-dimensional (2D) vdW layered materials [1, 2], including graphene [3, 4], silicene [5], hexagonal boron nitride (hBN) [6, 7], phosphorene [8, 9], and transition metal dichalcogenides (TMDs) [10–12], have aroused wide attention in recent years due to their exotic properties [11, 13] and promising applications in high-performance devices [9, 14–20]. The relatively weak interlayer vdW force enables vdW materials to be exfoliated into atomically thin layers with outstanding physical properties as well as highly adjustable 2D structures [12]. A variety of methods [21, 22] have been shown to efficiently regulate material properties, such as external field [23–26], doping [26–28], strain [29–33], integration with optical microcavity [34], and changing dielectric environment [35–37]. In semiconducting 2D materials, the significantly enhanced Coulomb interactions due to reduced dielectric screening and increased quantum confinement give rise to rich excitonic species, which are formed by tightly bound electron and hole pairs and could persist up to room temperature, showing strong light–matter couplings and many-body effects [38]. Specifically, TMDs possess fascinating optical and electronic properties, embracing widely tunable direct bandgap [39], large oscillator strength [40], substantial exciton binding energy [41], and strong spin–orbit coupling that endows TMDs with spin-valley contrasting physics [42–44]. More importantly, different layered materials can be stacked together through vdW interactions to form various vertical heterostructures or homostructures, leading to enriched physical properties with high flexibility and tunability beyond the simple combination of the constituent monolayers [45, 46]. Consequently, 2D vdW heterostructures offer an excellent platform for exploring modern solid-state physics, such as Bose–Einstein condensation (BEC) [47] and fractional quantum Hall effect [48]. The high adjustability of vdW heterostructures allows customized properties for the new generation of electronic and optoelectronic applications including quantum emitters [49] and excitonic devices [26, 50, 51].

The atomic alignment between the constituent layers of vdW heterostructure changes with interlayer lattice constant mismatch and relative orientation angle. Thus, the twist angle allows continuous modulation of strain distribution, interlayer coupling, electronic band structure and excitonic dynamics due to the incommensurate stacking [38, 52, 53], which prompts a new topic "twistronics" [54] that emphasizes the interplay between lattice rotational mismatch and interlayer electronic coupling. When the incommensurate heterostructures are stacked with a small twist angle or lattice mismatch, the atomic registries will change spatially with large-scale periodicity, forming so-called moiré patterns [49, 55]. Such moiré patterns can be directly observed via nanoscale techniques [56–58] and attract abundant research attention due to the fascinating moiré effects in theoretical predictions. The superlattice structure of moiré pattern can generate strongly correlated phases, such as insulating states [59] and unconventional superconductivities [60] in magic-angle graphene bilayer, and Hofstadter's butterfly pattern in graphene/hBN twisted heterostructure [48, 61]. Recently, TMD vdW heterostructures with moiré superlattice show novel excitonic and optical physics including excitons localized by periodic moiré potentials [62, 63], moiré exciton minibands [64, 65] and spatially modulated optical selection rules [49, 66, 67]. Furthermore, as a highly tunable system, moiré superlattice in vdW heterostructures can be feasibly combined with external factors, which will promote the exploration of frontier physics, including new spin optoelectronics, many-body interactions and potential applications in quantum information processing [49].

Here, we focus on the interlayer-twist-modified electronic and optical physics in semiconducting vdW heterostructures and the burgeoning area of moiré superlattice. This review is organized as follows. In Section 2, we first summarize the optoelectronic properties affected by interlayer twist in vdW heterostructures, including the exciton properties, the electronic band structures and the exciton dynamics. In Section 3, moiré pattern and the emergent superlattice effects in vdW heterostructures are systematically explained. Specifically, we discuss the theoretical analysis and experimental observations of diverse moiré excitons, as well as how the properties of these excitons (localization and spin-valley configuration) are modulated by moiré superlattice. On this basis, the

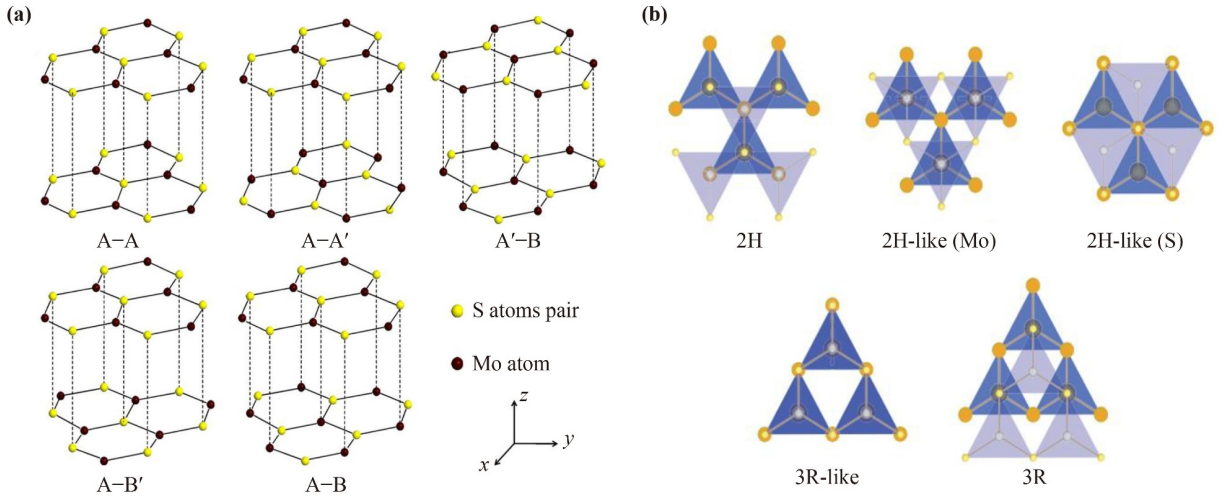

Fig. 1 Schematic diagrams of five typical aligned stacking patterns of bilayer MoS_2. **(a)** Side view and **(b)** Top view of stacking orders with two different kinds of labels, where A–A, A–A′, A′–B, A–B′ and A–B correspond to 3R-like, 2H, 2H-like (Mo), 2H-like (S) and 3R, respectively. One pair of S atoms is denoted by one yellow circle as a concise representation. (a) Reproduced with permission from Ref. [69]. (b) Reproduced with permission from Ref. [77].

influence of external conditions such as electric field, doping, and strain on the moiré system is further discussed. In Section 4, we introduce the recently emerging field of correlated electronic states reported in TMDs-based moiré superlattices that possess several advantages compared with graphene-based twisted bilayers. The conclusions and future outlooks are summarized in Section 5.

2 Twist-angle-tunable optoelectronic properties in van der Waals heterostructure

Early experimental observations on vdW heterostructures have revealed that changing relative orientation angle or lattice mismatch could extend the optical and electronic properties of vdW bilayers. Most of these works focused on bilayers stacked in high-symmetry patterns (Fig. 1), including A–A (point group D_{3h}), A–A′ (point group D_{3d}), A′–B (point group D_{3d}), A–B (point group C_{3v}) and A–B′ (point group D_{3d}) [68]. Then the interlayer twist of bilayer structures is employed to realize continuous tunning, of which excitonic physics is the most concerned [22, 41, 65]. It is theoretically predicted that relative twist between constituent layers can affect the excitonic phenomena and exciton dynamics through interlayer couplings [52] and electronic band structures [46, 68, 69], which has been confirmed and further explored in subsequent experiments [45, 51, 70–86].

2.1 Exciton properties controlled by twist-angle-dependent interlayer interactions

Interlayer coupling in multilayer system depends on the relative positions of atoms between layers. In 2H and 3R patterns [see Fig. 1(b)], Mo and S atoms with opposite charges from different layers are stacked together, resulting in the strongest interlayer coupling. On the contrary, if atoms with the same charge in different layers are stacked together, the Coulomb repulsion between them increases the interlayer distance and reduces the coupling strength, among which the 3R-like pattern exhibits the weakest coupling due to most of the S atoms overlapped [77]. Various theoretical calculations have reported the effects of stacking patterns on interlayer interactions. Early studies mainly focused on the effect of the interlayer distance on coupling strength under different atomic arrangements [68, 69], which can induce tunable optical responses such as Raman [75, 78, 87] and photoluminescence (PL) [51, 77, 88] spectroscopy. Liu *et al.* [69] evaluated the geometries and stabilities of bilayer MoS_2 with five typical stacking patterns using density functional theory (DFT) calculations based on the local density approximation (LDA) function. They found that A–B and A–A′ in Fig. 1(a) had shorter interlayer distances, lower relative energies and higher binding energies compared with the other patterns, as these two patterns exhibited the weakest interlayer repulsive interaction. Using random phase approximation (RPA), He *et al.* [68] studied the binding energy and interlayer spacing of TMD bilayers under different stacking patterns. They found that high symmetry A–A′ (bulklike 2H symmetry) was the most stable type with short interlayer distance, while the A–B stacking (3R type) followed closely behind, ~5 meV/formula unit less stable. The stacking order also affects the valence band splitting and the relative energy of the K point to Γ point, where the exciton binding energy and corresponding optical response are influenced. In the case of incommensurate

bilayer systems (with lattice constant mismatch and/or interlayer twist), numerical calculation for the estimation of interlayer coupling is nontrivial due to the lack of periodic features. For this, Wang *et al.* [52] adopted the analytical effective perturbative treatment to study the interlayer coupling represented by interlayer hopping integral in different valleys in both commensurate and incommensurate TMDCs bilayers. They show that the coupling strengths in ±K valleys are sensitive to the interlayer distance determined by the stacking pattern.

The stacking-dependent interlayer coupling is usually probed by Raman and PL spectra, which indicate the lattice vibration modes and optical transitions of the bilayer structures, respectively. Homojunctions of bilayer TMD with varying twist angles show remarkable modulations of optical transition energies and Raman modes [75]. In stacked MoS_2 bilayer with CVD-grown monolayers, van der Zande and collaborators revealed the twist-angle-controlled strong tunning of the indirect optical transition energy and second-harmonic generation (SHG), as well as the weak tuning of direct optical transition energy and Raman frequency [87], as shown in Fig. 2(a). The shift of indirect optical transition energies was attributed to the angle-dependent interlayer separation due to repulsion between S atoms [see Fig. 2(b)]. The results suggested that the effective interlayer interaction was maximized in the aligned ($\theta = 0°$) or anti-aligned ($\theta = 60°$) conformation, and minimized at $\theta = 30°$. Zheng *et al.* [74] reported the modulations of bandgap structures and phonon vibrations in a CVD-as-grown WS_2 bilayer. These bilayer WS_2 with random twist angles formed at high growth temperatures would exhibit a much stronger PL intensity of peak A and an additional peak A_1 compared with aligned stacking cases ($\theta = 0°$ or $60°$), accompanied with the absence of indirect transition peak I (interlayer exciton) [see Fig. 2(e)]. Such modulations were attributed to two mechanisms. On one hand, a large interlayer distance weakened the coupling strength, which was proved by the broadening and redshift of the out-of-plane A_{1g} mode in Raman spectra. On the other hand, symmetry breaking in the random-twisted bilayers led to a higher possibility of interlayer hoping, which would be suppressed by spin-layer locking in aligned case. Zhang *et al.* [76] also observed an extra peak in PL spectra at 77 K in as-grown MoS_2/WS_2 heterostructure with type II band alignment, which was identified as the recombination of interlayer carriers [see Figs. 2(c) and (d)]. Twisted heterostructures also show angle-tunable Raman modes. Wang *et al.* [78] reported a redshift of A_{1g} by ~2 cm^{-1} in WSe_2/WS_2 bilayer compared with the case of monolayer WSe_2, along with the emergence of a new peak at 309.4 cm^{-1} that was regarded as a general feature for strong coupling in bilayer system. The peak separations between $A_{1g}(\Gamma)$ and $E_{2g}(\Gamma)$ as well as the linewidths of $A_{1g}(\Gamma)$ in WS_2/MoS_2 heterostructures were periodically modulated by twist angles, caused by the interlayer coupling and charge transfer effects [80]. Apart from TMD vdW heterostructures, Raman spectra of bilayer graphene are also affected by interlayer twist [89, 90]. These twist-angle-sensitive Raman peaks demonstrate that the interlayer interactions and lattice dynamics can be regulated by interlayer rotation. Therefore, it is possible to control the electron-phonon coupling strength and thermal transport properties of 2D vdW heterostructures via twist angle [91].

Since the optical responses of 2D semiconducting materials are mostly determined by their excitonic physics, lots of researches on modulations by stacking and twist focus on the excitonic properties [88] and dynamics [78, 79]. Huang *et al.* [88] concentrated on the trions and excitons under varying twist angles between 0° and 120° in the stacked bilayer of CVD-grown MoS_2. In PL spectra, both the ratio of the trion (A^-) to exciton (A) and the trion binding energy showed periodic and oscillatory features as a function of twist angle θ, as shown in Fig. 2(f). These quantities reached their maxima in aligned cases ($\theta = 0°$ or $60°$) and minima at $\theta = 30°$ or $90°$, consistent with the angle-dependent interlayer coupling strength. Using micro-absorption spectroscopy, Wang *et al.* [78] showed that in WSe_2/WS_2 bilayer after annealing, the intralayer WSe_2 A exciton presented significant PL quenching and spectral broadening due to angle-insensitive interlayer charge separation under strong coupling condition, while the interlayer excitons formed by ultrafast interlayer charge transfer exhibit sensitively twist-angle-dependent nature. The PL intensity of the interlayer exciton in $MoSe_2/WSe_2$ heterostructure was enhanced at coherently stacking ($\theta = 0°$ and $60°$) while vanished at incoherent intermediate angles. Utilizing vdW-corrected DFT calculations, Nayak *et al.* [70] found that the states at valence band edges were affected by the twist angle, which exhibited a long tail stretching over another layer in coherently stacked $MoSe_2/WSe_2$, but localized in an individual layer in incoherent case, as shown in Fig. 2(g). The lattice mismatch controlled by twist angle would also significantly affect the properties of devices based on vdW heterostructures. Choi *et al.* [71] fabricated p-WSe_2/n-$MoSe_2$ junctions with $\theta = 0°$, 15° and 30°, and measured their I–V curves under illumination with different wavelengths. In the aligned case ($\theta = 0°$) where strong coupling is acquired, the sample showed a diodelike behavior under dark condition, functioning as a well-established p–n junction and displaying higher sensitivity under IR illumination. Whereas in the cases of lattice mismatch ($\theta = 15°$, 30°), interlayer potential barrier was built due to the vdW gap under weak coupling, and such barrier could be overcome under ultraviolet (UV) illumination, allowing photocurrent to flow in both forward and reverse directions. Apart from rotation mismatch, lattice relaxation and strain distribution of

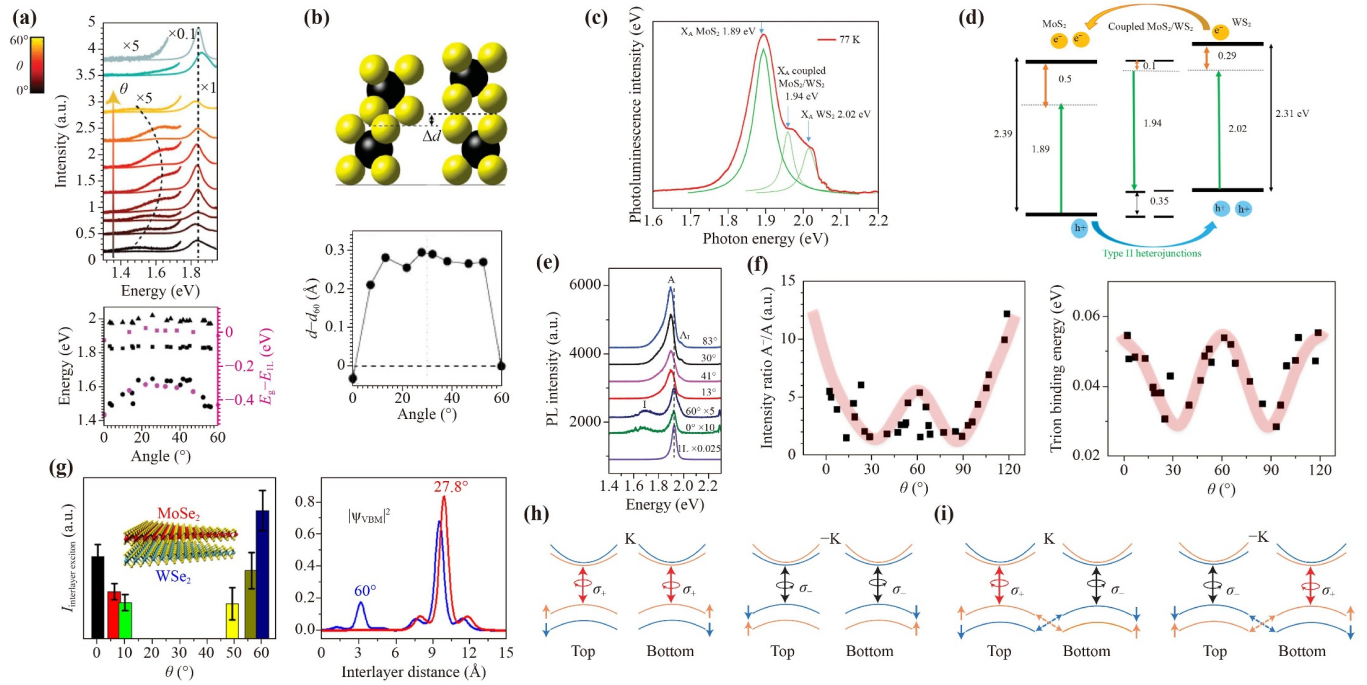

Fig. 2 Experimental observations of stacking-angle modulated interlayer interactions. **(a)** The upper panel shows PL spectroscopy for the bottom (as grown, gray line) and top (transferred, green line) monolayers, as well as twisted bilayers (t-BLs) MoS_2 at various twist angles θ. The lower panel is the measured (black) and simulated (magenta) peak energies versus θ for the indirect (circles), A (squares), and B (triangles) transitions. **(b)** Schematic of the interlayer separation of t-BL MoS_2 depending on the stacking patterns (upper panel) and twisting angle θ (lower panel) relative to the 60° separation. **(c)** PL spectra with the Lorentzian fitting at 77 K. **(d)** The bandgap alignment of coupled as-grown MoS_2/WS_2 heterostructure. The solid black, green, and orange double-arrow lines represent the energy gap, optical gap, and exciton binding energy, respectively. **(e)** PL spectra of the randomly twisted WS_2 bilayer compared with monolayer. **(f)** Twist angle dependence of the trion to exciton PL intensity ratio (left panel) and trion binding energy (right panel). **(g)** The intensity of the interlayer exciton peak versus the twist angle (left panel) and the plane-averaged partial charge density of each band edge state (VBM and CBM at K) versus the interlayer distance for θ = 60° and 27.8° (right panel) of $MoSe_2/WSe_2$ heterostructures. **(h–i)** Scheme of valley and spin polarizations excited by circularly polarized light in bilayers with suppressed (h) interlayer hopping and (i) strong interlayer coupling. (a, b) Reproduced with permission from Ref. [87]. (c, d) Reproduced with permission from Ref. [76]. (e) Reproduced with permission from Ref. [74]. (f) Reproduced with permission from Ref. [88]. (g) Reproduced with permission from Ref. [70]. (h, i) Reproduced with permission from Ref. [77].

vdW twisted bilayers can also influence the formation of excitonic species and consequently the optical responses. Recently, Dai et al. [92] have reported a four-fold enhancement of phonon-assisted photon up-conversion (UPC) in 5.5° twisted WSe_2 bilayer, along with PL intensity reduced by half, which was not observed in bilayers under other rotation angles such as 1.1° and 13.8°. Such UPC enhancement was attributed to the significant lattice relaxation at a mediate twist angle (5.5°) between the relaxed (1.1°) and rigid (13.8°) regimes. This mediate angle would cause increased strain and lattice deformation, leading to considerable interlayer separation. As a result, the formation of indirect interlayer exciton through non-radiative relaxation of direct neutral exciton was suppressed, which increased the UPC efficiency. On the other hand, the reduction of required assisted phonons due to the spectral redshift at the mediate angle also improved the UPC efficiency.

Light with circular polarization can be utilized to manipulate the valley degree of freedom in TMDCs, where the strong spin–orbit coupling (SOC) and the broken inversion symmetry lead to spin-valley-locked excitons at ±K valleys, resulting in the valley contrasting optical selection rule [42–44, 93–96]. The spin-valley-locked excitons can be modulated by external electric [23, 25, 97, 98] and magnetic fields [99], allowing desirable potential applications [16]. In bilayer systems, the valley-contrasting physics can also be regulated by the interlayer coupling and structural symmetry, depending on the stacking orders. Jiang *et al.* [77] fabricated MoS_2 bilayers with different stacking patterns by folding exfoliated monolayers to break the inversion symmetry and suppress interlayer hopping, resulting in strong valley and spin polarizations. Circularly polarized PL spectra showed the different degree of polarization (DOP) for different stacking bilayers, where the DOP in folded bilayers was comparable to that in monolayer, and much higher than that in natural 2H bilayer. The remarkable

DOP of folded bilayers confirmed that the suppression of interlayer hopping and broken inversion symmetry generated spin-valley configuration locked to the layer index. On the contrary, in the centrosymmetric 2H-stacking bilayer, the interlayer hopping amplitude of holes was estimated to be comparable with the SOC strength [100], giving rise to the mixing of layer pseudospins and suppressed valley- and spin-selective circular dichroism, as illustrated in Figs. 2(h) and (i).

2.2 Electronic band structures and relative twist in momentum space

The variety of stacking patterns and relative twist angles between crystal orientations in 2D multilayer system provides a vast realm to modify the electronic band structures through angle- and mismatch-dependent vdW interactions at the atomic level, flourishing novel optoelectronic properties such as spatial- and/or momentum- indirect excitons with twist-angle-tunable nature [72]. Unlike the monolayer TMD possessing a direct bandgap at the K point, bilayer TMD is a bulk-like indirect gap semiconductor. Liu *et al.* [69] used the LDA method to examine the band structures of bilayer MoS_2 with different stacking conformations. The indirect bandgap was found to be determined by the energy levels of K point in the conduction band and Γ point in the valence band. The states at the K point in the conduction band were constitutive of the strongly localized d orbitals at the Mo atom sites (Mo-d), whose double degeneracy remained intact under weak interaction. Whereas, the states at Γ point in the valence band originated from the linear combination of outer p orbitals of the S atom sites (S-p) and internal Mo-d orbitals, so the double level degeneracy at the Γ point was lifted by the stronger interaction between the S-p from different layers, leading to a higher energy level at the Γ point in valence band than that at the K point. Consequently, the band structure transformed from direct bandgap to indirect bandgap. Stronger interlayer coupling would enlarge the splitting at the Γ point in the valence band and lead to a smaller indirect bandgap. Therefore, the direct A-exciton transition was insensitive to the interlayer interaction, while the indirect transition was sensitively dependent on stacking order [77]. To gain a more accurate understanding of the stacking-induced modulation on electronic structures, excitonic effects and optical properties of bilayer TMDs, He *et al.* [68] utilized a many-body framework adopting the RPA and the GW approximation combined with the Bethe-Salpeter equation (BSE). The G_0W_0 quasiparticle band structure was represented by three valleys at T, K and Σ of the conduction band and two valleys at K and Γ of the valence band, as shown in Fig. 3(a). The conduction band minimum (CBM) was always located at the T point, while the valence band maximum (VBM) was related to the stacking pattern and vdW interlayer distance, which is mainly determined by the valence band splitting at K and the energy difference between K and Γ. For A excitons, although their binding energy were sensitive to stacking patterns (about 60–100 meV higher for A–A′ than A–B pattern) the optical transition energies were not significantly dependent on stacking, in accordance with the experimental results [see Fig. 2(a)] [87]. Apart from that, the theoretically predicted stacking-induced strong tunning on Γ valley in the valence band was also demonstrated by the observation of twist-angle-dependent indirect exciton transition.

Electronic structure and optical properties for twist heterostructures have also been well-explored. Jin and coworkers [45] used cathode lens microscopy and microprobe angle-resolved photoemission spectroscopy (μ-ARPES) to realize a direct measurement of the electronic structure in twisted graphene/MoS_2 vdW heterostructures. The observed band structures indicated that the electronic structure of graphene (Gr) remained intact, while the MoS_2-derived band exhibited twist angle dependence, as shown in Figs. 3(b) and (c). In particular, the relative energy between Γ and K decreased from ~0.2 to ~0 eV as the twist angle varied from 5° to 28°, suggesting an indirect bandgap character except for twist angle near 30°. These results showed a similar trend to the DFT calculation prediction, corroborating the view that the electron-transfer-induced strain between graphene and MoS_2 would affect the Mo–S bond and lead to the twist-angle-tunable band structure [101]. In TMD vdW heterostructures, the band structures exhibit direct- or indirect-gap determined by twist angles through tuning the relative energy levels between K and Γ but have robust type II band alignments [see Fig. 5(a)]. For twisted $MoSe_2/WSe_2$, first-principle DFT calculations reveal a tunable band structure shown in Fig. 3(f) [70], where the direct K–K transitions and indirect K–I transitions are almost degenerate, and the conduction band at Γ point varying with twist angle presents a trend similar to that in homostructure TMDs [68, 69]. However, the observed VBM is located at K instead of Γ due to the large SOC. The VBM and CBM at the K-point mainly come from WSe_2 and $MoSe_2$, respectively. Since direct transition possesses a larger amplitude than that of indirect transition which involves with second-order process, the interlayer transitions observed experimentally are expected to occur between band edge states from two different layers at K point with twist-angle-dependence [Fig. 2(g)]. For example, in twisted WSe_2/WS_2 heterostructure, VBM mostly originates from orbitals of the WSe_2 layer, while CBM is mainly contributed by the WS_2 layer. Such strong type-II band alignments are independent of the twist angle and bandgap nature [78]. The spatially indirect nature of interlayer exciton makes its transition dipole smaller than that of the intralayer exciton by one to two magnitudes and consequently weaker oscillator strength [54], which

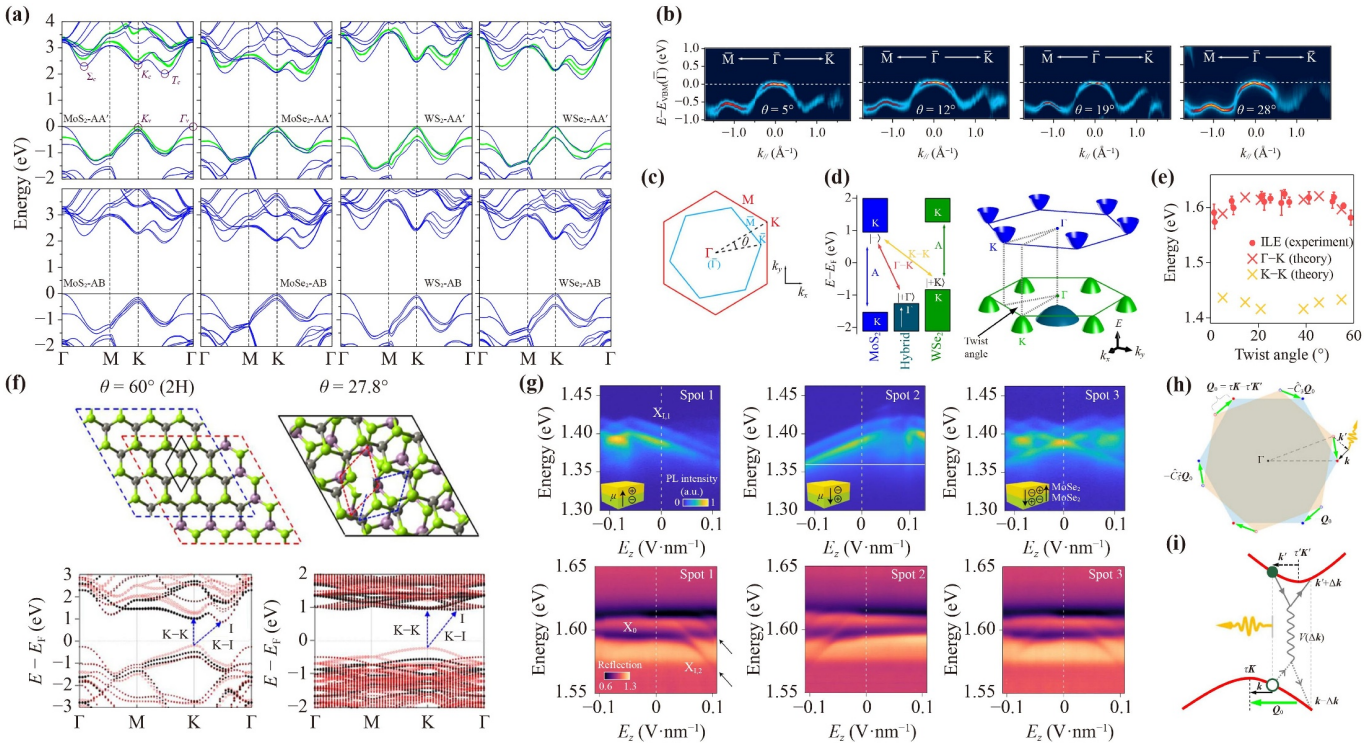

Fig. 3 Electronic structure and optical properties in twist heterostructures. **(a)** Quasiparticle band structure of AA′ and AB stacked bilayer TMDs. The green lines indicate the monolayer band structure. **(b)** Second-derivative plot of the ARPES band map along $\bar{M}$–$\bar{\Gamma}$–$\bar{K}$ of the MoS_2 in Gr/MoS_2 heterostructures under different twist angles. **(c)** Brillouin zone of Gr and surface Brillouin zone of MoS_2 under twist angle θ. **(d)** Scheme of band alignment (left panel) and two-dimensional band structure (right panel) of twisted MoS_2/WSe_2 heterostructure. $|+\Gamma\rangle$ is the hybrid state of both layers and moves up as hybridization increases. **(e)** Measured PL peak energies and calculated transition energies of different interlayer excitons MoS_2/WSe_2 heterostructure with different twist angles. **(f)** Geometries (upper panel) and corresponding DFT-calculated band structures (lower panel) of $MoSe_2$/WSe_2 heterostructures under twist angle $\theta = 60°$ and 27.8°. The contributions of the $MoSe_2$ (black) and WSe_2 (red) layer are denoted in band structures. **(g)** Electric-field-dependent PL spectra of K–Γ interlayer excitons (upper panel) and reflectance spectra of K–K intralayer excitons (lower panel) in different spots of t-BL $MoSe_2$ at 4 K. **(h)** Shifted Brillouin zone corners of two constituent layers under a small twist in TMD heterostructure. The green arrows denote the displacement vector between $\tau\boldsymbol{K}$ and $\tau'\boldsymbol{K}'$ corner. **(i)** An interlayer exciton formed with kinematic momentum Q. The interlayer Coulomb interaction between the electron and the hole conserving their momentum sum is marked by the gray wavy line. (a) Reproduced with permission from Ref. [68]. (b, c) Reproduced with permission from Ref. [45]. (d, e) Reproduced with permission from Ref. [72]. (f) Reproduced with permission from Ref. [70]. (g) Reproduced with permission from Ref. [82]. (h, i) Reproduced with permission from Ref. [46].

has been theoretically predicted [46, 65] and experimentally demonstrated [18, 78].

Such type II band alignment can easily promote the formation of interlayer exciton in which electrons and holes reside at K valleys from different layers. The electron and hole valleys of interlayer excitons will shift away from each other under a small twist and/or lattice mismatch, leading to a momentum mismatch of the Brillouin zone, shown in Fig. 3(h). The exciton's kinematic momentum is defined as $\boldsymbol{Q} \equiv \boldsymbol{k'} + \boldsymbol{k}$, where $\boldsymbol{k'}$ and $\boldsymbol{k}$ represent kinematic momentum of carriers from different layers, as shown in Fig. 3(i). The transition dipole of interlayer excitons is sensitive to $\boldsymbol{Q}$, forming sixfold degenerate light cones at finite center-of-mass (COM) velocities on the parabolic energy dispersion [46]. The so-called "light cone" means the region for allowed inter-conversion with photons in the exciton phase-space. When the electrons and holes relax to the bottom of the $\pm\boldsymbol{K}$ valleys in momentum space with $\boldsymbol{Q} = 0$, their transitions must involve phonon or impurity scattering to enter the finite-velocity light cones, resulting in long lifetimes of the interlayer excitons due to this inefficiency scattering process [102]. However, when the small mismatch can be compensated by the exciton's kinematic momentum $\boldsymbol{Q} = \pm\boldsymbol{Q}_0, \pm\hat{C}_3\boldsymbol{Q}_0, \pm\hat{C}_3^2\boldsymbol{Q}_0$, direct transition for radiative recombination is allowed. Here, $\boldsymbol{Q}_0 \equiv \tau\boldsymbol{K} - \tau'\boldsymbol{K'}$ represents the displacement from the Brillouin zone corner $\tau'\boldsymbol{K'}$ of one constituent layer to the nearest Brillouin zone corner $\tau\boldsymbol{K}$ of the other layer, where (τ, τ') denotes the electron-hole valley configuration. Such interlayer excitons are within the light cones, whose transition dipole strength would decay rapidly

with an increase in the magnitude of momentum. Only in commensurate stacking at $\theta = 0°$ or 60° with negligible lattice mismatch, all the main and Umklapp light cones can merge into a single cone at $\boldsymbol{Q} = 0$ and get close enough to the bottom of energy dispersion, leading to strong interlayer exciton PL [46, 103].

Unlike the interlayer excitons with spatially separated electron and hole both located at K valleys, Kunstmann and co-workers [72] have identified a new type of interlayer excitons in MoS_2/WSe_2 heterostructure, where the hole and the electron reside at the hybridized Γ valley and localized K valley, respectively, as shown in Figs. 3(d) and (e). This momentum-space indirect interlayer exciton was revealed by combining temperature-dependent PL spectroscopy and first-principle calculations. The emission energy of this kind of interlayer excitons could be tuned via relative twist by controlling the hybridization [72]. Likewise, Sung *et al.* [82] have also observed and investigated the Γ–K interlayer excitons at temperature $T = 4$ K. These momentum-indirect interlayer excitons possessed opposite out-of-plane electric dipole moments supported by broken mirror and inversion symmetry due to the spatially alternating stacking domains, which originated from atomic reconstruction. The electric dipole moments of Γ–K interlayer excitons were identified by the linear Stark effect in PL spectra, measured in a hexagonal boron nitride (hBN) encapsulated near-0°-twisted $MoSe_2$ bilayer under an out-of-plane electric field, as shown in Fig. 3(g). Additionally, K–K intralayer excitons with higher energy were also observed, which exhibited field-asymmetric hybridization with interlayer K–K excitons under large fields, manifesting as field-dependent avoided crossings between the two corresponding peaks in reflectance spectra [Fig. 3(g)]. The electric field dependence of these K–K interlayer excitons also varied spatially under alternating crystal symmetry. This result indicates the profound effects of crystal symmetry on excitonic properties and potentials for realizing alternating exciton arrays with high tunability.

In TMD heterostructures, interlayer excitons with spin-valley polarization inherited from the monolayers can directly interconvert with a photon with elliptic polarization [46, 54]. The interlayer exciton spin-valley polarization originates from valley-polarized intralayer excitons through interlayer charge transfer. Such valley-contrasting physics can be modified by interlayer twist, which can expand fascinating and complicated properties through changing mismatch between the Brillouin zone of constituent layers in momentum space. In exciton momentum space, light cones of interlayer exciton possess helicity determined by valley configurations of electron and hole, which allow tunable resonant optical injection of valley excitons and valley currents under linearly polarized light excitation, as illustrated in Fig. 4(a) [46]. For the commensurate case (i.e., $\theta = 0°$ or 60° with neglectable lattice mismatch ~0.1%) where all light cones merge into a single one at $\boldsymbol{Q} = 0$ and interlayer exciton PL gets enhanced, the brightness and the polarization selection rules depend on the interlayer translation. This interlayer exciton system allows observation of valley Hall and inverse valley Hall effects, which is regarded as an ideal platform to investigate Berry phase effects in the Bloch band [46]. Experimentally, Rivera and collaborators [51] observed interlayer excitons with valley-contrasting physics in $WSe_2/MoSe_2$ vertical heterostructures at near-0° stacking with slight twist and lattice mismatch at room temperature. In this case, the existence of light cones at small kinematic momenta allows interlayer excitons to interconvert with photons and radiatively recombine through scattering such as exciton–phonon or exciton–exciton interactions. Interlayer hopping between valleys with the same electron spin from two constituent layers becomes the dominant relaxation channel under small momentum mismatch, leading to the co-polarized optical selection rules [see Figs. 4(b) and (c)]. Whereas, the interlayer hopping between spin-contrasting valleys is strongly suppressed under large momentum difference. Interlayer exciton exhibits a long valley lifetime of about 40 nanoseconds, a few orders of magnitude longer than that of intralayer excitons in monolayer, enabling the visualization of the valley-polarized interlayer exciton cloud expanding, including lateral drift and diffusion over several micrometers [51]. Therefore, twisted van der Waals heterostructures act as a promising playground for exploring valley exciton physics. In recent years, several works have reported on the chiral optical properties and valley polarization physics in vdW bilayers via twist modulation. Scuri *et al.* [73] controlled the spin-valley properties of interlayer excitons in twisted WSe_2 bilayers encapsulated in hBN by tunning the momentum separation between valleys of different layers [Fig. 4(d)]. The interlayer excitons presented long valley lifetimes (> 40 ns) due to the indirect nature in both real and momentum space [65, 103–106]. Michl *et al.* [83] reported a high degree of intrinsic circular polarization of exciton PL driven by non-resonant linearly polarized laser in nonmagnetic twisted $hBN/MoSe_2/WSe_2$ heterostructure ($\theta = 5.3 \pm 1.4°$) at 1.8 K [Fig. 4(e)], which was attributed to the kinetic spin polarization of excitons arising from new pyromagnetic symmetry of chiral stack structures. Furthermore, it has been predicted theoretically that valley splitting of WSe_2 would be significantly enhanced in twisted WSe_2/CrI_3 heterostructure in contrast to non-twisted heterostructure, which was equivalent to the case with a perpendicular external magnetic field of about 20 T [107].

2.3 Twist-angle-dependent exciton dynamics

Lattice mismatch and relative twist between layers in vdW heterostructures with the ability to modify the interlayer interaction and electronic structure efficiently,

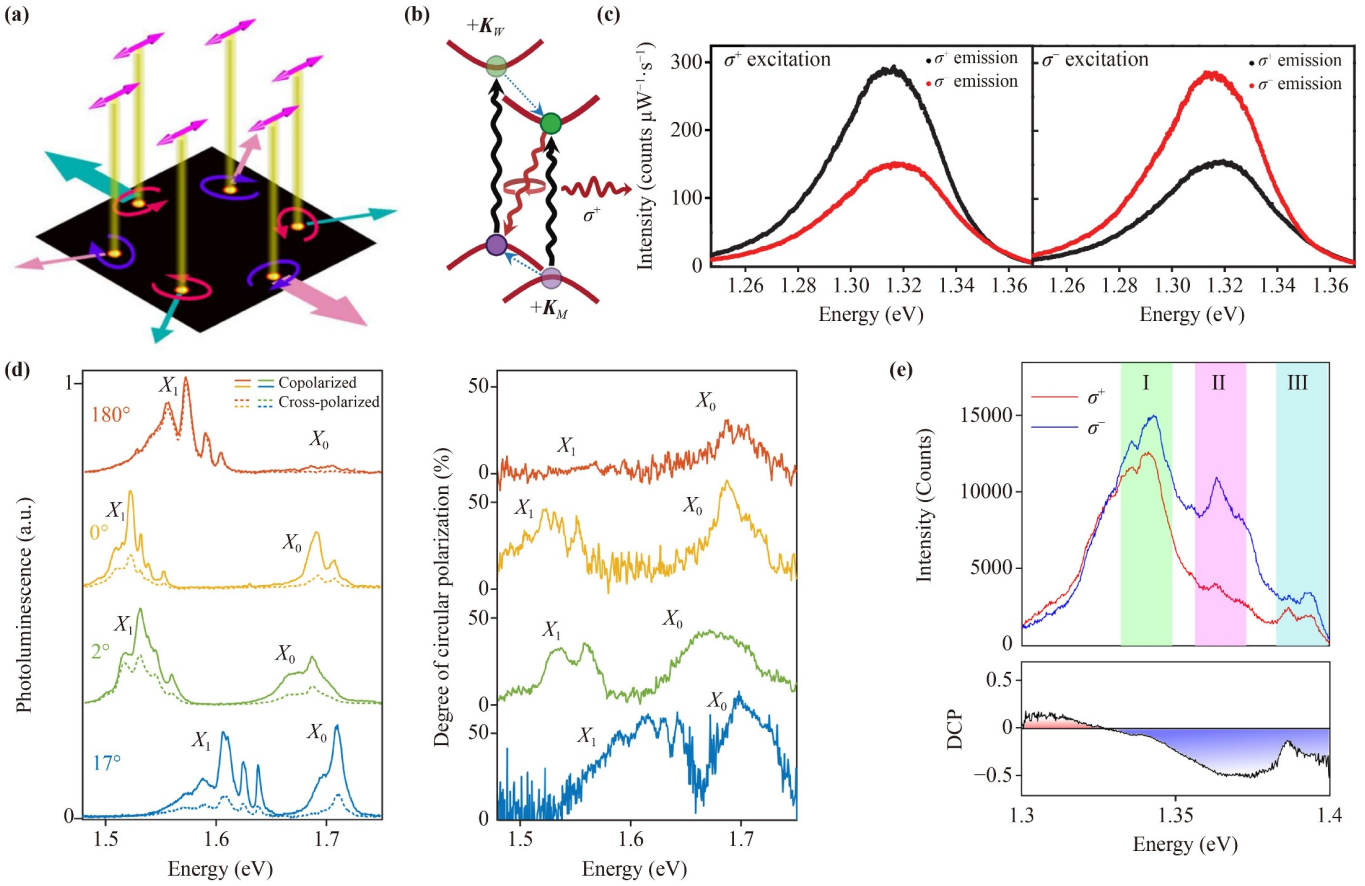

Fig. 4 Spin-valley polarization physics in twisted vdW TMD heterostructure. **(a)** Light cones at finite velocities and injection of pure valley current of excitons by linearly polarized light. Currents of different valleys are denoted by green and pink arrows. **(b)** Schematic of the interlayer excitons in the +K valley. Intralayer excitons are excited by σ^+ polarized optical pump (black wavy lines) and form interlayer excitons in the +K valley through fast interlayer charge transfer (blue dotted arrows). **(c)** Circular polarization-resolved PL spectra of the interlayer exciton performing a strong valley polarization. **(d)** Polarization-resolved PL spectra (left panel) and degree of circular polarization (DOCP) (right panel) of intralayer (X_0) and interlayer (X_I) excitons in WSe_2 bilayers with varying twist angles. **(e)** PL (upper panel) and DOCP (lower panel) of twisted $MoSe_2/WSe_2$ heterostructure under linearly polarized 532-nm laser pump and circular-polarized detection at 1.8 K. The splitting optical resonances are attributed to the moiré excitons. (a) Reproduced with permission from Ref. [46]. (b, c) Reproduced with permission from Ref. [51]. (d) Reproduced with permission from Ref. [73]. (e) Reproduced with permission from Ref. [83].

are supposed to play a key role in exciton dynamics, including ultrafast charge transfer, diffusion, and relaxation processes. With the help of transient spectroscopy such as pump-probe technique, time-resolved SHG and ultrafast electron diffraction (UED), a large range of works have focused on how exciton dynamics in heterostructures are affected by twist angle over these years [52, 78, 79, 84, 85]. Physical properties of semiconductor heterostructures are highly influenced by band alignment, which can be classified into three types, including type-I (straddling gap), type-II (staggered gap) and type-III (broken gap) [108], as depicted in Fig. 5(a). Theoretical calculations have found that the type-II interface band alignment is the most typical and common case for TMD vdW heterostructures [13, 109]. Meanwhile, the type-II band alignment with CBM and VBM of the heterostructures located in different layers supports the electron and hole to transfer to the spatial-separated band edges [see Fig. 5(b)].

Early experiments have demonstrated the rapid interlayer charge transfer (within 100 fs) by various methods such as micro-absorption spectroscopy, PL mapping and femtosecond pump-probe spectroscopy [78, 110]. Such efficient interfacial charge transfer (< 50 fs) dynamics in TMD vdW heterostructures do not exhibit twist-angle dependence [79, 111–113]. Ji *et al.* [79] found the charge transfer in MoS_2/WS_2 heterostructures was robust in a time scale of about 90 fs under varying twist angles with different interlayer coupling strengths, measured by optical two-color ultrafast pump-probe spectroscopy, as shown in Figs. 5(c) and (d). The twist-angle-independent charge transfer with high efficiency violates the common

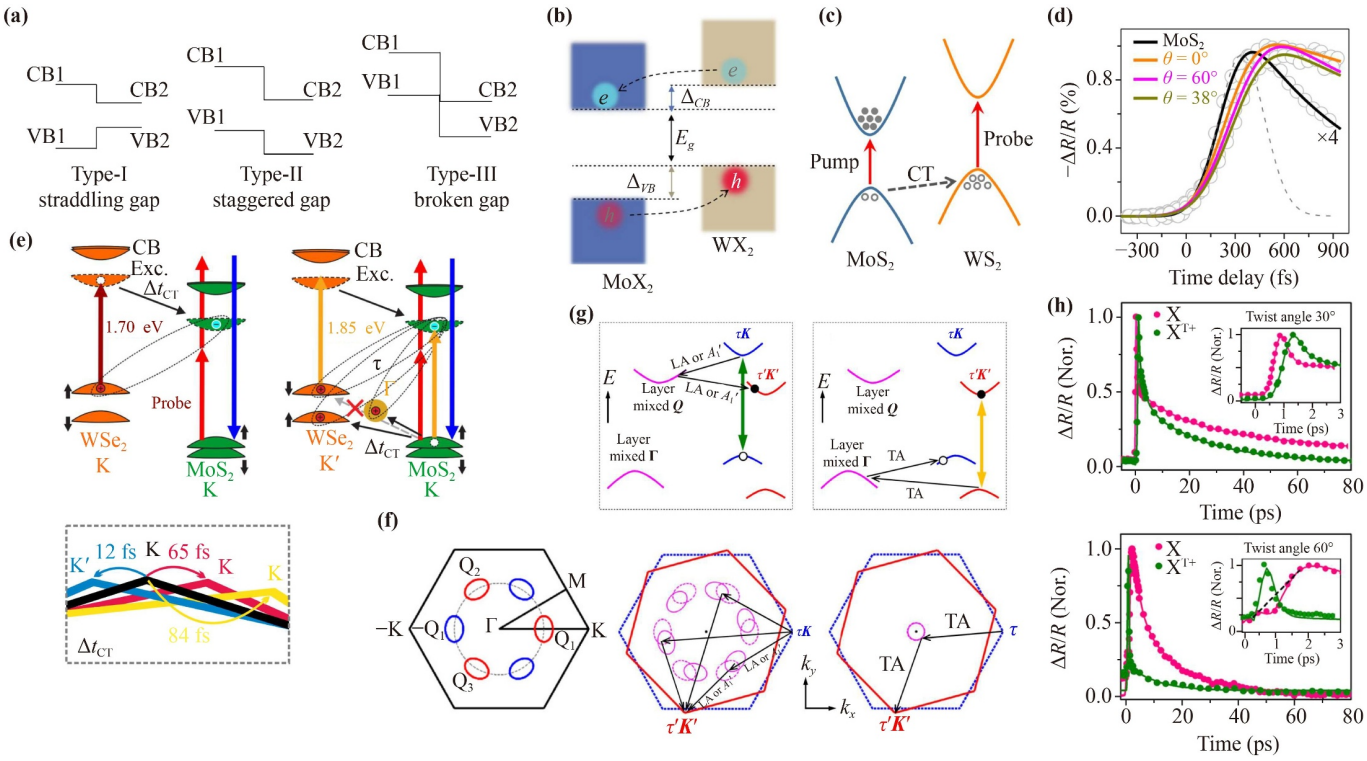

Fig. 5 Exciton dynamics modulated by twist angle. **(a)** Three types of band alignment in semiconductor heterostructures. The VB and CB represent valence band and conduction band positions, respectively. **(b)** Scheme of the charge transfer in type-II band alignment of TMD heterostructures. **(c)** Schematic illustration of interlayer hole transfer in of MoS_2/WS_2 heterostructures after optically pumping MoS_2 A-exciton, while the electron remains in the MoS_2 layer. **(d)** The transient absorption spectra obtained by selectively probing the WS_2 A-exciton resonance in MoS_2 monolayer or MoS_2/WS_2 heterostructures with varying twist angles. **(e)** Sketch of the band alignment and ultrafast charge transfer dynamics for twisted MoS_2/WSe_2 under 1.70 eV pump (left panel) and 1.85 eV pump (right panel). **(f)** The structure of the monolayer Brillouin zone, where the red and blue closed curves indicate the energy contours of Q_c valleys. The dashed circle denotes a ring region with strong interlayer coupling of the conduction band. **(g)** Schematic illustrations of interlayer charge transfer process mediated by strong layer mixed Γ and Q valleys in the energy (upper two panels) and momentum (lower two panels) spaces. The right two panels depict the electron transfer and those on the left correspond to the hole transfer. **(h)** Differential reflection signal of WS_2/WSe_2 heterostructures under 30° (upper panel) and 60° (lower panel) twist, respectively. (b) Reproduced with permission from Ref. [54]. (c, d) Reproduced with permission from Ref. [79]. (e) Reproduced with permission from Ref. [85]. (f, g) Reproduced with permission from Ref. [52]. (h) Reproduced with permission from Ref. [84].

perception that the interlayer charge transfer dynamics would sensitively depend on the relatively weak interlayer coupling affected by twist angle [54]. Moreover, the momentum mismatch between valleys from different constituent monolayers is expected to reduce the efficiency of interlayer charge transfer. Utilizing the STEM and time-dependent DFT simulations, the atomic-level local structural inhomogeneity caused by interlayer stretching and shifting is considered to be the origin of the observed robustness of ultrafast interlayer charge transfer. Such interlayer sliding provides extra parallel multi-channels for the efficient transfer process [79]. From the perspective of momentum mismatch in twisted heterostructures, phonon scattering coupled with interlayer hybridization mediates the twist-insensitive ultrafast interlayer charge transfer [52, 54]. Unlike the layer-localized $\pm\boldsymbol{K}$ valleys whose coupling strengths exhibit sensitive dependence on the interlayer twist and translations, the $\boldsymbol{\Gamma}_v$ ($\boldsymbol{\Gamma}$ point of valence band as the VBM) and $\boldsymbol{Q}_c$ (six CBMs near the middle of the $\boldsymbol{\Gamma}$–$\tau\boldsymbol{K}$ path) show strong interlayer coupling comparable to the corresponding band offsets in TMD heterostructures, as shown in Fig. 5(f). Such strong interlayer mixing is attributed to the nonignorable effects of p_z orbital of chalcogen atoms, as well as the relatively larger hopping integral with smaller momentums compared with those in $\pm\boldsymbol{K}$ valleys [52]. These highly layer-hybridized valleys allow the twist-independent ultrafast interlayer charge transfer of type-II TMD heterobilayers via a two-step mechanism involving the $\boldsymbol{\Gamma}_v$ and $\boldsymbol{Q}_c$ valleys as intermediary states. Specifically, the photoexcited electron with high energy in $\tau\boldsymbol{K}_c$ valley can be scattered to the $\boldsymbol{Q}_c$ valleys through coupling with phonons, defects, or other carriers, and subsequently relax to the $\tau'\boldsymbol{K}_c'$, as depicted in Fig. 5(g).

The high energy hole in $\tau'\boldsymbol{K}'_{\rm v}$ can similarly transfer to the $\tau\boldsymbol{K}_{\rm v}$ mediated by the strongly layer mixed $\boldsymbol{\Gamma}_{\rm v}$ valley. The efficient scatterings are supported by the strong couplings between carriers in $\pm\boldsymbol{K}$ valleys and the related phonons. Wang and co-workers [52] predicted this two-step interlayer electron (hole) transfer process assisted by phonons, and the calculated intervalley scattering rates accorded with experimental results. Twist in bilayers does not influence interlayer coupling and band offset of $\boldsymbol{\Gamma}_{\rm v}$ valley, while $\boldsymbol{Q}_{\rm c}$ valleys are always within the strongly interlayer hybridized ring region under arbitrary twist angle. Therefore, the ultrafast (< 50 fs) interlayer charge transfer in TMD heterostructures is unimpeded by interlayer rotational mismatch [52]. This two-step mechanism has been demonstrated by the observation of ultrafast electron intervalley scattering in MoS_2/WS_2 heterostructure with a small twist angle of 5° using the time- and angle-resolved photoemission spectroscopy (TR-ARPES), where electrons in $\boldsymbol{K}$ valleys are scattered to intermediary valleys (M, M/2 and Q) within 70 fs and relaxed to $\boldsymbol{K}'$ and $\boldsymbol{Q}'$ valleys on timescales of ~0.4 ps [114].

However, such robustness against interlayer twist in TMD heterostructures does not persist in all circumstances. Recent experimental researches on how the twist angle affects rapid charge transfer show diverse results. For a longer timescale of hundreds of femtoseconds in twisted WS_2/WSe_2 heterostructures, the interlayer tunneling rate decreases significantly as the rotational mismatch rises, affecting the formation and relaxation dynamics of interlayer excitons [115]. On the other hand, a more complicated stacking angle modulation mechanism of ultrafast dynamics has been revealed by more precise measurements (e.g., much higher time resolutions). Zimmermann *et al.* [85] investigated the ultrafast charge transfer dynamics affected dramatically by stacking angle in MoS_2/WSe_2 heterostructures at an ultrafast time resolution of about 6 fs. They conducted the measurement by the time- and polarization-resolved second-harmonic (SH) imaging microscopy, which could directly identify signals from different regions (two kinds of monolayers and their overlap) and control the SH intensity of different regions. For 1.70 eV pump which only resonantly excited the intralayer A-excitons of WSe_2, the extracted transfer time $\Delta t_{\rm CT}$ from WSe_2 to MoS_2 layer of probed electron sensitively depended on stacking angle: which are comparable in quasi-3R (θ = 9°, $\Delta t_{\rm CT}$ = 65 ± 10 fs) and misaligned (θ = 16°, $\Delta t_{\rm CT}$ = 84 ± 10 fs) cases, while become much faster in quasi-2H (θ = 52°, $\Delta t_{\rm CT}$ = 12 ± 6 fs) case [see Fig. 5(e)]. The twist-angle dependence was attributed to the different wave function overlap at $\boldsymbol{K}$ valleys between constituent layers at different stackings. Such distinct wave function overlap also influenced the recombination lifetimes, about hundreds of picoseconds, where stronger spatial coincidence was found in quasi-2H case [85]. When both materials were excited, the transient SH response of quasi-2H heterostructure presented a rapid recovery on femtosecond timescale slightly slower than those in the corresponding monolayer, which was not observed in the quasi-3R and misaligned samples. This discrepancy was explained by the competition between the coherent (intralayer) radiative recombination and additional relaxation tunnels, where holes from the MoS_2 layer could be scattered to the WSe_2 layer in $\boldsymbol{K}$ valleys or strongly hybridized states in $\boldsymbol{\Gamma}$ valley. As shown in Fig. 5(e), hole transfer from $\boldsymbol{K}'(\boldsymbol{K})$ in MoS_2 to $\boldsymbol{K}(\boldsymbol{K}')$ in WSe_2 was spin forbidden in the quasi-2H case, and the misaligned case had a larger momentum mismatch than that in quasi-3R stacking sample. Therefore, the efficiency of the hole transfer decreased from quasi-3R, misaligned to quasi-2H, which corresponded to the increasing coherent recombination [85]. This result indicates the possibility of modifying the layer mixed states through stacking configuration, thus affecting the exciton dynamics. Apart from the vdW heterostructures composed of the TMD family, the charge transfer and relaxation dynamics of TMD-Gr heterostructures are also strongly modulated through the twist-angle-tunable overlap between interlayer electronic states. Recently, Luo and co-workers [86] have realized the simultaneous visualization of charge transfer and electron–phonon coupling using the UED method and demonstrated the sensitive dependence of interlayer charge transfer on the twist angle [116].

In vdW heterostructures, intralayer and interlayer Coulomb interaction leads to the formation of diverse quasi-particle species such as intralayer excitons, interlayer excitons and trions. Twist angles in vdW heterostructures also influence the optical behaviors of these "many-body" species. Recently, Shi *et al.* [84] observed increased luminescence ratio of positive trions compared with excitons in steady-state PL spectra of WS_2/WSe_2 heterostructure under twist angle of 30° and 60° but not 0°. They used ultrafast transient absorption spectroscopy to reveal the faster formation time for trions than intralayer excitons at θ = 60°, and the higher formation probability of trions due to accumulation of residual free carriers at θ = 30°, as illustrated in Fig. 5(h).

There are several theoretical discussions on moiré physics and a considerable part of experimental observations of the moiré quasi-periodic structures using high-resolution methods such as annular dark-field scanning transmission electron microscopy (ADF-STEM) [56]. Nevertheless, comprehensive investigations focusing on moiré pattern remained scarce in early experimental researches. Since the moiré pattern is easily disordered in a heterostructure without hexagonal boron nitride encapsulation [93], limitations of the quality of the sample mainly account for this lack. Besides, the effects arising from moiré potential would be submerged at room temperature.

3 Moiré excitonic physics

Twistronics investigates the physics including electronic, optical and magnetic properties [117] of twisted 2D van der Waals heterostructures, and has promoted various studies as mentioned above. In the wake of experimental technology progress, an increasing number of researchers have set their sights on the moiré superlattices (MSL), which are formed by heterostructures stacked with a finite relative twist angle or lattice mismatch. MSL can trigger various exotic properties, such as flat bands [49, 50, 64, 118–120], excitons modulated by moiré periodic potential [57, 121] and many-body effects [122] in such artificial superlattice. The magic angles in twisted bilayer graphene generate fascinating properties including correlated insulator states and unconventional superconductivity originating from the flat bands [59–61, 123]. Since then correlated electronic physics has been investigated in various graphene-based structures such as ABC trilayer graphene/BN [61, 124–126] and twisted double bilayer graphene (TDBG) [127]. In the last few years, moiré effects and correlated phenomena have also been found in other 2D materials-based systems such as TMDs [128–131]. TMDs possess unique advantages compared with graphene due to their desirable properties, such as sizeable bandgap and large spin-orbit coupling. Therefore, MSL in TMDs would perform thermal stability and feasibility for topological band engineering and spatially alternating spin-valley configuration [93]. There are several theoretical predictions on the moiré modulated excitons and corresponding optical response of TMDs-based heterostructures, like localized excitons and nanodot quantum emission arrays [132]. In addition, TMD MSLs have flat bands that exist over a wide range of stacking angles instead of certain magic angles [133], making MSL easier to realize and providing an extra rotation degree of freedom for modulating the moiré effects.

When vertically stacked vdW layers present a complex periodic pattern consisting of varying interlayer atomic alignment, the in-plane moiré superlattice will take shape, as shown in Figs. 6(a) and (b). Moiré superlattice will be formed in two ways mainly determined by the magnitude of relative twist, including the rigid-lattice and atomic reconstruction [132]. The rigid-lattice moiré pattern would naturally occur under a relative rotation angle or lattice mismatch between constituent layers, and such misalignment serves as a crucial node for controlling the electronic structure and optical properties [134–137]. The periodic MSL can be represented by a moiré wavelength λ_m [138]:

$$\lambda_m = \frac{(1+\delta)\,a_0}{\sqrt{2\,(1+\delta)\,(1-\cos\theta)+\delta^2}}, \tag{3.1}$$

where lattice mismatch is presented as $\delta = \frac{|a_0{}' - a_0|}{a_0}$, and a_0, $a_0{}'$ denote the lattice constants of the two constituent layers, with θ as the relative twist angle. The corresponding moiré period (also known as moiré lattice constant) under small lattice constant mismatch δ can be approximately represented as $a_M \approx \frac{a_0}{\sqrt{\delta^2+\theta^2}}$ [65], with length scales from a few nanometers to tens of nanometers [54, 93]. As mentioned above, there are different types of commensurate stacking patterns, which can be subsumed under two categories: near-rhombohedral stacking (R-stacking) and near-hexagonal stacking (H-stacking). The high-symmetry local atomic registries existing in one moiré supercell preserve three-fold rotational symmetry $\hat{C}_3$ and generate charming properties such as spatially alternating optical selection rules [49]. As depicted in Figs. 6(a) and (b), these high symmetry points can be labeled by the notation $\mathrm{R}_\mathrm{h}^\mathrm{A}$ ($\mathrm{H}_\mathrm{h}^\mathrm{A}$) (A = h, X, M) for R-(H-)stacking, indicating the "A" in the electron layer aligned to the "h" in the hole layer. The superscript "A" here refers to the lattice center (h), chalcogen atom (X) or metal atom (M). Varying interlayer atomic registries in the moiré supercell result in the spatial modulation of interlayer distance, exciton potential energy and spin-valley characteristics [49, 93, 132]. For stacking order at near-commensurate twist angle ($\theta \approx 0°$ or 60°), atomic-level reconstruction would be induced through interlayer coupling and lattice relaxation. Instead of a smoothly varying rigid-lattice moiré pattern, discrete commensurate regions with narrow boundaries will be formed [139–142]. These discrete domains with constant conductivity could be observed using conductive atomic force microscopy (CAFM), as shown in Fig. 6(c). Furthermore, the existence of strain variation across the moiré supercell leads to substantial strain accumulations at region boundaries and domains with relatively unstable stacking orders, which introduces lattice deformation and extra modulation on band structures [143]. DFT calculated band structures revealed the spatial modulation of the relative electronic band edges induced by atomic reconstruction [140]. Consequently, such spatial distribution of considerable strain affects the formation of excitonic species and optical properties, which are also highly tunable by relative twist [92].

As the fabrication, detection and observation of moiré structures become increasingly achievable, multiple experimental studies on moiré excitons have been performed through electronic and optical measurements such as STEM [56], PL [63, 144, 145] and Reflectance spectroscopy [145, 146]. The mechanisms of how moiré structure modulates intralayer and interlayer excitons have attracted much attention but still lack a comprehensive explanation. For the moiré superlattice with a periodicity of about 10 nm in a twisted semiconducting vdW heterostructure, excitons have the Bohr radius between the moiré wavelength and the lattice constant of monolayer [132]. Therefore, exciton in superlattice can be regarded as a composite quasi-particle modulated by

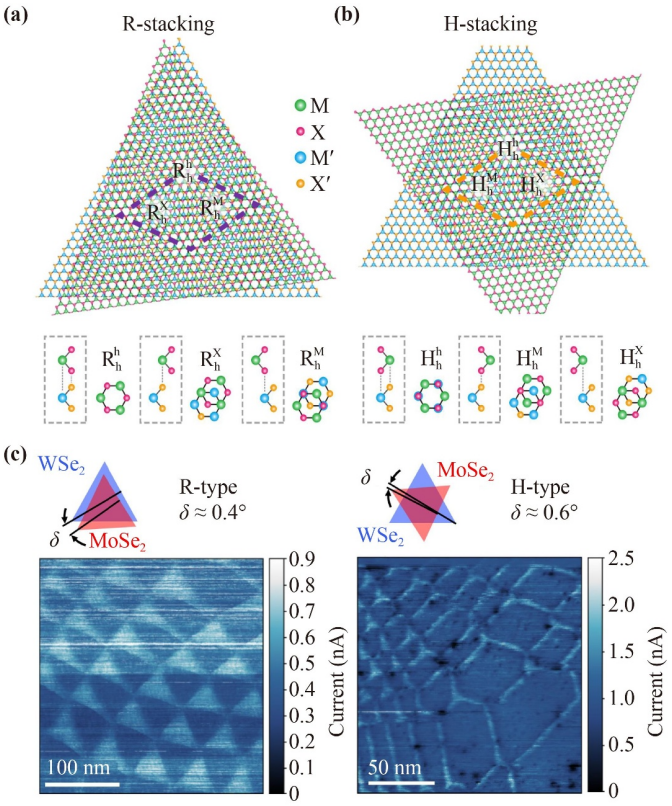

Fig. 6 MSLs in twisted TMD heterostructures. High symmetry points in a moiré supercell of near R-stacking **(a)** and near H-stacking **(b)** MSLs. **(c)** CAFM image of near-0° (left panel) and near-60° (right panel) heterostructures presenting alternating triangular and hexagonal domains with constant conductivity and narrow boundaries. (a, b) Reproduced with permission from Ref. [93]. (c) Reproduced with permission from Ref. [140].

exciton potential with spatially periodical variation, manifesting in the locally changing oscillator strength and optical transition dipole [49]. The center-of-mass motion could be described by [147]:

$$H = \hbar\Omega_0 + \frac{\hbar^2 \boldsymbol{k}^2}{2M} + \Delta(\boldsymbol{r}), \tag{3.2}$$

where $\hbar\Omega_0$ is a constant representing the energy of the lowest exciton state without moiré potential energy, $\frac{\hbar^2\boldsymbol{k}^2}{2M}$ is the center-of-mass kinetic energy, and $\Delta(\boldsymbol{r})$ denotes the exciton moiré potential energy with M as the exciton effective mass. $\Delta(\boldsymbol{r})$ varies smoothly and can be approximated by the lowest-order harmonic expansion [64, 65]:

$$\Delta(\boldsymbol{r}) \approx \sum_{j=1}^{6} V_j \exp(i\boldsymbol{b}_j \cdot \boldsymbol{r}), \tag{3.3}$$

where $\boldsymbol{b}_j = \theta \boldsymbol{G}_j \times \hat{z}$ defines the reciprocal lattice vectors of the moiré superlattice under a finite θ [65]. Near $\mathrm{R}_\mathrm{h}^\mathrm{h}$ points, $\Delta(\boldsymbol{r})$ has the form of a harmonic oscillator with quantized energy levels modulated by twist angle through changing moiré period [147]. This harmonic-potential model is widely accepted in most TMD heterostructures but cannot dominate all systems [132]. In the case of band alignment under small band-edge offset, the near-resonant hybridization between interlayer and intralayer excitons would occur through interlayer tunneling in moiré minibands, which generates hybridized excitons with intriguing features [146, 148–150].

3.1 Theoretical predictions and experimental observations of new excitons in moiré structure

As mentioned in the previous section, early experimental methods and sample quality cannot provide sufficient conditions for the observation and further investigation of moiré modulated exciton properties. Whereas, several theoretical prediction works [49, 52, 64–66, 118] on the new physics of excitons in moiré superlattice have been reported. In the superlattice with a large-scale moiré period, a mini Brillouin zone (BZ) would be formed, whose corners are located at $\tau\boldsymbol{K}$–$\tau'\boldsymbol{K}'$ and its $\pi/3$ rotations [52], as depicted in Fig. 7(a). The original monolayer bands are folded into a series of closely spaced mini bands inside the mini BZ, where interlayer hopping can happen between states with the same wave vector $\boldsymbol{k}$ from different layers [Fig. 7(b)]. The local atomic registry is spatially varying in a moiré supercell much larger than the monolayer unit cell, resulting in a periodic modulation of the local band structure [52]. Yu *et al.* [49] described the moiré modulated exciton as an exciton wave packet moving adiabatically in the periodic potential, which was constructed by the basis of kinematic momentum eigenstates under misaligned heterobilayer. In the near R-type stacking case, exciton wave packets at the three high symmetry points [A–$\mathrm{R}_\mathrm{h}^\mathrm{h}$, B–$\mathrm{R}_\mathrm{h}^\mathrm{X}$ and C–$\mathrm{R}_\mathrm{h}^\mathrm{M}$ in Fig. 7(c)] have distinct $\hat{C}_3$ transformations due to the different $\hat{C}_3$ eigenvalues of the electron Bloch function:

$$\hat{C}_3\chi_{A,s} = \mathrm{e}^{-\mathrm{i}\frac{2\pi}{3}s}\chi_{A,s},\ \hat{C}_3\chi_{B,s} = \mathrm{e}^{\mathrm{i}\frac{2\pi}{3}s}\chi_{B,s},\ \hat{C}_3\chi_{C,s} = \chi_{C,s}. \tag{3.4}$$

Here, χ is the exciton wave packets and $\mathrm{s} = +(-)$ denotes the spin-valley index for exciton at $\boldsymbol{K}$ ($-\boldsymbol{K}$) valley with up (down) spin. As shown in Figs. 7(d) and (e), the convertible photons must possess the same rotational symmetry, which leads to the spatially alternating optical selection rules. The interlayer exciton emissions are circularly polarized at A and B points with opposite helicity and forbidden at C, while the emissions are elliptically polarized at other locals in the moiré supercell. The distinct rotational symmetries in the three points also make them the extrema of exciton potential [Fig. 7(e)]. The strong deep traps of exciton potential (~100 meV) around the global minima at A points can

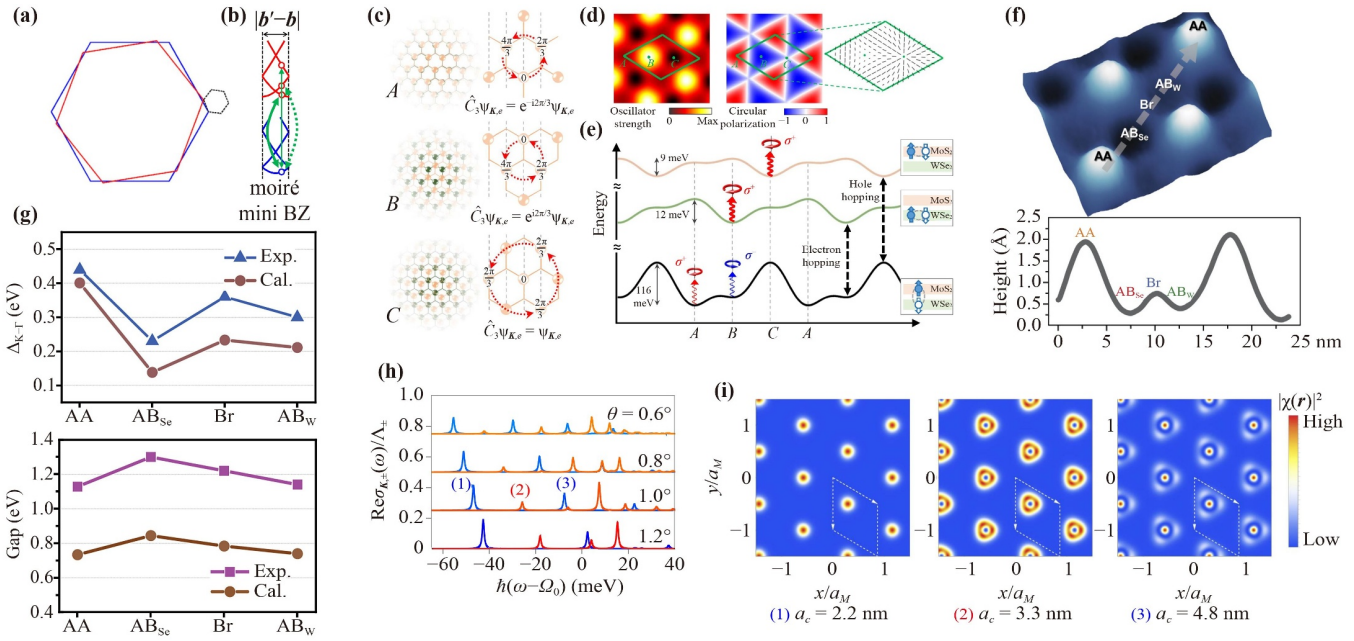

Fig. 7 Theoretical predictions of excitons in moiré superlattices. **(a)** The monolayer Brillouin zones (solid blue and red hexagons) and the mini Brillouin zone of moiré superlattice (dash black hexagon). **(b)** The corresponding interlayer hopping terms (green double arrows) between different mini bands near the band edges of the 1D moiré mini BZ. **(c)** Exciton wave packets at the three high symmetry locals (left column) and the corresponding transformations of electron Bloch wave function with hexagon center of the hole layer as a rotation center. **(d)** Oscillator strength of the interlayer exciton (left panel) and optical selection rule (right panel) for the spin-up interlayer exciton at the K valley. The insert denotes the major axis of polarization with the length proportional to ellipticity. **(e)** Contrasted potential landscapes for the intralayer and interlayer excitons, with the optical selection rules for the spin-up species at the energy minima. **(f)** Upper panel: A perspective view of an STM image zoomed in on one moiré supercell. Lower panel: A height profile under varying stacking order along the diagonal line. **(g)** The site-dependent electronic structures in MoS_2/WSe_2 heterobilayers. Upper panel: The experimental values and calculated DFT results of energy differences between K_W and Γ_W of valence band at four different local atomic registries. Lower panel: The experimental and calculated DFT results of local bandgap formed between the CBM of MoS_2 and the VBM of WSe_2. **(h)** Optical spectrum of K-valley interlayer excitons under different twist angles of WS_2/MoS_2 heterobilayer with AA stacking. The red and blue curves show the optical absorption in response to σ_+- and σ_--polarized light at frequency ω, respectively. **(i)** The real-space probability function of the interlayer excitons responsible for the first three absorption peaks at $\theta = 1°$. (a, b) Reproduced with permission from Ref. [52]. (c–e) Reproduced with permission from Ref. [49]. (f, g) Reproduced with permission from Ref. [56]. (h, i) Reproduced with permission from Ref. [56].

realize perfect arrays of nanodot confinement, which can act as uniform quantum emitters tunable by perpendicular electric field and strain [49]. The moiré pattern with periodic varying interlayer separation was observed experimentally by scanning tunneling microscope (STM) measurement in MoS_2/WSe_2 heterobilayer, as shown in Fig. 7(f) [56]. The STM and scanning tunneling spectra (STS) also revealed the formation of an electronic superlattice and detailed information on the local electronic structures affected by interlayer coupling. The experimentally observed and DFT-calculated site-dependent electronic structures showed consistent trends as illustrated in Fig. 7(g). Wu and co-workers [65] adopted the theory of moiré potential modulated interlayer exciton and predicted that moiré potential affected interlayer excitons in two aspects: First, the periodic potential mixed and split the three independent exciton COM eigenstates that were otherwise degenerate at the moiré Brillouin zone (MBZ) corners, resulting in new exciton eigenstates with rotational symmetries of the moiré pattern. Thus, the circular optical selection rule remained, which was sensitive to the spatially varying potential energy and local optical absorption strength, but not locked to the valley. The moiré potential energy mixed COM eigenstates, and consequently split the spectral weight associated with interlayer excitons across a variety of different states. Such energy splitting can be tuned by twist angles through changing moiré periodicity and the MBZ [Fig. 7(h)]. Second, the exciton states could be confined in potential minima [Fig. 7(i)], allowing the realization of nanoscale 2D arrays of identical quantum dots. The calculated exciton band structure in the moiré Brillouin zone had flat-band features for the first few exciton bands, showing the mixing of excitons with different momenta and strong confinement for these Wannier excitons states. The exciton moiré band structure

would exhibit Dirac dispersion within the light cone when the moiré potential was tuned to have an additional two-fold rotational symmetry besides the $\hat{C}_3$ symmetry [65]. Wu and co-workers also focused on the intralayer excitons under periodic moiré potentials and found that moiré superlattice in the TMD bilayer generated the twist-angle-dependent satellite excitonic peaks in the optical absorption spectrum [64]. These theoretical works also point out the topological features of the moiré exciton bands that would further relate to the unique Hubbard models with twist-angle-dependent hopping and interaction strength [118]. Twisted bilayers with moiré structure provide an accessible platform to simulate the Hubbard models for exploring many-body phenomena such as spin-liquid states and quantum anomalous Hall insulators [49, 64].

With the development of experimental methods, multiple observations of moiré effects in vdW heterostructures have been reported and showed diverse characteristics and fascinating physics. In most cases, the periodic moiré potential was regarded to play a crucial role in the emergence and modulation of excitons in a twisted heterostructure, supporting the harmonic-potential model based on perturbation theory. Pan *et al.* [57] observed the moiré pattern in MoS_2/WSe_2 on epitaxial graphene using STM and STS at temperatures of 5 and 80 K. STS showed significant energy shifts of about 0.2 eV between the maxima and minima of the moiré corrugation [Fig. 8(a)]. Sharp peaks (linewidth <10 meV) occurred near band-edge energies of the spectra for both the valence band (VB) and the conduction band (CB) at 5 K, which were attributed to the quantum-confined states associated with the Γ_W–VB and K_{Mo}–CB under moiré potential. These confined states showed obvious temperature dependence and the corresponding narrow peaks vanished at 80 K. The spatially periodic in-plane potential leads to splittings of both intralayer exciton and trion energies, which was observed in the emission and absorption spectra of $MoSe_2/MoS_2$ heterostructure encapsulated in hBN at 5 K, as shown in Figs. 8(b)–(d) [121]. The energy differences between the split peaks were consistent with the theoretical predictions mentioned above. The intensities of the split peaks of excitons and trions also exhibited temperature dependence, suggesting that excitons can be detrapped from moiré potential minima through thermally activated phonon scattering. Moiré exciton states were also observed from the multiple emergent peaks around the original WSe_2 A exciton resonance in the absorption spectra of closely aligned WSe_2/WS_2 heterostructures at 10 K [151]. These peaks were considered to arise from the strongly coupled heterobilayer rather than from several separated domains, since the photoluminescence excitation (PLE) spectrum showed the strong enhancement of the interlayer exciton emission under excitation at the energies of each of the three emergent peaks (labeled as resonances I, II and III), as shown in Fig. 8(e). Different moiré exciton peaks in WSe_2 exhibited distinct dependences on electron doping in WS_2 [Fig. 8(g)]. The discrepancy indicates that peaks I, II and III arose from exciton states with different real-space distributions in the moiré superlattice. These phenomena were well explained by the theoretical model in which the periodic moiré potential was much stronger than the exciton kinetic energy and generated multiple flat exciton minibands [151]. Besides, excitons modulated by moiré potential have also been observed in TMD vdW homostructures [63, 141, 145, 152]. Wu *et al.* [63] observed moiré intralayer excitons in WSe_2/WSe_2 bilayers with small twist angles in the PL spectrum at 8 K. The extracted moiré potential depth (inversely proportional to the moiré superlattice period) increased with the twist angle, manifesting as more splitting and broader energy peaks [Fig. 8(h)]. As the excitation power increased, moiré excitons turned into a main peak dominated by intralayer excitons with a larger peak width in the PL spectrum. The power dependence of moiré exciton peaks was attributed to the saturation of flat minibands filled by trapped excitons [63]. Moiré excitons were also identified in the twisted WS_2/WS_2 homostructure with a twist angle of $1.46° \pm 0.07°$ determined by SHG [145]. The multiple emergent peaks in the PL spectrum at 8 K exhibited a nearly constant peak spacing of 19 ± 3 meV and showed similar pump power dependence, which also resulted from the flat electronic minibands generated by the reconstructed moiré potential.

Although the effective harmonic-potential model has been utilized to describe moiré effects successfully in TMD heterostructures with considerable interlayer band edges offsets like WS_2/WSe_2 and $MoSe_2/MoS_2$, this theoretical model cannot explain moiré excitonic behaviors in all systems. In the case of TMD heterostructures with a slight band-edges offset featuring nearly degenerate carrier bands, such as $MoSe_2/WS_2$ and some twisted homobilayers, resonant interlayer hybridization must be explicitly considered. The interlayer hybridization would enhance the moiré superlattice effects on the electronic structures and lead to the formation of hybridized excitons (hXs) through interlayer carrier tunneling [146, 150]. The hybridized excitons arise out of the band hybridization effects [Fig. 8(j)], consisting of strongly mixed electron or hole states involved in the formation of intralayer excitons (Xs) and interlayer excitons (IXs). The hXs inherit the brightness of intralayer excitons and the polarity of interlayer excitons, leading to their identical optical selection rules to those of intralayer excitons in constituent monolayer and sensitivity to vertical electrical bias, respectively [132, 150]. The theoretical absorption spectra of resonant heterobilayers $MoSe_2/WS_2$ varied sharply with twist angle, as shown in Fig. 8(l), in which a bright line at higher energies appeared when closely aligned due to moiré umklapp electron-photon interac-

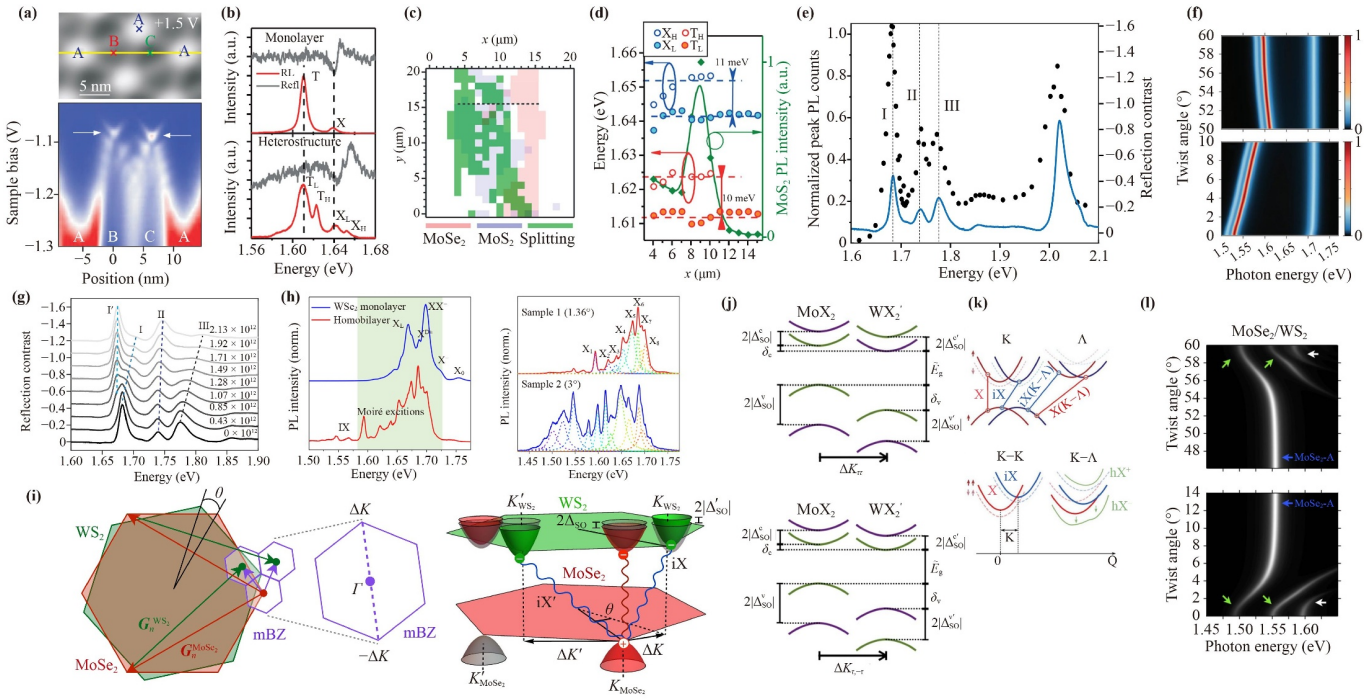

Fig. 8 Experimental observations of moiré excitons. **(a)** STM image with different moiré locations of MoS_2/WSe_2 heterostructure (upper panel) and constant-height conductance map for voltage in the valence band-edge region (lower panel), where confined states occurred at B and C. **(b)** PL and reflectivity spectra of $MoSe_2$ measured in monolayer and $MoSe_2/MoS_2$ heterostructure. **(c)** Spatial map showing the presence of $MoSe_2$ transition splitting overlaid with the areas of most intense PL of MoS_2 and $MoSe_2$. **(d)** The energy of the observed $MoSe_2$ transitions (blue and red dots) extracted along the horizontal dashed line of (c). Green diamonds denote the MoS_2 PL intensity. **(e)** Comparison between the interlayer exciton PLE spectrum (black dots) and the reflection spectrum (blue curve) of WSe_2/WS_2 moiré superlattice. **(f)** Twist-angle dependent PL calculated for i) anti-parallel and ii) parallel stacking twisted WSe_2 on SiO_2 at 4 K. **(g)** Reflection contrast spectra in the range of the WSe_2 A exciton on the electron-doping side. **(h)** Optical characteristics of moiré intralayer excitons in WSe_2/WSe_2 twisted homobilayer. Left panel: Comparing the PL spectra of WSe_2 monolayer and homobilayer at 8 K. Right panel: PL spectra of homobilayers with twist angles of 1.36° and 3°. **(i)** Left panel: Moiré mini Brillouin zone (purple) defined by the moiré Bragg vectors (purple arrows). Right panel: Electronic band structures and Brillouin zone alignment for twisted $MoSe_2/WS_2$ heterobilayers. Spin-down (spin-up) bands are colored red or green (grey). **(j)** Band alignments with almost resonant conduction band states of the twisted bilayer of TMD MoX_2 and WX'_2 (X, X′ = S, Se, Te) for near parallel ($\theta \approx 0°$, left panel) and near antiparallel ($\theta \approx 60°$, right panel) cases. **(k)** Exciton hybridization in twisted bilayers TMDs. Upper panel: Schematic electronic band structure at the K and Λ valley of the two twisted layers (red and blue, respectively) as well as possible intra- (X) and interlayer excitons (IX). Lower panel: Schematic exciton center-of-mass dispersion without hybridization as well as hybridized K–Λ state hX (green). **(l)** Twist-angle dependent low-energy absorption spectra near the energy of A exciton in $MoSe_2/WS_2$ with resonant conduction band edges. The hXs form at closely alignment cases, leading to the avoided crossings marked by green arrows. The white arrows denote the absorption lines enabled by moiré Umklapp processes. (a) Reproduced with permission from Ref. [57]. (b–d) Reproduced with permission from Ref. [121]. (e, g) Reproduced with permission from Ref. [151]. (f, k) Reproduced with permission from Ref. [149]. (h) Reproduced with permission from Ref. [63]. (i) Reproduced with permission from Ref. [146]. (j, l) Reproduced with permission from Ref. [150].

tions. The umklapp processes fold exciton states with finite-momentum onto zero-momentum, regarded as the evidence for moiré superlattice minibands for the excitons. Such features were absent in non-resonant cases due to the weak mixing between IXs and X [150]. Alexeev *et al.* [146] investigated the interplay between moiré superlattice effects and twist-angle dependent hybridization of X and IX in $MoSe_2/WS_2$ heterostructures with near-degenerate conduction band edges. The exciton energy and linewidth in PL spectra change periodically with the interlayer twist angle at a period of $\theta \approx 60°$, suggesting a connection to the valley rotational mismatch between the Brillouin zones of two constituent monolayers $\Delta \boldsymbol{K} = \boldsymbol{K}_{WS_2} - \boldsymbol{K}_{MoSe_2}$ $(\Delta \boldsymbol{K'} = \boldsymbol{K'}_{WS_2} - \boldsymbol{K}_{MoSe_2})$. The conduction-band states had plane-wave projections onto all Bragg vectors of their corresponding reciprocal lattices $\boldsymbol{G}_n^{MoSe_2}$ and $\boldsymbol{G}_n^{WS_2}$. As a result, the interlayer tunneling between states satisfied momentum conservation $\boldsymbol{k}_{WS_2} - \boldsymbol{k}_{MoSe_2} = \Delta \boldsymbol{K} + \boldsymbol{b}_n$. Here, $\boldsymbol{k}_{WS_2}$ and $\boldsymbol{k}_{MoSe_2}$ were the corresponding first-Brillouin-zone wave vectors from the K valley. The $\boldsymbol{b}_n = \boldsymbol{G}_n^{WS_2} - \boldsymbol{G}_n^{MoSe_2}$ denoted the first Bragg vectors of moiré superlattice, which defined the twist-

angle-dependent mini BZ, as depicted in Fig. 8(i). In closely aligned (or anti-aligned) $MoSe_2/WS_2$ heterobilayers, the minimized momentum mismatch for interlayer conduction-band tunneling enabled hybridization between the interlayer excitons and the $MoSe_2$ intralayer excitons (both A and B excitons), leading to shared hole band of the hybridized excitons (hXs) [Fig. 8(i)] [146]. The resulting hXs (labeled as hX_1) and higher-energy peaks arising from the moiré mini-band states of hX (labeled as hX_2 and hX_3) appeared at closely aligned case in reflectance contrast spectra at low temperatures (T = 10 – 105 K). Apart from the bright excitons, momentum-dark excitons in moiré superlattice have also been reported to be affected by interlayer hybridization. Berm *et al.* [149] investigated the twisted WSe_2 bilayers and showed the twist-angle-dependent electron hybridization at the Λ point of momentum-indirect K–Λ exciton in phonon-assisted PL (T = 4 K). The K–Λ excitons exhibited a prominent hybridization effect due to their strong delocalization over both layers, in contrast to the K-K excitons, as shown in Figs. 8(f) and (k).

Recently, several experimental methods apart from optical measurements for observation of moiré superlattice and moiré exciton have been reported. Andersen and coworkers [141] realized the direct stacking domains imaging in vdW heterostructure devices. They developed a secondary electron microscope (SEM) technique to investigate reconstructed moiré patterns in twisted WSe_2/WSe_2 bilayers. They directly demonstrated the considerable variation of local moiré periodicity in a small twist angle bilayer and correlated the local structure with distinct optical properties. Karni *et al.* [153] utilized the time-resolved and angle-resolved photoemission spectroscopy (TR-μ-ARPES) to capture images of the electron and hole distributions of interlayer exciton in WSe_2/MoS_2 heterostructure. The interlayer exciton was found to have a diameter comparable with the moiré period, whereas its center of mass was highly confined in a region much smaller than the size of the exciton itself.

3.2 Localization and modulation of excitons by moiré superlattice

Excitons in TMD moiré superlattices under the spatially varying potentials show in-plane localization [153] and possess the flat-band feature. The flat bands are related to the in-plane localization due to the vanishing of group velocity [154]. The moiré potential traps are analogous to the localized defect levels in semiconductors, where the moiré periodicity corresponds to the defect–defect distance. The "defect" bands would become less dispersive as the periodicity increased and their interactions reduced [50]. Since the amplitude and period of moiré potential are sensitive to the interlayer stacking and twisting in vdW heterostructures, the spatial distributions, resonant energies and oscillation strengths of moiré excitons can also be continuously tunned by twist angle. Guo *et al.* [50] theoretically predicted the distributions of moiré excitons in twisted MoS_2/WSe_2 heterostructures under different angles. Based on time-dependent density functional theory (TDDFT), they predicted that exciton with lower energy could be more localized and would experience deeper moiré potential under a small twist angle relative to $\theta = 0°$ or 60°, as shown in Fig. 9(a). The holes showed stronger in-plane localization than electrons, consistent with the narrower bandwidth of VBM than that of CBM [50]. The calculated charge density showed that the hole with stronger in-plane localization extended to both layers (modulated by interlayer moiré potential), while the delocalized electron is confined at the $MoSe_2$ layer (modulated by intralayer moiré potential). This result suggested a more localized interlayer exciton than intralayer exciton because the bandgap modulation of interlayer exciton was larger than that of the intralayer exciton [50]. Numbers of studies have observed the intralayer excitons in moiré superlattices. Under moiré potential with a relatively large period, the moiré intralayer excitons and trions in $MoS_2/MoSe_2$ heterostructure exhibited unchanged decay times compared with those in monolayer at 5 K due to the relatively weak localization effect [121]. In the reconstructed moiré patterns of WSe_2/WSe_2 homobilayer with spatially alternating AB- and BA-stacked domains, a higher-energy intralayer exciton peak emerged in the p-doped regime of PL spectra (T = 4 K) at regions with larger λ_m, in contrast to those with $\lambda_m < 10$ nm. As shown in Fig. 9(b), the two peaks showed different doping dependence and distinct valley coherence represented by the degree of linear polarization (DOLP) [141]. These results could be explained by the formation of two exciton species (type I and II excitons). The two intralayer exciton species were distributed in different intralayer locations with different bandgaps in the reconstructed superlattice, as depicted in Fig. 9(c). Type II excitons could only be observed in perfectly reconstructed moiré patterns with aligned domains size larger than the exciton diffusion length (estimated to be 10–100 nm), because the interlayer tunneling at the K point was symmetry forbidden in AB/BA-stacked domains, which would prevent the excitons from relaxing to the lower-energy state (type I) before recombining. Type I excitons could bind strongly to extra holes under p-doped to form charged excitons due to the higher VBM of exciton I than that of type II excitons. Whereas, the less-layer-localized electrons were expected to interact with both exciton species under n-doping, since the global CBM was located at the Q point [Figs. 9(c) and (d)] [141]. The doped hole in type I location and exciton I could form an entangled state $|\mathrm{K}\rangle_{\mathrm{X}}|\mathrm{K}'\rangle_{\mathrm{h}} \pm |\mathrm{K}'\rangle_{\mathrm{X}}|\mathrm{K}\rangle_{\mathrm{h}}$ under the Pauli exclusion principle.

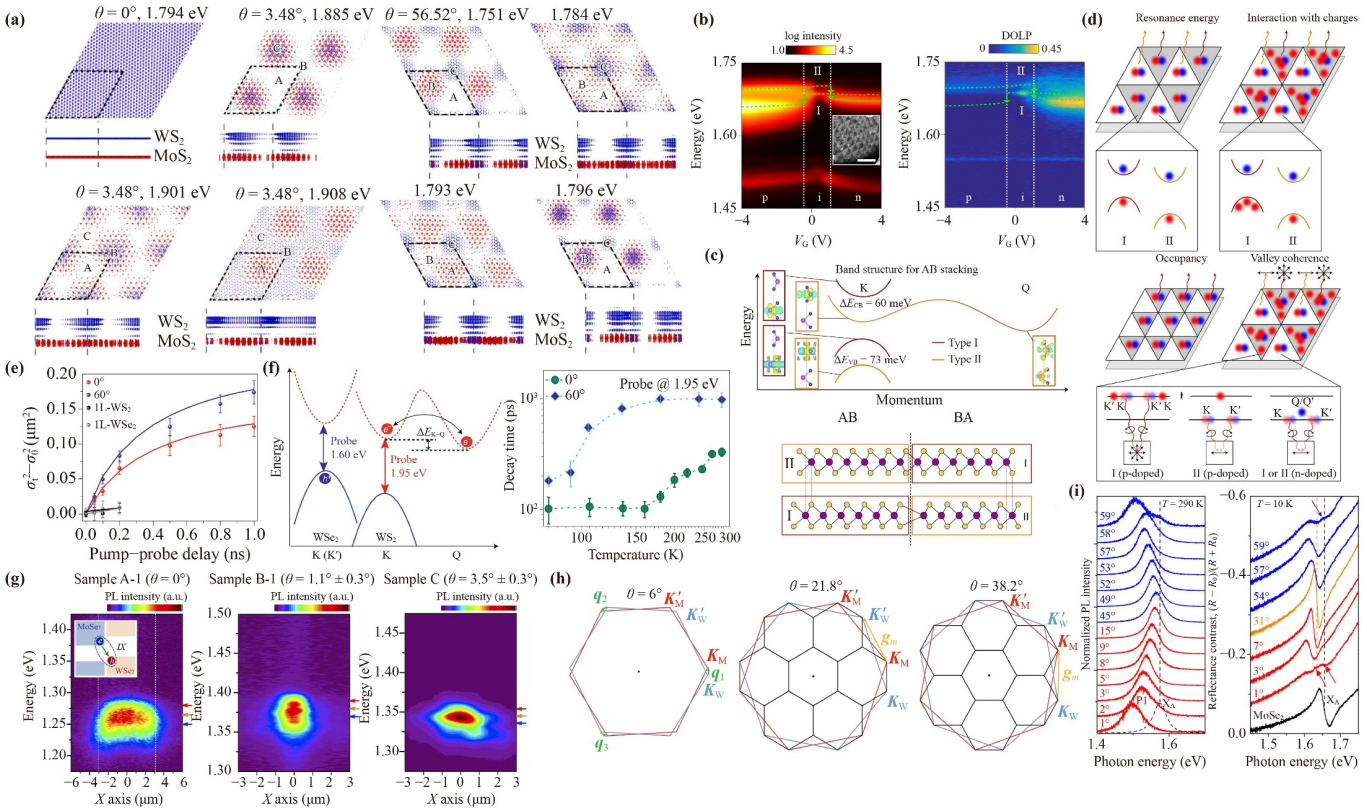

Fig. 9 Exciton properties and dynamics modulated by moiré superlattice. **(a)** Localized moiré excitons with different twist angles and energies in the MoS_2/WS_2 heterostructure. The charge densities of the electron and the hole are colored in red and blue, respectively. **(b)** Gate-dependent PL spectra (left panel) and DOLP (right panel) of the two exciton species in WSe_2 bilayers with reconstructed moiré superlattice. Inset in the left panel: SEM image of the measured spot. **(c)** Upper panel: Band structure schematic and wavefunction distribution at important points in k-space. Lower panel: Side views of AB and BA domains, where type I and II locations are denoted by maroon and orange boxes, respectively. **(d)** Schematic of alternating properties in the 2D triangular exciton array, showing only excitons in the top layer for brevity. **(e)** Anomalous diffusion of interlayer excitons in WS_2/WSe_2 heterobilayers with exciton density at time zero $N_0 = 6.0 \times 10^{12}$ cm^{-2} at 295 K, compared with the normal exciton diffusion in 1L-WSe_2 and 1L-WS_2 with linear temporal dependence. **(f)** Twist-angle- and temperature-dependent K–K and K–Q interlayer exciton dynamics. Left panel: Schematic of the probing electron (reflecting K–K interlayer exciton population) and hole (reflecting the sum of the K–K and K–Q exciton populations) dynamics. Right panel: The fitted decay time of the K–K exciton as a function of temperature under exciton density at 4.1×10^{12} cm^{-2}. **(g)** Spatially resolved PL images of the interlayer excitons for CVD-grown sample A-1, mechanical exfoliation and transfer (MET) sample B-1, and MET sample C with different twist angles θ, respectively. **(h)** Schematics of the Brillouin zone of twisted bilayers. The red (blue) hexagons denote the Brillouin zone of $MoSe_2$ (WS_2) monolayers. In the left panel with $\theta = 6°$, the green arrows indicate vectors of momentum shift between the Brillouin zone corners of the two monolayers. In the middle (right) panel, a commensurate moiré reciprocal lattice is formed with the corresponding moiré Brillouin zone denoted by the black hexagons. The yellow arrow represents the moiré reciprocal lattice base vector that connects K_M and K'_W (K_W). **(i)** Twist-angle dependence of normalized PL spectra at 290 K (left panel) and reflectance contrast spectra at 10 K (right panel) of $MoSe_2/WS_2$ heterobilayers near the A-exciton energy in an isolated $MoSe_2$ monolayer (black). (a) Reproduced with permission from Ref. [50]. (b–d) Reproduced with permission from Ref. [141]. (e, f) Reproduced with permission from Ref. [134]. (g) Reproduced with permission from Ref. [158]. (h) Reproduced with permission from Ref. [135]. (i) Reproduced with permission from Ref. [146].

The orthogonal $|K'\rangle_h$ and $|K\rangle_h$ made linearly polarized emission impossible because of the broken symmetry caused by correlated resident holes. On the contrary, the resident hole of type II excitons was in the other layer and carried no information about the exciton valley, allowing a non-zero DOLP. DOLP was non-zero for both exciton species in the n-doped regime, because the electron would be located in a valley (Q/Q′) different from that of the exciton (K/K′) [141]. The results indicate the possibility of realizing exciton arrays with tunable quantum coherence properties based on reconstructed moiré superlattices.

Compared with intralayer excitons, interlayer excitons with spatial separation and permanent dipole are

expected to be more deeply affected by moiré potential, which could serve as interacting bosonic lattices suitable for experimental realization of Bose–Hubbard model and study on bosonic supersolid and superfluid states [155–157]. Given the relatively long lifetime and diffusion length of interlayer excitons, modulation of the interlayer excitons diffusion dynamics by moiré superlattice is of great interest [50, 54]. The exciton diffusion in the moiré system can be described as a range of incoherent hops between sites with local minimum of moiré potential. The confined moiré excitons are expected to have shorter diffusion lengths compared with the delocalized excitons. The observed diffusion length of the moiré exciton was one order of magnitude smaller than that in the untwisted $WSe_2/MoSe_2$ heterostructure [26, 50]. Using transient absorption (TA) microscopy, Yuan *et al.* [134] investigated interlayer exciton dynamics and transport in WS_2/WSe_2 heterobilayers under twist angles of 0° and 60° with a 4% lattice mismatch, which had a moiré period of about 7.6 nm. The diffusions of interlayer excitons with non-linear temporal dependence of mean square distance $\sigma_t^2 - \sigma_0^2$ deviated from the normal diffusions of intralayer excitons in the constituent monolayers [Fig. 9(e)]. The deviations suggested the interplay between moiré potentials and strong repulsive exciton–exciton interactions of interlayer excitons. Diffusions of interlayer exciton exhibited twist-angle dependence, corroborating the twist-angle tunable moiré potentials. Specifically, the DFT calculation indicated deeper potential and stronger localization for interlayer excitons at $\theta \approx 0°$ than those at $\theta \approx 60°$. A larger energy difference between the K and Q valleys of the conduction band ΔE_{K-Q} in the 0°-twisted bilayer suppressed the efficient electron scattering from Q to K, compared with the 60° twisted case. Consequently, WS_2/WSe_2 heterobilayers presented a shorter K–K exciton decay time and higher temperature for thermally excited phonons to assist the Q–K scattering at near-0° than at near-60°, as shown in Fig. 9(f) [134]. Choi and co-workers [158] also reported that interlayer exciton diffusion in $WSe_2/MoSe_2$ heterobilayers could be highly controlled by twist angle, using spatially and time-resolved PL measurements at $T = 4$ K, as shown in Fig. 9(g). The presence of moiré superlattice with a large supercell and deep potential at small twisting could completely localize interlayer exciton and lead to a reduced lifetime and velocity. Consequently, the diffusion length was decreased in comparison with that in commensurate heterostructure. At a larger twist angle leading to a reduced moiré period, excitons may tunnel between supercells and have a longer interlayer exciton lifetime [46, 158]. Apart from the low-temperature case, the temperature-activated diffusivity is also dependent on the twist angle due to the deep moiré potentials [136]. Moiré potential effects can be effectively screened at a sufficiently high exciton density or temperature [134]. The moiré interlayer excitons of $MoSe_2/WSe_2$ heterobilayers showed a transition temperature, above which the confined IXs turned to be delocalized, manifesting as significantly decreased PL intensity. The temperature dependence of IXs was considered to result from IX–IX exchange interactions exceeding the moiré potential traps at a sufficiently high temperature [159]. Brem and Malic [155] have newly reported the theoretical prediction that the strong delocalization of moiré-confined interlayer excitons would occur at intermediate densities (10^{11}–10^{12} cm^{-2}) due to the combination of strong repulsive IX–IX interactions and their bosonic nature. The delocalization causes a blueshift and the collapse of the split series of optical moiré resonances, which would merge into a single free exciton peak. The interlayer exciton lifetime has also been demonstrated to be influenced by moiré potential [160]. Based on a low-energy continuum mode, the twist-angle-dependent IX lifetimes in twisted TMD bilayers should consider two main mechanisms: One is the shift to indirect transitions due to the rotation momentum mismatch under an increasing twist angle. The other mechanism is that the presence of moiré potential introduces an interaction among the IXs with different COM momenta and opens additional radiative recombination channels, resulting in the relaxed momentum conservation and consequently a softened twist angle dependence [160].

In addition to interlayer twist and temperature, various factors in twisted vdW heterostructures have shown the ability to modulate the localization of moiré excitons in recent researches. Cai and co-workers [161] focused on the formation mechanism of numerous PL peaks from localized interlayer excitons in moiré superlattices. They constructed an interlayer donor-acceptor pair exciton (DAP IX) dynamic model to explain the origins of these narrow excitonic peaks, where the localized DAP exciton has an electron trapped in the donor site and a hole trapped in the acceptor site. They also fabricated an hBN-encapsulated $MoSe_2/WSe_2$ bilayer ($\theta \approx 60° \pm 1°$) on a nanopillar array, and experimentally confirmed the DAP IX model through observations of the emission energy-lifetime correlation and unique nonmonotonic power dependence of the energy-resolved lifetime. The nanopillars here produced strain to provide PL emission enhancement through strain gradient-induced funnelling as well as the increased coupling between the band-edge and DAP IX, indicating the modulation of moiré excitons from out-of-plain strain. Coincidentally, Lin *et al.* [143] have demonstrated the influence of atomic-level in-plane strain on moiré potential. They measured the moiré potential for excitons in a large amount of $MoSe_2/MoS_2$ heterobilayers with various twist angles. Surprisingly, the moiré potential depth for intralayer excitons was found to be up to ~130 meV, which was larger than the predicted value of most DFT calculations and comparable to the potential depth for interlayer excitons. The deepened moiré potential depth for intralayer excitons was

attributed to the remarkable in-plane strain distribution caused by atomic reconstruction, which would induce band gap variation up to ~100 meV in $MoSe_2$. Besides vdW heterobilayers, multilayer-based systems can provide new degree of freedom for moiré superlattice regulations. Zheng and collaborators reported that interlayer excitons in both twisted $WSe_2/WSe_2/WSe_2$ and $WSe_2/WS_2/WSe_2$ trilayers were confined by deeper moiré potentials compared with bilayer systems, manifesting as multiple dense and sharp emission peaks in PL spectra [162, 163].

For the circumstance suitable for the resonant hybridization model, twist angle modulate the properties and dynamics of interlayer and intralayer hybrid excitons (hXs) by changing moiré reciprocal lattices [135]. The properties of the hXs such as oscillator strengths, resonance energies, and mixing of intralayer and interlayer components, are sensitively dependent on the moiré period (twist angle) [135, 146], as shown in Fig. 9(i). It is notable that though large detuning between interlayer and intralayer states would suppress hybridization over a range of angles deviating from aligned or anti-aligned cases, pronounced hybridized moiré excitons with strong interlayer tunneling occur under twist angles near 21.8° and 38.2°, These high-angle moiré excitons were observed in $WS_2/MoSe_2$ bilayers by reflectance contrast spectra at 4 K. The features and valley configurations of moiré hXs at $\theta = 21.8°$ and $\theta = 38.2°$ resembled those at $\theta = 0°$ and 60°, respectively [135]. Moiré reciprocal lattice at these angles are commensurate with the monolayer lattices in Brillouin zones and therefore the angularly mismatched valleys of constituent monolayers are connected by primitive moiré reciprocal lattices vectors. The commensurate moiré lattices allow nearly resonant tunneling between the intra- and interlayer states, which contributes to the observable hX features, as depicted in Fig. 9(h) [135]. Furthermore, the moiré reciprocal lattices at $\theta = 21.8°$ and 38.2° have the largest reciprocal lattice constant equivalent to $1/\sqrt{7}$ of the monolayer reciprocal lattice constant, corresponding to the smallest moiré lattice with $\Sigma = 7$. Σ is the coincidence site lattice (CSL), defined as the smallest unit cell volume shared by the commensurately twisted bilayers. The unit cell maintains the in-plane rotational and translational gliding symmetry [137]. Zhao and co-workers [137] systematically investigated the optical properties of TMD homobilayers with various twist angles. For the MoS_2 homobilayers with $\Sigma = 7$ ($\theta = 21.8°$), an intense peak of indirect moiré excitons (1.6 eV) appeared in the PL spectra at 10 K. The indirect moiré excitons showed PL intensity stronger than that of direct intravalley excitons (1.9 eV), which was attributed to a smaller effective mass at the multiple valley points in the conduction bands. Similar commensurate structures at $\Sigma = 13$ ($\theta = 27.8°$) also showed a remarkable moiré exciton peak, but its relative intensity with respect to the intravalley exciton decreased due to a flattened conduction valley. These high-angle commensurate twisted bilayers exhibit optoelectronic properties different from those in the small twist angle cases and are commonly found in as-prepared samples without deliberate alignment, which would motivate further studies into dynamics and valley properties of these high-angle moiré excitons [137].

Moiré system based on twisted TMD heterostructures can form large-scale superlattice with spatially modulated bandgap confining excitons in localized orbitals [52], providing a strongly interacting regime [122]. The moiré superlattice offers a compelling platform for exotic many-body interactions phenomena, such as exciton BEC, especially for the indirect interlayer excitons with interlayer electric dipole and relatively longer lifetimes [122]. Recently, Remez *et al.* [122] have shown that the strong interactions in twisted TMD bilayers can drive "leaky emission" originate from "dark condensate" where momentum-indirect excitons form a Bose–Einstein condensate. These "leaky emissions" originate from strong interactions and dominate the photoluminescence of TMD moiré excitons at low temperatures with distinctive features.

3.3 Spin-valley configuration of moiré excitons

Excitons in moiré superlattice experience spatially varying periodic potential due to the local bandgaps, determined by the atomic registry. As shown in Fig. 7(c) and (e), intralayer excitons and interlayer excitons confined in the local energy minima have different landscapes, accompanied with distinct spin-valley optical selection rules [49]. In near-0° twisted heterostructures and homostructures, valley optical selection rules for moiré intralayer excitons were maintained, presenting a degree of circular polarization (DOP) very similar to that in the monolayer [Fig. 10(a)]. In conclusion, the moiré pattern has no influence on the intralayer optical transitions due to the unchanged rotational symmetry in the plane of the monolayer [63, 121, 145].

On the contrary, optical selection rules for interlayer excitons exhibit extra complexity. The intralayer excitons excited by circularly polarized light will then relax through the interlayer transfer process to form interlayer excitons. The spin and valley indices of carriers would be conserved in this process [65]. Unlike intralayer excitons, interlayer excitons with certain spin-valley configurations may generate emissions with circular polarizations opposite to those of the excitation light. Take R-type stacking MoX_2/WX_2 heterobilayer (X denotes chalcogen) as an example. As mentioned in Section 3.1, moiré interlayer exciton wave packets at the high-symmetry locals have distinct $\hat{C}_3$ transformations described by Eq. (3.4). Hence the corresponding convertible photons must have the same rotational symmetry [65]. Therefore, the calculated optical selection rules would vary spatially, as depicted in Fig. 7(e): The spin-up exciton wave packet

at local A (B) only couples to light with $\sigma^+(\sigma^-)$ circular polarization, while light coupling at C is forbidden. At other locals without $\hat{C}_3$ symmetry, optical selection rules manifest as elliptical polarization [49]. Wu *et al.* [63] investigated the valley polarization of interlayer excitons in WSe_2/WSe_2 twisted homobilayer by measuring the polarized-resolved PL spectra at 8 K. Here, interlayer excitons showed two emission peaks with opposite polarizations, as shown in Figs. 10(b) and (c). The distinct behaviours of the two IX peaks were attributed to the spin–orbit coupling effect. The conduction band split into spin-up and spin-down energy levels, where the two kinds of interlayer excitons with different transition energies exhibit distinct spin configurations, depicted in Fig. 10(c) [63]. In contrast to the monolayer TMD where the spin-triplet excitons are considered dark, the optical transition dipole of the spin-triplet interlayer exciton is expected to be comparable to that of the spin-singlet exciton in TMD heterobilayer due to the breaking of the out-of-plane symmetry [66]. Yu *et al.* [66] reported that as the local interlayer atomic registry changes, the optical transition dipole of interlayer exciton wave packet varies between two in-plane transition dipoles of opposite circular polarizations and the out-of-plane one, which enables the spatial modulation of IX light-coupling including the strength of optical transition dipole and the optical selection rule in a large scale moiré pattern. Additionally, the spin-triplet and spin-singlet excitons have distinct valley polarization selection rules at a certain atomic registry, as shown in Fig. 10(f). As a result, the selective optical addressing of both the valley and spin configurations of IXs would be achievable. Zhang and collaborators [164] identified the spin-singlet and spin-triplet exciton states with very high valley polarizations (over 80%) and opposite helicities in high-quality hBN encapsulated $WSe_2/MoSe_2$ heterobilayers with near 60° (58.7° ± 0.7°) twist angle at 4 K [Fig. 10(g)]. The two exciton states with high valley polarization and short lifetimes originated from direct band-gap transition, which were regarded to be localized at the H_h^h atomic registry (local point A as the potential minimum). In addition, the long interlayer exciton valley depolarization time suggested strongly suppressed intervalley exchange interactions, on account of both spatial separation of interlayer exciton as well as the discretized spin singlet and triplet states [164]. Jin *et al.* [67] also observed that the coexisting multiple interlayer exciton states localized at different sites in moiré supercell and exhibited opposite optical selection rules in a near-0° twisted WSe_2/WS_2 heterostructure at 10 K. In this work, PLE and resonant pump-probe spectroscopy were utilized to detect the relative oscillator strengths and spin-valley configurations of the moiré interlayer excitons. The conception of exciton quasi-angular momentum (QAM) was adopted here, which describes the phase change of the exciton wave function after the $\hat{C}_3$ transformation [Eq. (3.4)]. The total QAM of an interlayer exciton state directly determines its optical selection rule, which is related to the spin, valley, and moiré pattern. The spatially varying moiré QAM associated with different interlayer lattice registrations explained the opposite selection rules of multiple interlayer excitons in the WSe_2/WS_2 heterostructure [67].

The presence of moiré confinement for interlayer excitons can realize perfect arrays of quantum emitters, which are highly tunable by several external methods [49]. Seyler *et al.* [62] studied the valley-polarized nature of the trapped interlayer excitons of $MoSe_2/WSe_2$ heterobilayers at $T = 1.6$ K. The moiré trapped IXs exhibited strong valley polarizations with selection rules depending on the twist angle, as shown in Fig. 10(d), corroborating the retention of three-fold rotational symmetry under a sufficient smooth moiré potential. They performed magneto-photoluminescence spectroscopy to determine the Landé g-factor of the trapped interlayer excitons through the valley Zeeman effect [Fig. 10(e)]. The extracted g-factors were homogeneous across the same sample and took two values, –15.89 ± 0.03 and 6.72 ± 0.02 for near 60° (57°) and 0° (2°), respectively. The g-factor of an interlayer exciton represents its valley configuration and valley magnetic moment. Thus the two different values indicated the distinct valley-pairing configurations at the two twist angles. At $\theta \approx 60°$, the spin-flip optical transitions would lead to emissions with much larger Zeeman shifts, whereas the spin-singlet excitonic Zeeman splitting at $\theta \approx 0°$ was similar to that of the monolayer. In particular, the trapped interlayer excitons at $\theta = 20°$ (near the commensurate stacking angle 21.8° providing the shortest superlattice periodicity $\Sigma = 7$) had a g-factor close to that at $\theta = 57°$ because of the same valley configurations, while the emission intensities at $\theta = 20°$ were reduced by two orders of magnitude compared with those at $\theta = 57°$ due to the weak optical dipole of the umklapp recombination [62].

Beyond the moiré system based on heterobilayer, introducing the layer degree of freedom would open up more possibility of tuning the spin-valley configuration through spin-layer locking. Brotons-Gisbert and co-workers [165] fabricated a trilayer (TL) heterostructure consisting of a monolayer (ML) WSe_2 and bilayer (BL) 2H-$MoSe_2$ (anti-aligned) and observed the spin-layer locking of moiré-trapped excitons at cryogenic temperature. Two types of interlayer excitons IX^H and IX^R were identified, with electrons localized in the lower and upper $MoSe_2$ layer, respectively [Fig. 10(j)]. In magneto-optical spectroscopy measurements, the two IX species exhibited distinct spin-valley-locked magnetic moments and exhibited different optical selection rules determined by the local atomic registry of the moiré trapping sites, as shown in Figs. 10(h) and (i). Such spin-layer locking induces the layer index as a potential knob to engineer few-level quantum systems in vdW heterostructures, providing new opportunities for quantum information applications [165].

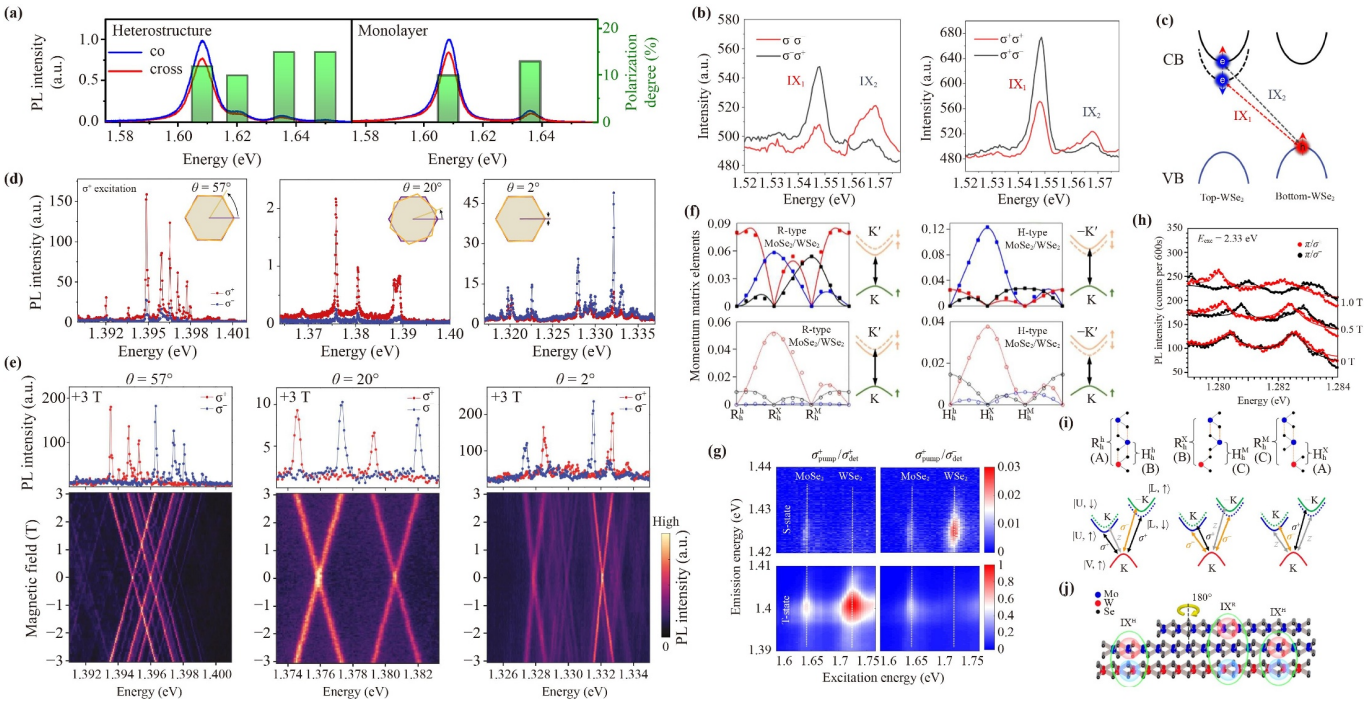

Fig. 10 Spin-valley configurations of moiré excitons. **(a)** Circular-polarization-resolved PL spectrum of $MoSe_2$ measured in (left panel) and out of (right panel) the $MoSe_2/MoS_2$ heterostructure region at $T = 5$ K. The green bars represent the DOP of the peaks. **(b)** Interlayer excitons valley polarization in WSe_2/WSe_2 twisted homobilayer at $T = 8$ K. **(c)** The illustration of the interlayer excitons transitions for IX_1 and IX_2 showing opposite circular polarizations. **(d)** Valley polarization of trapped interlayer excitons of $MoSe_2/WSe_2$ heterobilayers with twist angles of 57° (co-circularly polarized), 20° (cross-circularly polarized) and 2° (co-circularly polarized) excited by σ^+-polarized light at $T = 1.6$ K. The σ^+ and σ^- components of the photoluminescence are shown in red and blue, respectively. **(e)** Dependence of Zeeman splitting of trapped interlayer excitons on the twist angle in $MoSe_2/WSe_2$ heterobilayer. Top: Helicity-resolved PL spectra at 3 T under linearly polarized excitation. Bottom: Plot of total PL intensity as a function of magnetic field. **(f)** The spin-conserved and spin-flip momentum matrix elements for R-type and H-type $MoSe_2/WSe_2$ heterobilayers. The red, blue and black colors correspond to the σ^+, σ^- and out-of-plane (z) polarized components, respectively. **(g)** Valley-polarized singlet and triplet interlayer exciton emissions for hBN encapsulated $WSe_2/MoSe_2$ twisted bilayer. **(h)** Circular-polarization-resolved PL spectra of representative IX^R excitons of TL heterostructures (ML-WSe_2 and BL 2H-$MoSe_2$) trapped in the site R_h^h under linearly polarized excitation at 2.33 eV and different applied magnetic fields. **(i)** Schematics of the selection rules for optical transitions involving the K-point valence band for both spin-singlet and spin-triplet IXs trapped in moiré potential sites with different atomic registries. **(j)** Sketch of the TL heterostructures consisting of a 2H BL-$MoSe_2$ crystal with ML- and BL-thick terraces stacked on top of an ML-WSe_2. Electrons (red shadows) at the ±K valleys localized either in the bottom or top layer $MoSe_2$, are strongly bound to holes (blue shadows) in the WSe_2, creating two species of IX (green circles): IX^H and IX^R, respectively. (a) Reproduced with permission from Ref. [121]. (b, c) Reproduced with permission from Ref. [63]. (d, e) Reproduced with permission from Ref. [62]. (f) Reproduced with permission from Ref. [66]. (g) Reproduced with permission from Ref. [164]. (h) (i, j) Reproduced with permission from Ref. [165].

3.4 Moiré system under external tunning

As the novel electronic and optical physics of moiré superlattice based on van der Waals heterostructures has been widely investigated theoretically and experimentally, several researches on control of moiré systems by external tunning methods have been reported in recent years, such as electric fields [148], carriers doping [154, 166], magnetic field [62, 165], temperature [136, 159], strain [144, 167, 168] and so on. Thanks to the remarkable sensitivity to external factors, modulations on moiré systems based on 2D vdW heterostructures have shown desirable performance and novel physics.

An applied external electric field can effectively tune the properties of interlayer excitons due to their static electric dipole perpendicular to the plane ($\boldsymbol{p} = e\boldsymbol{h}$, where e is the charge quantity and $\boldsymbol{h}$ is the vector denoting charge separation from negative charge to positive charge) [50, 54]. The coupling between the perpendicular electric field and the electric dipole would shift energy levels due to the Stark effect, which can realize modulations of the resonant energy and polarity of interlayer exciton. Consequently, the in-plane distributions of moiré interlayer excitons are controllable by external electric fields. Guo *et al.* [50] used first-principle calculations to predict the charge density distributions tuned by the electric field in

the twisted MoS_2/WS_2 heterostructure, as shown in Fig. 11(a). Furthermore, the shifts of CBM and VBM from different constituent monolayers would control the interlayer resonant tunneling of the electron or hole and therefore the formation of hybridized excitons. In addition, an electric field can change both the electric dipole orientations and dipole moments of hXs [50]. Tang *et al.* [148] employed a dual-gate device [Fig. 11(b)] to independently apply a vertical electric field and doping to the WSe_2/WS_2 (type II band alignment) and $MoSe_2/WS_2$ (type I band alignment) heterobilayers at 5 K. They identified layer-hybridized moiré excitons through an emergent feature iX in the doping-dependent reflectance contrast spectrum, which was only observed in anti-aligned ($\theta = 60°$) WSe_2/WS_2 heterostructures. The configuration of anti-aligned WSe_2/WS_2 bilayers [Fig. 11(b)] enabled extra Bragg reflection from the moiré potential to help conserve quasi-momentum and promote strong coupling. Therefore, the resonant interlayer tunneling was regarded as spin-conserving. Under an out-of-plane electric field, strong exciton coupling was observed in WSe_2/WS_2 heterobilayers with coupling constants comparable to the intralayer moiré potential (~25 meV), manifesting as energy-level anticrossing and electric-field-dependent oscillator redistribution between the interlayer and intralayer resonances, as shown in Fig. 11(c). The IX peak exhibited linear electric-field response and weak oscillator strength when it was decoupled from other excitons under a sufficiently large positive perpendicular electric field, indicating the interlayer exciton nature of IX. The angle-aligned $MoSe_2/WS_2$ heterobilayers had much weaker coupling with the extracted coupling constants smaller than the exciton linewidths (about 5–10 meV), but still showed discernible multiple layer-hybridized moiré excitons with two distinct electric-field dispersions. In addition to layer hybridization, electric fields are also expected to control moiré exciton transport. Based on the Förster theory, the relative orientation of the dipole moments plays an important role in the modulation of moiré exciton diffusion [50]. Lately, several works have reported the electric-field-tunable spatial distribution and transport of excitonic species in 2D vdW heterostructures. Tagerlli *et al.* [170] have achieved electrostatic control over layer-hybridized exciton states represented by effective out-of-plane dipole lengths and revealed the dipole-dependent micrometre-scale transport of hybrid exciton. They modulated the layer hybridization and many-body interactions of excitonic species in 2H-stacked WSe_2 homobilayers by applying a vertical electric field at 4 K. The moiré-less 2H-WSe_2 structures eliminated the potential traps and type-II band alignment, which allowed tunable exciton–exciton interactions and long-range propagating. In the presence of moiré superlattice, the electric-field-dependent hybridization would allow continuous tuning of interlayer exciton hopping between different moiré sites, and generate a mixture of these interlayer excitons as a superposition moiré states, which has been demonstrated in a trilayer WSe_2/monolayer WS_2 heterostructure reported by Lian and co-workers [171]. Besides, in the R-stacked TMD vdW heterostructures accompanied with breaking out-of-plane mirror symmetry, the electric field can act as a switch to flip the out-of-plane polarization through in-plane sliding motion, which would bring about interfacial ferroelectricity [81, 172, 173]. Utilizing piezoelectric force microscopy (PFM), Wang *et al.* [81] have achieved the visualization of moiré ferroelectric domains and observed the electric-field-induced domain wall motion in several nearly parallel-stacked R-type bilayers.

Doping introduces charged moiré excitons that obey fermionic statistics and exhibit distinct properties such as the long-range Coulomb interaction in contrast to bosonic neutral excitons, providing an accessible platform to study fermionic many-body effects [166]. Recently, Dandu *et al.* [154] have realized the control of carrier concentration by gate-induced doping in H-type stacked twisted MoS_2 bilayer, and investigated the coexisting localized and delocalized intralayer moiré excitonic species at 4.5 K. As $|V_g|$ increased, the energies of intralayer exciton peaks stayed relatively unchanged, whereas their intensities (except the localized exciton X_I) quenched rapidly accompanied with emergent peaks with lower energy, as shown in Fig. 11(d). The results suggested the unchanged spatial modulation of intralayer moiré potential and the formation of trions from the delocalized higher energy excitons. Through a combination of gating (modulation of carrier density and potential depth) and varying excitation power (exciton density), multiple intralayer moiré trion species would be formed with tunable localization phases, depicted in Fig. 11(e). They also demonstrated the gate tunable valley coherence and exciton–phonon coupling strength for the moiré excitons. The charging effects would influence the spin-valley physics of interlayer moiré exciton as well. Wang and collaborators [166] observed moiré trions as the moiré traps were filled with either electrons or holes in H-stacked $WSe_2/MoSe_2$ heterobilayer at 1.6 K, manifesting as new sets of narrow peaks in PL spectra, as shown in Fig. 11(f). These emergent peaks were about 7 meV below the energies of the neutral interlayer moiré excitons. The similar g-factors of these excitons and trions (about –16) implied their same spin-triplet configuration and the smooth moiré potential traps. When positively charged, the valley polarization of moiré trion was inverted to cross-circular polarization under the σ^+ excitation at WSe_2 monolayer exciton resonance, in contrast to the co-circularly PL in the neutral and negative cases. Such inversion was explained by the competition between spin-flip valley-conserved and spin-conserved valley-flip relaxation channels of electrons during the formation of interlayer trions. In both negative and

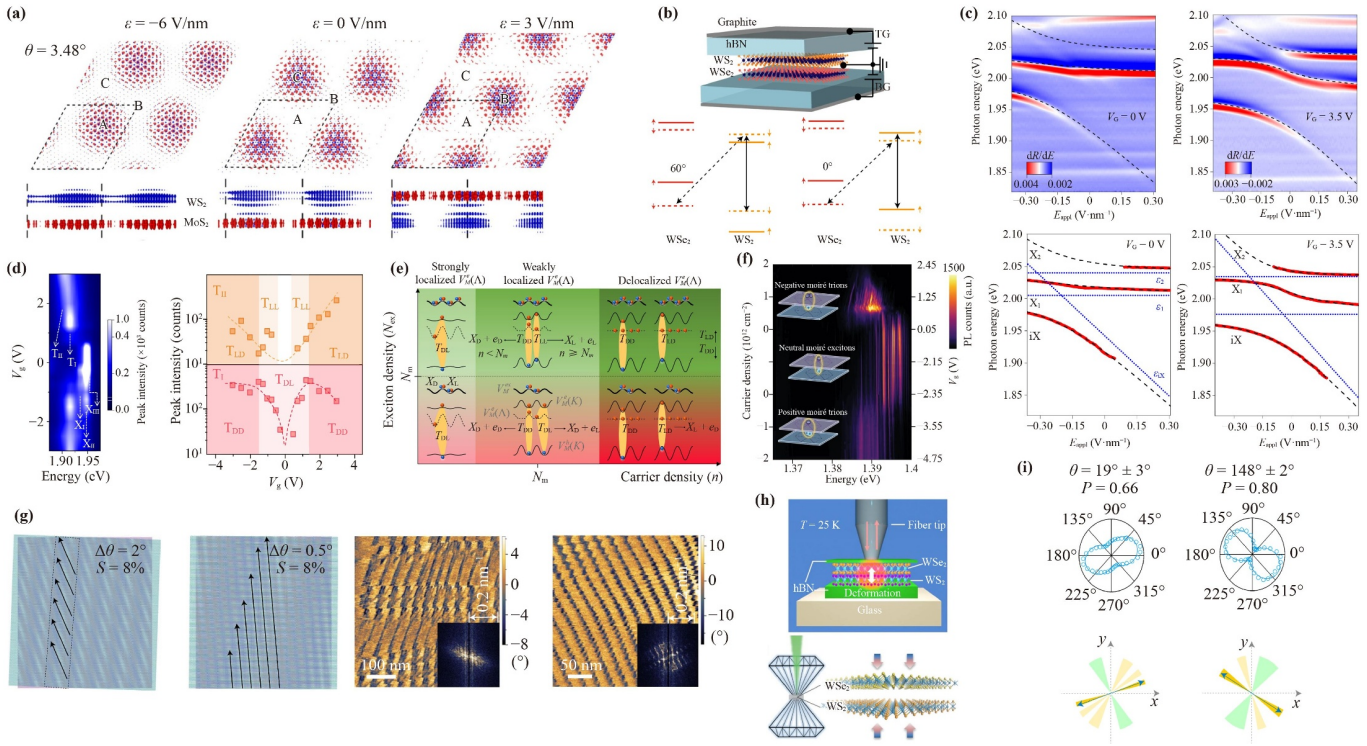

Fig. 11 Moiré system tunning by external methods. **(a)** The charge density distribution for the lowest-energy moiré exciton in the twisted MoS_2/WS_2 heterostructure under different electric fields. Red and blue colors represent the charge density of the electron and the hole, respectively. **(b)** Upper panel: Schematic of the dual-gate device structure for WSe_2/WS_2 bilayer. Lower panel: Type II band alignment for 60°-aligned and 0°-aligned samples. Intralayer (interlayer) dipole-allowed optical transitions are represented by solid (dashed) double-headed arrows. **(c)** Electric-field dependence of layer-hybridized excitons in 60°-aligned WSe_2/WS_2 moiré superlattice at fixed doping densities. Top row: Energy derivative of the reflectance contrast spectrum. Bottom row: The extracted exciton resonance energies, where solid red lines and dashed black lines represent experimental data and the best fit three-level model, respectively. The blue dotted lines show the dispersion of uncoupled exciton states. **(d)** Moiré trions in a twisted bilayer MoS_2. The left panel is the color plot of PL spectra under varying gate voltage. Right panel: Peak intensities of the two trion peaks as a function of gate voltage. **(e)** Phase diagram of moiré trion formation as a function of exciton density and electron density under positive gating, where N_m denotes moiré trap density. T_{AB} represent different types of trions, where the subscripts A and B denote the phase of the exciton and the electron involved in the trion formation, respectively. **(f)** PL spectra as a function of doping. Insets depict the charge configuration of both neutral and charged excitons. **(g)** Left two panels: Schematic of quasi-1D moiré superlattices formed with a uniaxial strain S of 8% under different twist angle $\Delta\theta$, where the arrows highlight the primary 1D moiré structures and the dashed rectangles of the secondary ones. Right two panels: PFM images at different locations of the twisted hBN/WSe_2/$MoSe_2$. Insets: FFTs of the PFM images. **(h)** Schematic of dynamic tunning of moiré excitons in WSe_2/WS_2 heterostructure by optical fiber tip (upper panel) and DAC (lower panel). **(i)** Direct correlation between 1D moiré patterns and linearly polarized PL emissions for $WSe_2/MoSe_2$ heterobilayers under different twist angles. Top row: Angular dependence of the PL emission. Bottom row: Corresponding angular distribution in the 2D FFTs of the PFM images. The light-golden sectors represent the angular distributions of the primary oval structures in the strained moiré landscapes, while the green sectors denote the angular distributions of the secondary pseudo-1D stripes formed by the primary structures. The blue double arrows represent the corresponding PL polarization directions. (a) Reproduced with permission from Ref. [50]. (b, c) Reproduced with permission from Ref. [148]. (d, e) Reproduced with permission from Ref. [154]. (f) Reproduced with permission from Ref. [166]. (g, i) Reproduced with permission from Ref. [167]. (h) Reproduced with permissions from Refs. [144, 168].

neutrally charged cases (M_T^- and M_X^0) where the optical selection rules were determined by the spin-valley index of the photo-excited hole, the excited K-valley-polarized hole could form a spin-triplet recombining pair with –K′ valley electron. The resulting high co-circular PL polarization suggested that the valley polarization of the excited hole was well-protected by spin-valley locking and that these multiple election–hole pairs were all trapped at H_h^h locals. Under hole-doping (M_T^+), the emission polarization was determined by the electron valley configuration since the doped holes would distribute at both opposite valleys. The relaxation channels of photo-excited electrons involved either a spin flip or a valley flip, where the latter was found to dominate the process, resulting in the smaller cross-circular polarization of M_T^+ [166]. Moreover, the properties of layer-hybridized excitons

including energies, coupling constants and effective dipole moment can also be significantly modulated by doping through electron-exciton interactions under considerable localization of moiré potential [148]. The rich and complex phenomena of moiré excitonic species under electrical modulation indicate the promising potential of engineering both bosonic and fermionic many-body physics. Furthermore, their dynamic adjustable features suggest the possibilities of photonic and valleytronic devices based on moiré systems.

The excellent inherent mechanical flexibility and remarkable strength of two-dimensional materials make strain engineering an ideal tuning method for manipulating their electronic and optical properties. For example, Both graphene and TMD possess maximum elastic strains larger than 10% [29]. Strain can realize continuous band structure modulation [30, 32, 174, 175], and inhomogeneous strain can creat local variation of bandgap [31, 176–178]. The stacking structures of twisted 2D vdW heterostructures enable sensitive and dynamic strain engineering of moiré potential landscape [167] and topological properties [33]. Moreover, the moiré system only requires small strains to achieve considerable modulation. By applying proper differential (inequivalent strains on the two constituent layers in the order of the lattice mismatch) and uniaxial tensile strain to twisted $WSe_2/MoSe_2$ heterobilayers, Bai *et al.* [167] transformed the zero-dimensional (0D) moiré pattern into a one-dimensional (1D) structure with parallel stripes and presented real-space imaging of these two patterns using PFM, as shown in Fig. 11(g). In the 1D moiré pattern, the photoluminescence emission at 4 K from interlayer exciton showed a single broad peak and significantly higher intensity in contrast to the 0D case. The enhanced broad peak in PL spectra was attributed to the higher density of states with densely spaced excitonic levels and radiative recombination from multiple levels. The emissions of 1D structures were linear polarized and their directions were aligned with the direction of one of the primary structures obtained from 2D-FFT (Fast Fourier Transforms) image analysis [Fig. 11(i)]. The linear polarization here was qualitatively attributed to the hybridization of the two valley configurations through electron-hole exchange interaction, because the electron-hole wave functions were highly anisotropic in the 1D moiré potential from the breaking $\hat{C}_3$ rotational symmetry. The strain-field-induced 1D moiré potential, analogous to the quantum wires, is attractive for studying strongly correlated and anisotropic charge transport [167]. Apart from the differential strain, in-situ deformation is another approach to realize dynamic control of the moiré potential and correlated states by directly altering the interlayer separation of the vdW heterostructures, which can help gain a clear understanding of the exciton physical behaviour in moiré system [144, 168]. Li and coworkers [144] have performed the *in-situ* dynamic modulation of moiré potential for twisted WS_2/WSe_2 heterostructures by employing diamond anvil cell (DAC) hydrostatic pressure engineering at room temperature [Fig. 11(h)]. When the pressure was lower than 1.1 GPa, the exciton response of heterostructures (HS) had distinct pressure dependence under different twist angles. For HS-7.5°, PL peaks exhibited blue shift trends due to the changed band structure, in which the energy of direct transition from the K valley would increase under larger pressure. Whereas in HS-1.15°, the predominant moiré effect led to different exciton responses. The PL peaks of HS-1.15° showed continuous redshift with approximately linear dependence for intralayer excitons, which could be explained by the increased moiré potential under smaller interlayer spacing. The exciton dispersion band of the mini-Brillouin zone shifted to lower energy levels under the deepened moiré potential. At pressure higher than 1.1 GPa, effective enhancement of interfacial coupling in all twisted heterostructures dominated the exciton response in PL spectra [144]. However, conventional experiment methods to realize in-situ deformation like DAC are challenging to apply to moiré heterostructures at low temperatures. Zhao *et al.* [168] utilized an optical fiber tip in a cryogenic scanning near-field optical microscope (SNOM) to locally deform the sample and measure its background-free near-field optical response simultaneously, as illustrated in Fig. 11(h). The moiré potential of the near-zero-twisted WSe_2/WS_2 heterostructure increased under compressive deformation at 25 K, resulting in redshift of both intralayer and interlayer excitons. Under the maximum stress of 1.4 GPa, the sample obtained a modulation of 7 meV on the moiré potential coefficient V_j in Eq. (3.3). The maximum stress was limited by the damage threshold of the optical fiber tip. Therefore, this method requires a tip made from stronger materials to achieve a higher limit [168]. Cai *et al.* [161] utilized a nanopillar array placed under the hBN-encapsulated $MoSe_2/WSe_2$ heterostructures to introduce strain-enhanced coupling and strain gradient-induced funneling, which helped them to corroborate and develop the DAP IX dynamic model for understanding the primary origin of moiré localized interlayer excitons.

Moiré system combined with other elements would facilitate more fertile physics and deserve further investigation. Anđelković *et al.* [169] discussed the supermoiré (SM) resulting from two slightly misaligned interfering moiré patterns in the trilayer system. They concentrated on graphene encapsulated by hBN and quantitatively described the angle-dependent SM effects that led to electronic spectrum reconstruction, velocity suppression and spatial electron redistribution. Fitzgerald *et al.* [34] studied twist-angle-tunable moiré exciton polaritons resulting from hybridization between moiré intralayer excitons and photons in the strong coupling regime. They focused on twisted AA-stacked $MoSe_2/WSe_2$ heterostructures integrated within a Fabry–Pérot cavity.

They theoretically predicted the delocalized nature of the new hybrid light-exciton states and the optical responses of moiré exciton polaritons including exciton-light coupling, polariton energy and the number of polariton branches, which could be modulated by twist angle and cavity [34]. Moiré patterns have also prompted new progress in diverse fields. For example, moiré phonon physics derived from the atomic stress redistribution and folding effects of phonon dispersion in twisted 2D materials can drastically regulate the lattice vibration modes and thermal transport properties [91]. Besides, a variety of researches involved with moiré structures have been reported like gap solitons in parity–time symmetric moiré optical lattice [179], and moiré bilayer hyperbolic metasurface with highly controllable electromagnetic responses [180]. These research efforts are expected to pave the way to realize flat bands and localized states at arbitrary frequencies for multifunctional devices.

4 Correlated electronic states in moiré superlattice

Moiré superlattice in vdW heterostructures provides a general and promising solid-state platform for exploring and engineering correlated electronic states, supported by the strong periodic moiré potential with the flat electronic band. The core of the flat band lies in the comparability between the electron–electron interaction U and the electronic bandwidth W under sufficient narrow electronic bands, enabling the effects of Coulomb interactions to become pronounced in the system [181]. We can consider a simplified model of a two-dimensional electron gas in a periodic potential with a period λ, accompanied with the formation of a set of electronic minibands. For the lowest electronic miniband, it can be estimated that $U \approx \frac{e^2}{4\pi\varepsilon\lambda}$ and $W \approx \frac{\hbar^2\pi}{2m_e^*\lambda^2}$, where ε and m_e^* are the effective dielectric constant and electron effective mass, respectively. Strong correlation would become achievable when the ratio of electron-electron interaction to electronic bandwidth satisfies $U/W > 1$, which needs sufficient large $m_e^*\lambda$ [181]. The theoretical analysis of such systems must consider the correlated electronic effects instead of one electron approximation, which can trigger abundant quantum many-body states such as quantum anomalous Hall insulators and high-temperature superconductivity [118, 182]. A comprehensive understanding of such exotic physics based on strong electronic correlations requires both in-depth theory and experiment researches that complement each other. In a moiré superlattice, the electronic correlated effects would be enhanced under a large λ with reduced bandwidth W, which can be achieved by a small twist angle θ. Since the correlated insulator [59] and unconventional superconductivity [60] were observed in magic-angle graphene superlattice by Cao and co-workers, a wealth of moiré-system-based correlated electronic states in twisted vdW heterostructures has been reported [61, 129–131, 181, 183–188].

A real moiré system based on van der Waals heterostructures possesses more complexity beyond the simplified model shown above. Flat bands in the graphene-based heterostructures appear only at a discrete set of magic angles [123, 127], limiting the tunability of the strongly correlated systems. A sufficiently strong moiré effects require effective interlayer coupling between the constituent materials. Besides, a small enough twist angle provides a large λ but simultaneously brings about atomic reconstruction [132, 140], which would decrease the homogeneity of the moiré superlattice. Given these factors, TMD moiré heterostructures are supposed to offer an ideal system for the exploration of quantum many-body phenomena thanks to their strong light–matter interactions, considerable moiré potential and the reduced degeneracy arising from the coupled spin-valley index [128, 131, 181]. The electronic band structures of TMDs with relatively large effective mass ($m_e^* \approx 0.5m_0$, with m_0 as the free electron mass) facilitate flat band features and many-body effects [181]. Wu *et al.* [118] have presented that TMD moiré flat bands could exist over a range of twist angles (smaller than around 3.5°), enabling continuous tuning of correlation effects. They used the continuum model to describe the low-energy electrons in the moiré superlattice, in which the Hamiltonians were spatially periodic under effective moiré potential [64, 118]. The moiré band Hamiltonian for twisted TMDs heterobilayers had only two low-energy valence bands when the chemical potential was within the topmost valence bands, and could be mapped to triangular-lattice single-band Hubbard models with the Wannier wave function localized in one of the moiré potential extremum positions. The estimated hopping parameters t (related to the bandwidth W) and on-site Coulomb repulsion energy U (sensitive to the effective dielectric constant ε) both varied with the moiré period, resulting in a correlation strength that could be modulated over a wide range by twist angle. The relatively strong on-site repulsion would suppress double occupation of one moiré site when satisfying $U \gg t$, and therefore the Mott insulator ground state was predicted at hole half-filling (filling factor $v = 1$ considering the Hubbard model spin degeneracy, signifying one electron per moiré unit cell) [118]. Hubbard model is a simple theoretical model of interacting quantum particles in a lattice, which is considered to be paradigmatic in the physics of complex quantum many-body effects [129, 189, 190]. The TMDs moiré superlattices are regarded as an analogue quantum simulator of the Hubbard model with widely tunable parameters like bandwidth, interaction strength and band filling, which could play an important role in revealing the physics of various strongly interacting quantum particles [118, 128–131, 183, 191]. Wang *et al.*

[128] have reported the observations of the correlated insulator and zero-resistance regions in bilayer WSe_2 under twist angles ranging from 4 to 5.1°, indicating the continuously tunable collective phases in the TMD-based moiré system. Utilizing transport measurements, the effective electronic interactions U/W here were demonstrated to be tunable by external electric field and doping, driving a continuous metal-insulator transition (MIT) at near half-filling of the first moiré subband (one hole/electron per superlattice site) [183, 191]. The realization of the highly controllable triangular-lattice Hubbard model offers new avenues in exploring the correlation insulating phase transitions [191] that would potentially relate to exotic states such as quantum spin liquids [192, 193] and unconventional superconductivity [194]. Furthermore, TMDs moiré superlattice are expected to provide a promising platform for engineering novel correlated states, such as emerging correlated valley and spin physics thanks to the layer-valley-spin locking in TMDs [165, 185, 195].

The strong light–matter interactions of TMD heterostructures enable optical spectroscopy measurements to detect the strongly correlated phases, complementary to the traditional transport measurements [93, 181]. Regan *et al.* [181] have realized the optical detection of strongly correlated phases in near-zero twisted WSe_2/WS_2 heterostructures. They developed a novel measuring technique called optically detected resistance and capacitance (ODRC) [Fig. 12(a)], which could avoid the large contact resistances that impeded direct electrical transport measurements. As shown in Fig. 12(b), they observed the Mott insulating state at hole doping factor $v = 1$ ($n = n_0$; n_0 was the moiré supercell density) and additional insulating states at $v = 1/3$ ($n = n_0/3$) and $v = 2/3$ ($n = 2n_0/3$) in the heterostructures with moiré period $\lambda \approx 8$ nm at 3 K. The additional insulating states were attributed to generalized Wigner crystallization of holes in the moiré superlattice, where holes tried to avoid simultaneous occupation of adjacent sites [Fig. 12(c)]. The emergence of generalized Wigner crystallization arises from the relatively large inter-site interaction compared with the moiré miniband bandwidth, indicating the necessary of an extended Hubbard model that considers inter-site (long-range) interactions in addition to on-site (short-range) interactions in TMDs moiré superlattice [181]. Tang et al. [129] have also reported the observation of Mott insulating state in aligned WSe_2/WS_2 heterobilayers using the close-cycle cryostat magneto-optical measurements. The Mott insulating state occurred at half-filling of the first hole moiré band in the limit of $U/t \gg 1$ with antiferromagnetic Curie–Weiss behaviour [Figs. 12(d) and (e)], suggesting the antiferromagnetic interaction between the moiré band holes. Xu and co-workers [130] have observed nearly two dozen correlated insulating states at several fractional fillings of WSe_2/WS_2 moiré superlattice. They utilized a new optical sensing method based on dielectric-sensitive excited-state excitons in WS_2 monolayer as a probe of correlated states. As depicted in Fig. 12(f), the cascade insulating states with energy ordering nearly symmetric about filling factor $v = 1/2$ (half a particle per moiré supercell) were attributed to a series of charge-ordered states ranging from generalized Wigner crystals to charge density waves, which further corroborated the remarkable long-range interactions in TMD-based moiré systems.

Shimasaki *et al.* [131] have reported the incompressible electronic states probed by the exciton-polariton resonances in a long-period moiré superlattice. They fabricated a $MoSe_2$/hBN/$MoSe_2$ homobilayer with $\lambda = 24$ nm and a large r_s parameter ($r_s \geqslant 14$, the ratio of interaction energy to kinetic energy). The inserted hBN layer weakened the moiré potential and increased the on-site interaction strength, making the homobilayer moiré system a unique regime beyond the standard Fermi-Hubbard model. They controlled the hybridization as well as the doping of the top and bottom layers independently. The hybridization between intralayer and interlayer excitons with opposite dipole moments was regulated through electric-field-dependent coherent carrier tunneling. The charging configuration of the two layers could be simultaneously detected by the attractive polaron (AP) and repulsive polaron (RP) branches in the differential reflectance spectrum due to the dynamical screening of excitons by itinerant carriers. Negative compressibility was observed as the top gate voltage increased while the back gate fixed, manifesting as the depletion of electrons from the bottom layer due to the intralayer exchange interaction [Fig. 12(g)], indicating the prominent electron–electron interactions at high electron densities [131]. In the low-electron-density regime at half-filling of the lowest moiré subband ($v = 1/2$), abrupt collective interlayer transfer of electrons was observed with resilience towards electric-field-induced charge redistribution, as shown in Fig. 12(i). This result suggested the existence of Mott-like incompressible electronic states, which could be accommodated in either the top or the bottom $MoSe_2$ layer. Similar interaction-induced incompressible electronic states with abrupt phase transitions also appeared for other doping levels equal to an integer multiple of the moiré supercell density. This kind of moiré system was expected to act as a new platform for studying the interaction between dipolar excitons and electrons confined to flat bands, like Bose–Fermi mixtures [131].

As mentioned above, TMDs moiré superlattice have emerged as an ideal system for studying correlated electronic physics with high tunability, where the onsite Coulomb interaction U and the nearest-neighbour hopping parameter t are controllable by varying twist angle [128] and electric field [183, 191]. Apart from these methods, Wang *et al.* [187] and Chen *et al.* [185] have

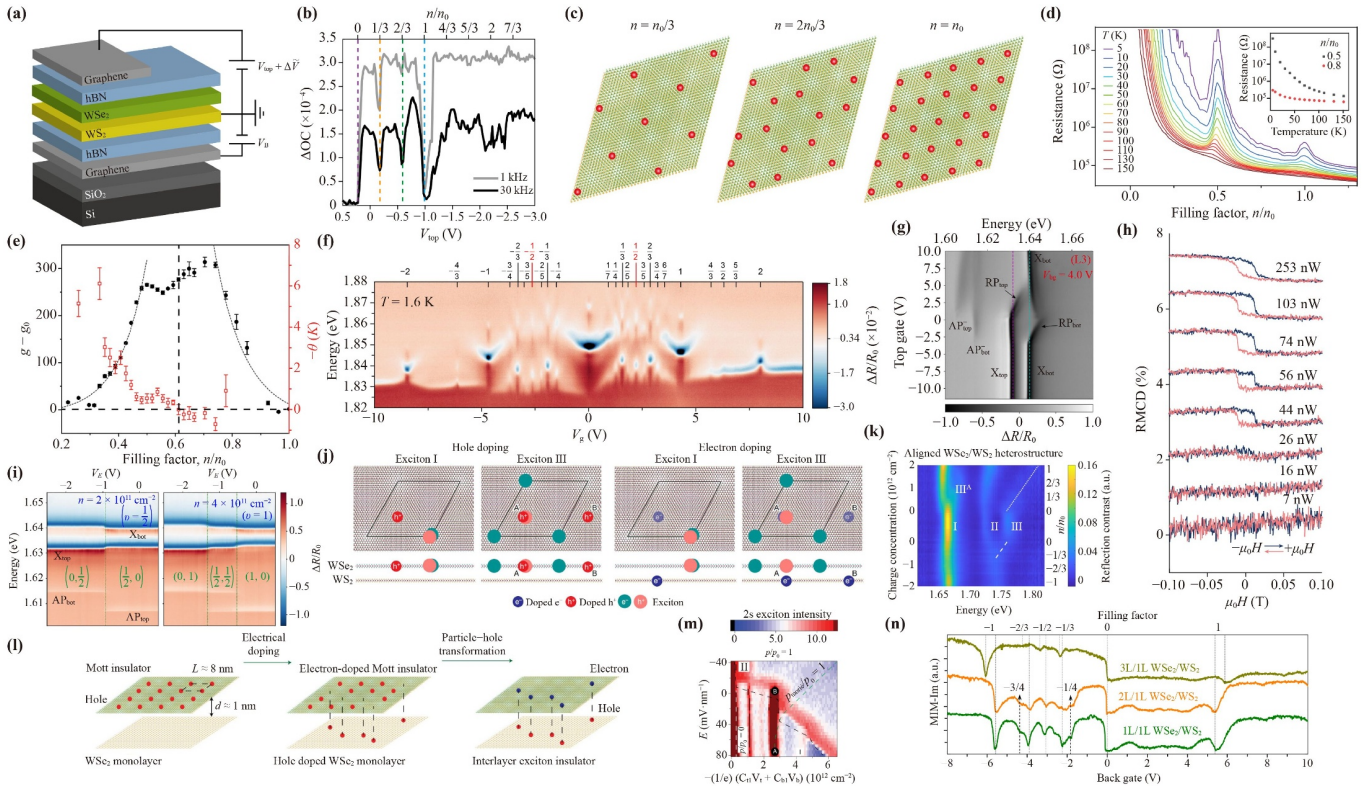

Fig. 12 Correlated electronic states in moiré systems. **(a)** Illustration of a near-zero twisted WSe_2/WS_2 heterostructure device used for an ODRC measurement. A small a.c. bias ($\Delta\tilde{V}$) leads to charge redistribution between the region covered by top gate and the uncovered region, which is detected via the change in the optical reflectivity of the WSe_2 exciton in the uncovered region. **(b)** The doping-dependent Mott insulating states and Wigner crystal of devices in (a) probed by optical contrast reflectance ΔOC. **(c)** Illustrations of generalized Wigner crystal and Mott insulator states in a WSe_2/WS_2 moiré superlattice. **(d)** Two-terminal resistance of 60° aligned WSe_2/WS_2 bilayers as a function of filling factor at different temperatures. The inset shows the temperature-dependent resistance at two different filling factors. **(e)** Dependence of the magnetic susceptibility $g–g_0$ (left axis, black filled symbols) on the filling factor at 1.65 K and Weiss constant θ (right axis, red empty symbols) in 60° aligned WSe_2/WS_2 bilayers, with $n_0/2$ as the density of moiré supercell. Here $g–g_0$ is the difference of Landé g-factor between excitons in the moiré superlattice and bare excitons. **(f)** Nearly two dozen insulating states and their energy ordering in a WSe_2/WS_2 moiré heterostructure at 1.6 K probed by the 2s exciton in the sensor. The top axis shows the proposed filling factor for the insulating states. **(g)** Gate dependence of differential reflectance spectrum of $MoSe_2$/hBN/$MoSe_2$ with back gate fixed at 4 V. **(h)** Observation of optically induced ferromagnetism at near $\upsilon = -1/3$ filling of WS_2/WSe_2 measured by power-dependent RMCD at 1.6 K. **(i)** Electric field dependence of differential reflectance spectrum of $MoSe_2$/hBN/$MoSe_2$ at two fixed filling factors, with charge configuration of the top and bottom layer indicated by $(\upsilon_{top}, \upsilon_{bot})$ in green. **(j)** Schematic of moiré exciton I and III under hole and electron doping. **(k)** Doping-dependent reflection contrast spectrum of a WSe_2/WS_2 moiré superlattice shows distinct behaviour for WSe_2 moiré excitons I, II and III. **(l)** The schematic of hole distributions for the double-layer system of (left panel) the Mott insulator at point A of (m), (middle panel) interlayer exciton insulator at point B of (m), and (right panel) the particle-hole transformation of the doped Mott insulator state at point B of (m) to form the interlayer exciton insulator. **(m)** The phase diagram of the correlated interlayer exciton insulator in the double-layer system detected by the WSe_2 monolayer 2s exciton signal. **(n)** MIM spectra as a function of gate voltage for the moiré superlattice of 1L/1L, 2L/1L and 3L/1L WSe_2/WS_2 at 10 K, respectively. (a–c) Reproduced with permission from Ref. [181]. (d, e) Reproduced with permission from Ref. [129]. (f) Reproduced with permission from Ref. [130]. (g, i) Reproduced with permission from Ref. [131]. (h) Reproduced with permission from Ref. [187]. (j, k) Reproduced with permission from Ref. [186]. (l, m) Reproduced with permission from Ref. [188]. (n) Reproduced with permission from Ref. [185].

introduced other factors that could modulate the electronic correlation in TMDs moiré superlattice. The former studied the impact of optical excitation on the correlated electronic states in WS_2/WSe_2 heterobilayers. They showed that optical excitation enhanced magnetic interaction between moiré-trapped carriers and consequently led to ferromagnetic order [187]. The hysteresis loop at low filling factor $\upsilon = -1/3$ measured by the reflective magnetic circular dichroism (RMCD) at $T = 1.6$ K, signified the emergence of ferromagnetic order due to

long-range spin-spin interaction in generalized Wigner crystal state. The power dependence of RMCD responses [Fig. 12(h)] indicated the remarkable optical tuning of spin–spin interaction strength between moiré-trapped holes mediated by itinerant photoexcited excitons, which could realize the modulation of magnetic phases [187]. Chen and co-workers [185] introduced the layer degree of freedom in the angle-aligned WSe_2/WS_2 heterostructure with WSe_2 varying from monolayer to trilayer, in order to systematically tune both electronic flat bands and moiré exciton bands. The systematic changes including emergent exciton resonances and increased resonance energy separations in the differential reflectance spectra suggested that moiré coupling was strongly confined at the WSe_2/WS_2 interface with limited out-of-plane extension. In the multilayer WSe_2/1L WS_2, the added WSe_2 layer(s) could affect the hybridization between moiré excitons and the interlayer-like hybrid exciton. Microwave impedance microscopy (MIM) measurements demonstrated the tunability of the electron correlation by layer degree of freedom, as illustrated in Fig. 12(n). As the layer number of WSe_2 increased, the correlated insulating states became fewer and less pronounced in the MIM spectra accompanied with reduced Mott transition temperature. The reduction of transition temperature indicated the weaker inter-site and on-site electron interaction strengths, which could be explained by reduced interfacial Coulomb interaction under enhanced dielectric screening and the increased kinetic energy originated from the larger bandwidth of the flat band in multilayer WSe_2/1L WS_2. It is worth noting that even the weakened electron correlation (with the Mott transition temperature about 60 K for 3L WSe_2/1L WS_2) reported here was still stronger than that in the graphene moiré system (with transition temperature of about 4 K).

Taking advantage of the rich excitonic physics in TMD vdW heterostructures, several new correlated insulating phases of excitons have been reported in recent years. Zhang *et al.* [188] integrated the moiré superlattice into a "double-layer system" composed of a near-aligned WS_2/WSe_2 heterobilayer (moiré superlattice) and a WSe_2 monolayer separating by an ultrathin hBN layer, aiming at realizing flat electronic bands and strong interlayer electron–hole interactions simultaneously. They controlled the total hole concentration p and the average electric field independently. The electric field determined the hole distribution between the WSe_2 monolayer p_{mono} and the WSe_2 from moiré bilayer p_{bi}, following a relation of $p = p_{\mathrm{bi}} + p_{\mathrm{mono}}$. As finite hole density was distributed in both WSe_2 layers, a higher total p should be required to achieve the moiré bilayer Mott insulator state ($p_{\mathrm{bi}} = p_0$, with p_0 denoting one hole per moiré lattice site), while actually a stable correlated insulator state appeared at $p/p_0 = 1$ [Fig. 12(m)]. The unexpectedly low p originated from the strong interlayer Coulomb interaction preventing the holes in the WSe_2 monolayer from occupying the same sites with holes from the WS_2/WSe_2 moiré bilayer. This correlated insulating phase was interpreted as an interlayer exciton insulator through particle-hole transformation, where holes in the WSe_2 monolayer and the doped electrons in the WS_2/WSe_2 moiré bilayer could form tightly bound interlayer excitons, as depicted in Fig. 12(l). This interlayer exciton insulator would evolve to other correlated phases such as metal-like optical response under sufficient high p_{mono}, and could potentially form exciton condensate and counterflow superfluidity [188]. Recently, Xiong *et al.* [196] have also reported an exciton incompressible state as a bosonic correlated insulator in WSe_2/WS_2 moiré superlattices persisting above 30 K. Using a unique pump-probe spectroscopy method to independently tune the charge and exciton density through electrostatic gating and pump light respectively, they achieved continuous transitions between the bosonic correlated insulating phase and the electron correlated insulator where excitons avoid electron-occupied sites under on-site electron–exciton repulsion. These excitonic correlated states observed in semiconducting moiré superlattices open up new ways for manipulating emergent bosonic phases and many-body interactions involving both fermions and bosons [196].

The moiré excitons behaviours under optical measurements with limited spatial resolutions are commonly described by a continuum model [118, 197], which considers the center-of-mass motion of the pristine exciton modulated by the effective moiré potential, assuming that the internal spatial electron-hole correlations from the pristine single layers are retained [186]. The prevailing effective continuum model is limited to large moiré periods and cannot capture the microscopic nature of exciton states in real moiré superlattice, where electrons and holes could experience different moiré effects and exhibit distinct spatially modulated moiré flat bands [133, 139, 198]. Combining large-scale first-principles GW-BSE predictions with micro-reflection spectroscopy, Naik and co-workers [186] have identified various exciton states with distinct electron–hole correlations in rotationally aligned WSe_2/WS_2 reconstructed moiré superlattice at $T = 1.6$ K, including a Wannier-type exciton with lowest energy and a new-found intralayer charge-transfer exciton with higher resonance energy. Different from the Wannier-type moiré exciton with tightly correlated electron and hole, the intralayer charge transfer exciton had electron and hole densities distributed with about 5 nm separation in the WSe_2 layer. The distinct spatial electron–hole distributions resulted in different carrier densities and magnetic-field dependence. As shown in Fig. 12(k), the moiré peak I (Wannier exciton) was almost unaffected by doping except for the formation of Mott state at one doped hole per moiré unit cell, while the intralayer charge exciton resonance (the moiré peak III) was strongly modulated by carrier doping due to the

Coulomb interactions and large dipole of charge-transfer exciton [Fig. 12(j)]. The attractive electron–hole interaction between doped electrons at local A led to the emergent peak III^A close to peak I. As electron doping increased, the peak III^A showed blueshifts and consequently reduced the resonant hybridization between peak I and peak III^A, resulting in the weakened oscillator strength. The brief enhanced oscillator strength of the peak III^A at around 1/3 and 2/3 filling was ascribed to the reduced screening of correlated states. The peak II exhibited a mixed character. The non-trivial intralayer charge-transfer exciton state with specific spatial characters can be more easily modified and dissociated, suggesting a new approach to engineering many-body physics and desirable optoelectronic nanodevices based on moiré system [186]. Such charge-transfer excitons with long lifetimes have lately been reported in monolayer WSe_2/twisted bilayer graphene (TBG) by Hu *et al.* [199], due to strongly asymmetric interlayer Coulomb interactions under a relatively large moiré wavelength compared to the exciton size. At a quite small twist angle ($\theta = 0.6°$), they observed Rydberg moiré excitons where the accumulated charges in TBG strongly attracted the loosely bound 2s excitons in WSe_2, resembling the Rydberg atom trapped by arrays of optical tweezers. The moiré system brings about highly tunable properties and mutual interactions of the spatially confined Rydberg excitons, demonstrating great potential for the applications of quantum information processing and quantum simulations based on the excitonic Rydberg states in solid-state systems [199].

5 Conclusions and outlook

This review systematically summarizes the recent progress in twistronic and moiré exciton physics in van der Waals heterostructures that consist of 2D semiconducting materials. The interlayer twist angle can act as an effective knob to modulate the electronic structures and optical properties through interlayer interactions and momentum-space mismatches. The most concerning aspect is exciton physics, where the exciton properties such as binding energy, static electric dipole, emission intensities of different excitonic species [87, 88] and degree of spin-valley polarization [77], are all controlled by the interlayer twist angle. Moreover, the interlayer twist in momentum space also affect the excitonic dynamics including formation, transport and recombination processes with complex mechanisms that involve localized and hybridized valleys [52, 79, 85]. The twist-angle-tunable physics is significantly enriched when the moiré effects are considered, which still lacks a comprehensive model to understand moiré excitons in various systems. Early theoretical analyses have predicted the Moiré Brillouin zone of superlattice structures as well as the moiré patterns-induced spatial modulations of exciton energy and wave function symmetry, which will lead to some novel phenomena such as splitting resonance energies, spatially modulated optical selection rules and localization of moiré excitons, etc. [49, 52]. The harmonic moiré potential model [65] describes the moiré excitons as particles moving under approximated potentials with spatial periodicity. This model is suitable for heterostructures with relatively large band edge offsets, but is not sufficient to capture the excitonic physics in systems with near-resonant band edges, where interlayer and intralayer hybridization through carrier tunneling should be considered [146]. Apart from the moiré superlattice under small twist angles, the enhanced moiré exciton features also appear in high-angle twisted heterostructures due to the umklapp processes in commensurate moiré reciprocal lattice [135, 137]. Moiré systems based on vdW heterostructures exhibit expanded properties and dynamic tunability in conjunction with external factors, such as electric fields, carrier doping and strain, which would promote an in-depth understanding of moiré physics and pave the way to promising applications. Recently, the enhanced electron–electron interactions and flat band features in moiré vdW heterostructures have facilitated research on strongly correlated electronic states at a few certain filling factors, such as Mott insulating states, generalized Wigner crystal and other correlated phases. These studies are expected to experimentally realize novel quantum phenomena like fractional quantum anomalous Hall effects and spin-liquid states [118].

In this review, we mainly focus on the excitonic behaviours in twisted vdW heterostructures revealed by optical spectroscopy, which only covers a part of new physics in twistronics and moiré superlattice. There are still a large variety of controversies and challenges in current research that need to be tackled, even within this certain topic. A comprehensive model to understand the excitonic physics modulated by moiré pattern has yet to be established. Excitons presented distinct behaviours in different twisted heterostructure systems. On one hand, such variations are possibly caused by the randomness of twisted heterostructures, which require preparation and detection technology with high precision. On the other hand, the impacts of the moiré pattern on electronic band structures and optical properties in vdW heterostructures are still not clear, such as strain distributions and atomic reconstructions under lattice mismatches [92, 143]. Besides, the twist-angle-dependent electron-phonon coupling strength in combination with moiré phonon physics in twisted 2D vdW materials might deserve further study [91]. The carrier dynamics and transport influenced by interlayer twist show much more complicated mechanisms other than interlayer momentum mismatch. For example, the ultrafast interlayer charge transfer processes are relatively robust due to the mixed valley serving as an intermediate in some TMD

heterostructures, whereas they show obvious twist angle dependence in other cases [85, 86]. Interlayer stretching and shift caused by atomic reconstructions are also expected to affect the carrier dynamics through generating extra channels [79]. In addition, moiré excitons exhibit splitting resonance energies and localization introduced by moiré periodic potential. The cascade transitions between moiré interlayer excitons with different energies have been reported recently, suggesting the spatial overlap between the multiple IX minibands in TMDs-based moiré superlattice [200]. The links between excitons distributed in different moiré sites and different energies still need in-depth exploration. Moreover, the study on strong moiré excitonic features observed in high-angle commensurately twisted bilayers at several twist angles is still preliminary but interesting, since these cases are widely found in randomly stacked TMD bilayers without the need for deliberate alignment [137]. Apart from the moiré exciton properties and dynamics, correlated electronic states in TMDs moiré superlattice have spurred great interest and generated many open questions in recent years. The TMDs-based moiré systems working as designed quantum simulation platforms provide many opportunities for new quantum states. It is inspiring that the strong light–matter interactions of TMDs allow optical probing methods such as ODRC [181] and differential reflectance spectrum [131, 188], which utilize excitons as sensors. However, the microscopic mechanisms of the interplay between correlated electrons and excitons remain obscure. The nature of various correlated states identified at certain filling factors needs further investigation.

The optical measurement techniques used for probing moiré excitons so far still have limited spatial resolutions in the far-field limit, which are unable to detect the excitonic physics within an individual moiré supercell [93]. It has been theoretically predicted that electrons, holes, and excitons with different energies have distinct spatial distributions and modulated band structures in moiré superlattice, which are challenging for conventional optical probing methods, especially considering the spatial inhomogeneity and defects. Therefore, non-invasive experimental techniques with sufficiently high spatial- and momentum-resolutions are indispensable for mapping the exact charge distributions and revealing their microscopic nature and mutual correlations in moiré systems. Techniques like scanning near-field optical microscopy [201], PFM [58], STM spectroscopy [202], and nano-ARPES [153, 203] are promising for future explorations that might eliminate ambiguity in early researches. Besides, the heterogeneity and intricate many-body effects of moiré excitons can possibly be captured by the optical 2D coherent spectroscopy (2DCS), leaving a wealth of opportunities for exploring the interaction between moiré superlattice and excitonic quantum dynamics [204].

Moiré system based on vdW heterostructure inherits the high tunability and ability to be customized in multiple ways. Moiré vdW heterostructures combined with various external factors such as cavity and strain are interesting and intriguing for further investigations. For instance, strain engineering of twisted vdW heterostructures can cause efficient tunning of optoelectronic properties due to the nano-scale structures of the moiré pattern [167]. Moiré superlattice can also couple to multiple 2D vdW materials with different stacking sequences and orders to construct vdW heterostructure possessing new electronic and photonic physics, including controllable ferroelectricity [20, 81, 173, 205] and magnetism [206]. Beyond the most studied TMDs and graphene reviewed here, the material choice to fabricate a vdW heterostructure is wider regardless of lattice constants matching. The research on twisted vdW heterostructures will prompt engineering artificial materials with moiré superlattice, providing a fascinating platform for exploring emerging quantum phenomena and valuable applications.

Declarations The authors declare that they have no competing interests and there are no conflicts.

Acknowledgements The authors are grateful for financial support from the National Natural Science Foundation of China (Nos. 62105364 and 62075240); the Science and Technology Innovation Program of Hunan Province (No. 2021RC2068); and the Scientific Researches Foundation of National University of Defense Technology (No. ZK22-16).

References

1. M. Osada and T. Sasaki, Two-dimensional dielectric nanosheets: Novel nanoelectronics from nanocrystal building blocks, *Adv. Mater.* 24(2), 210 (2012)
2. M. Xu, T. Liang, M. Shi, and H. Chen, Graphene-like two-dimensional materials, *Chem. Rev.* 113(5), 3766 (2013)
3. K. S. Novoselov, D. Jiang, F. Schedin, T. J. Booth, V. V. Khotkevich, S. V. Morozov, and A. K. Geim, Two-dimensional atomic crystals, *Proc. Natl. Acad. Sci. USA* 102(30), 10451 (2005)
4. A. K. Geim and K. S. Novoselov, The rise of graphene, *Nat. Mater.* 6(3), 183 (2007)
5. P. Vogt, P. De Padova, C. Quaresima, J. Avila, E. Frantzeskakis, M. C. Asensio, A. Resta, B. Ealet, and G. Le Lay, Silicene: Compelling experimental evidence for graphenelike two-dimensional silicon, *Phys. Rev. Lett.* 108(15), 155501 (2012)
6. K. Watanabe, T. Taniguchi, and H. Kanda, Direct-bandgap properties and evidence for ultraviolet lasing of hexagonal boron nitride single crystal, *Nat. Mater.* 3(6), 404 (2004)
7. L. Song, L. Ci, H. Lu, P. B. Sorokin, C. Jin, J. Ni, A. G. Kvashnin, D. G. Kvashnin, J. Lou, B. I. Yakobson,

and P. M. Ajayan, Large scale growth and characterization of atomic hexagonal boron nitride layers, *Nano Lett.* 10(8), 3209 (2010)
8. H. Liu, A. T. Neal, Z. Zhu, Z. Luo, X. Xu, D. Tománek, and P. D. Ye, Phosphorene: An unexplored 2D semiconductor with a high hole mobility, *ACS Nano* 8(4), 4033 (2014)
9. L. Li, Y. Yu, G. J. Ye, Q. Ge, X. Ou, H. Wu, D. Feng, X. H. Chen, and Y. Zhang, Black phosphorus field-effect transistors, *Nat. Nanotechnol.* 9(5), 372 (2014)
10. C. Ataca, M. Topsakal, E. Aktürk, and S. Ciraci, A comparative study of lattice dynamics of three- and two-dimensional MoS_2, *J. Phys. Chem. C* 115(33), 16354 (2011)
11. R. Ganatra and Q. Zhang, Few-layer MoS_2: A promising layered semiconductor, *ACS Nano* 8(5), 4074 (2014)
12. Q. H. Wang, K. Kalantar-zadeh, A. Kis, J. N. Coleman, and M. S. Strano, Electronics and optoelectronics of two-dimensional transition metal dichalcogenides, *Nat. Nanotechnol.* 7(11), 699 (2012)
13. C. Gong, H. Zhang, W. Wang, L. Colombo, R. M. Wallace, and K. Cho, Band alignment of two-dimensional transition metal dichalcogenides: Application in tunnel field effect transistors, *Appl. Phys. Lett.* 103(5), 053513 (2013)
14. H. J. Chuang, X. Tan, N. J. Ghimire, M. M. Perera, B. Chamlagain, M. M. C. Cheng, J. Yan, D. Mandrus, D. Tománek, and Z. Zhou, High mobility WSe_2 p- and n-type field-effect transistors contacted by highly doped graphene for low-resistance contacts, *Nano Lett.* 14(6), 3594 (2014)
15. Y. Ye, Z. J. Wong, X. Lu, X. Ni, H. Zhu, X. Chen, Y. Wang, and X. Zhang, Monolayer excitonic laser, *Nat. Photonics* 9(11), 733 (2015)
16. Y. K. Luo, J. Xu, T. Zhu, G. Wu, E. J. McCormick, W. Zhan, M. R. Neupane, and R. K. Kawakami, Opto-valleytronic spin injection in monolayer MoS_2/few-layer graphene hybrid spin valves, *Nano Lett.* 17(6), 3877 (2017)
17. B. Radisavljevic, M. B. Whitwick, and A. Kis, Integrated circuits and logic operations based on single-layer MoS_2, *ACS Nano* 5(12), 9934 (2011)
18. J. S. Ross, P. Rivera, J. Schaibley, E. Lee-Wong, H. Yu, T. Taniguchi, K. Watanabe, J. Yan, D. Mandrus, D. Cobden, W. Yao, and X. Xu, Interlayer exciton optoelectronics in a 2D heterostructure p–n junction, *Nano Lett.* 17(2), 638 (2017)
19. C. Gao, Q. Nie, C. Y. Lin, F. Huang, L. Wang, W. Xia, X. Wang, Z. Hu, M. Li, H. W. Lu, Y. C. Lai, Y. F. Lin, J. Chu, and W. Li, Touch-modulated van der Waals heterostructure with self-writing power switch for synaptic simulation, *Nano Energy* 91, 106659 (2022)
20. G. D. Wenbiao Niu, Z. Jia, X. Q. Ma, J. Y. Zhao, K. Zhou, S. T. Han, C. C. Kuo, and Y. Zhou, Recent advances in memristors based on two-dimensional ferroelectric materials, *Front. Phys.* 19(1), 13402 (2024)
21. A. Chaves, J. G. Azadani, H. Alsalman, D. R. da Costa, R. Frisenda, A. J. Chaves, S. H. Song, Y. D. Kim, D. He, J. Zhou, A. Castellanos-Gomez, F. M. Peeters, Z. Liu, C. L. Hinkle, S.-H. Oh, P. D. Ye, S. J. Koester, Y. H. Lee, P. Avouris, X. Wang, and T. Low, Bandgap engineering of two-dimensional semiconductor materials, *npj 2D Mater. Appl.* 4, 29 (2020)
22. Y. Wang, Z. Nie, and F. Wang, Modulation of photocarrier relaxation dynamics in two-dimensional semiconductors, *Light Sci. Appl.* 9(1), 192 (2020)
23. S. Wu, J. S. Ross, G. B. Liu, G. Aivazian, A. Jones, Z. Fei, W. Zhu, D. Xiao, W. Yao, D. Cobden, and X. Xu, Electrical tuning of valley magnetic moment through symmetry control in bilayer MoS_2, *Nat. Phys.* 9(3), 149 (2013)
24. I. Lee, S. Rathi, D. Lim, L. Li, J. Park, Y. Lee, K. S. Yi, K. P. Dhakal, J. Kim, C. Lee, G. H. Lee, Y. D. Kim, J. Hone, S. J. Yun, D. H. Youn, and G. H. Kim, Gate-tunable hole and electron carrier transport in atomically thin dual-channel WSe_2/MoS_2 heterostructure for ambipolar field-effect transistors, *Adv. Mater.* 28(43), 9519 (2016)
25. J. Lee, K. F. Mak, and J. Shan, Electrical control of the valley Hall effect in bilayer MoS_2 transistors, *Nat. Nanotechnol.* 11, 421 (2016)
26. L. A. Jauregui, A. Y. Joe, K. Pistunova, D. S. Wild, A. A. High, Y. Zhou, G. Scuri, K. De Greve, A. Sushko, C. H. Yu, T. Taniguchi, K. Watanabe, D. J. Needleman, M. D. Lukin, H. Park, and P. Kim, Electrical control of interlayer exciton dynamics in atomically thin heterostructures, *Science* 366(6467), 870 (2019)
27. A. Chernikov, A. M. van der Zande, H. M. Hill, A. F. Rigosi, A. Velauthapillai, J. Hone, and T. F. Heinz, Electrical tuning of exciton binding energies in monolayer WS_2, *Phys. Rev. Lett.* 115(12), 126802 (2015)
28. P. V. Nguyen, N. C. Teutsch, N. P. Wilson, J. Kahn, X. Xia, A. J. Graham, V. Kandyba, A. Giampietri, A. Barinov, G. C. Constantinescu, N. Yeung, N. Hine, X. Xu, D. H. Cobden, and N. R. Wilson, Visualizing electrostatic gating effects in two-dimensional heterostructures, *Nature* 572(7768), 220 (2019)
29. Z. Peng, X. Chen, Y. Fan, D. J. Srolovitz, and D. Lei, Strain engineering of 2D semiconductors and graphene: From strain fields to band-structure tuning and photonic applications, *Light Sci. Appl.* 9(1), 190 (2020)
30. H. J. Conley, B. Wang, J. I. Ziegler, R. F. Jr Haglund, S. T. Pantelides, and K. I. Bolotin, Bandgap engineering of strained monolayer and bilayer MoS_2, *Nano Lett.* 13(8), 3626 (2013)
31. M. G. Harats, J. N. Kirchhof, M. Qiao, K. Greben, and K. I. Bolotin, Dynamics and efficient conversion of excitons to trions in non-uniformly strained monolayer WS_2, *Nat. Photonics* 14(5), 324 (2020)
32. Z. Li, Y. Lv, L. Ren, J. Li, L. Kong, Y. Zeng, Q. Tao, R. Wu, H. Ma, B. Zhao, D. Wang, W. Dang, K. Chen, L. Liao, X. Duan, X. Duan, and Y. Liu, Efficient strain modulation of 2D materials via polymer encapsulation, *Nat. Commun.* 11(1), 1151 (2020)
33. G. Luo, X. Lv, L. Wen, Z. Li, and Z. Dai, Strain induced topological transitions in twisted double bilayer graphene, *Front. Phys.* 17(2), 23502 (2022)
34. J. M. Fitzgerald, J. J. P. Thompson, and E. Malic, Twist angle tuning of moiré exciton polaritons in van der Waals heterostructures, *Nano Lett.* 22(11), 4468 (2022)

35. Y. Hoshi, T. Kuroda, M. Okada, R. Moriya, S. Masubuchi, K. Watanabe, T. Taniguchi, R. Kitaura, and T. Machida, Suppression of exciton–exciton annihilation in tungsten disulfide monolayers encapsulated by hexagonal boron nitrides, *Phys. Rev. B* 95(24), 241403 (2017)
36. A. K. M. Newaz, Y. S. Puzyrev, B. Wang, S. T. Pantelides, and K. I. Bolotin, Probing charge scattering mechanisms in suspended graphene by varying its dielectric environment, *Nat. Commun.* 3(1), 734 (2012)
37. A. Raja, A. Chaves, J. Yu, G. Arefe, H. M. Hill, A. F. Rigosi, T. C. Berkelbach, P. Nagler, C. Schüller, T. Korn, C. Nuckolls, J. Hone, L. E. Brus, T. F. Heinz, D. R. Reichman, and A. Chernikov, Coulomb engineering of the bandgap and excitons in two-dimensional materials, *Nat. Commun.* 8(1), 15251 (2017)
38. N. P. Wilson, W. Yao, J. Shan, and X. Xu, Excitons and emergent quantum phenomena in stacked 2D semiconductors, *Nature* 599(7885), 383 (2021)
39. K. F. Mak, C. Lee, J. Hone, J. Shan and T. F. Heinz, Atomically thin MoS_2: A new direct-gap semiconductor, *Phys. Rev. Lett.* 105, 136805 (2010)
40. Y. Li, A. Chernikov, X. Zhang, A. Rigosi, H. M. Hill, A. M. van der Zande, D. A. Chenet, E. M. Shih, J. Hone, and T. F. Heinz, Measurement of the optical dielectric function of monolayer transition-metal dichalcogenides: MoS_2, $MoSe_2$, WS_2, and WSe_2, *Phys. Rev. B* 90(20), 205422 (2014)
41. T. C. Berkelbach, M. S. Hybertsen, and D. R. Reichman, Theory of neutral and charged excitons in monolayer transition metal dichalcogenides, *Phys. Rev. B* 88(4), 045318 (2013)
42. D. Xiao, W. Yao, and Q. Niu, Valley-contrasting physics in graphene: Magnetic moment and topological transport, *Phys. Rev. Lett.* 99(23), 236809 (2007)
43. W. Yao, D. Xiao, and Q. Niu, Valley-dependent optoelectronics from inversion symmetry breaking, *Phys. Rev. B* 77(23), 235406 (2008)
44. T. Cao, G. Wang, W. Han, H. Ye, C. Zhu, J. Shi, Q. Niu, P. Tan, E. Wang, B. Liu, and J. Feng, Valley-selective circular dichroism of monolayer molybdenum disulphide, *Nat. Commun.* 3(1), 887 (2012)
45. W. Jin, P. C. Yeh, N. Zaki, D. Chenet, G. Arefe, Y. Hao, A. Sala, T. O. Mentes, J. I. Dadap, A. Locatelli, J. Hone, and R. M. Osgood, Tuning the electronic structure of monolayer graphene/MoS_2 van der Waals heterostructures via interlayer twist, *Phys. Rev. B* 92(20), 201409 (2015)
46. H. Yu, Y. Wang, Q. Tong, X. Xu, and W. Yao, Anomalous light cones and valley optical selection rules of interlayer excitons in twisted heterobilayers, *Phys. Rev. Lett.* 115(18), 187002 (2015)
47. J. P. Eisenstein and A. H. MacDonald, Bose–Einstein condensation of excitons in bilayer electron systems, *Nature* 432(7018), 691 (2004)
48. C. R. Dean, L. Wang, P. Maher, C. Forsythe, F. Ghahari, Y. Gao, J. Katoch, M. Ishigami, P. Moon, M. Koshino, T. Taniguchi, K. Watanabe, K. L. Shepard, J. Hone, and P. Kim, Hofstadter's butterfly and the fractal quantum Hall effect in moiré superlattices, *Nature* 497(7451), 598 (2013)
49. H. Yu, G. B. Liu, J. Tang, X. Xu, and W. Yao, Moiré excitons: From programmable quantum emitter arrays to spin–orbit coupled artificial lattices, *Sci. Adv.* 3(11), e1701696 (2017)
50. H. Guo, X. Zhang, and G. Lu, Shedding light on moiré excitons: A first-principles perspective, *Sci. Adv.* 6(42), eabc5638 (2020)
51. P. Rivera, K. L. Seyler, H. Yu, J. R. Schaibley, J. Yan, D. G. Mandrus, W. Yao, and X. Xu, Valley- polarized exciton dynamics in a 2D semiconductor heterostructure, *Science* 351(6274), 688 (2016)
52. Y. Wang, Z. Wang, W. Yao, G. B. Liu, and H. Yu, Interlayer coupling in commensurate and incommensurate bilayer structures of transition-metal dichalcogenides, *Phys. Rev. B* 95(11), 115429 (2017)
53. W. Ren, S. Lu, C. Yu, J. He, Z. Zhang, J. Chen, and G. Zhang, Impact of moiré superlattice on atomic stress and thermal transport in van der Waals heterostructures, *Appl. Phys. Rev.* 10(4), 041404 (2023)
54. Y. Jiang, S. Chen, W. Zheng, B. Zheng, and A. Pan, Interlayer exciton formation, relaxation, and transport in TMD van der Waals heterostructures, *Light Sci. Appl.* 10(1), 72 (2021)
55. Q. Tong, H. Yu, Q. Zhu, Y. Wang, X. Xu, and W. Yao, Topological mosaics in moiré superlattices of van der Waals heterobilayers, *Nat. Phys.* 13(4), 356 (2017)
56. C. Zhang, C. P. Chuu, X. Ren, M. Y. Li, L. J. Li, C. Jin, M. Y. Chou, and C. K. Shih, Interlayer couplings, Moiré patterns, and 2D electronic superlattices in MoS_2/WSe_2 hetero-bilayers, *Sci. Adv.* 3(1), e1601459 (2017)
57. Y. Pan, S. Fölsch, Y. Nie, D. Waters, Y. C. Lin, B. Jariwala, K. Zhang, K. Cho, J. A. Robinson, and R. M. Feenstra, Quantum-confined electronic states arising from the moiré pattern of MoS_2–WSe_2 heterobilayers, *Nano Lett.* 18(3), 1849 (2018)
58. L. J. McGilly, A. Kerelsky, N. R. Finney, K. Shapovalov, E. M. Shih, A. Ghiotto, Y. Zeng, S. L. Moore, W. Wu, Y. Bai, K. Watanabe, T. Taniguchi, M. Stengel, L. Zhou, J. Hone, X. Zhu, D. N. Basov, C. Dean, C. E. Dreyer, and A. N. Pasupathy, Visualization of moiré superlattices, *Nat. Nanotechnol.* 15(7), 580 (2020)
59. Y. Cao, V. Fatemi, A. Demir, S. Fang, S. L. Tomarken, J. Y. Luo, J. D. Sanchez-Yamagishi, K. Watanabe, T. Taniguchi, E. Kaxiras, R. C. Ashoori, and P. Jarillo-Herrero, Correlated insulator behaviour at half-filling in magic-angle graphene superlattices, *Nature* 556(7699), 80 (2018)
60. Y. Cao, V. Fatemi, S. Fang, K. Watanabe, T. Taniguchi, E. Kaxiras, and P. Jarillo-Herrero, Unconventional superconductivity in magic-angle graphene superlattices, *Nature* 556(7699), 43 (2018)
61. L. Li, M. Wu, and X. Lu, Correlation, superconductivity and topology in graphene moiré superlattice, *Front. Phys.* 18(4), 43401 (2023)
62. K. L. Seyler, P. Rivera, H. Yu, N. P. Wilson, E. L. Ray, D. G. Mandrus, J. Yan, W. Yao, and X. Xu, Signatures of moiré-trapped valley excitons in $MoSe_2$/WSe_2 heterobilayers, *Nature* 567(7746), 66 (2019)

63. B. Wu, H. Zheng, S. Li, J. Ding, J. He, Y. Zeng, K. Chen, Z. Liu, S. Chen, A. Pan, and Y. Liu, Evidence for moiré intralayer excitons in twisted WSe_2/WSe_2 homobilayer superlattices, *Light Sci. Appl.* 11(1), 166 (2022)
64. F. Wu, T. Lovorn, and A. H. MacDonald, Topological exciton bands in moiré heterojunctions, *Phys. Rev. Lett.* 118(14), 147401 (2017)
65. F. Wu, T. Lovorn, and A. H. MacDonald, Theory of optical absorption by interlayer excitons in transition metal dichalcogenide heterobilayers, *Phys. Rev. B* 97(3), 035306 (2018)
66. H. Yu, G. B. Liu, and W. Yao, Brightened spin-triplet interlayer excitons and optical selection rules in van der Waals heterobilayers, *2D Mater.* 5, 035021 (2018)
67. C. Jin, E. C. Regan, D. Wang, M. Iqbal Bakti Utama, C. S. Yang, J. Cain, Y. Qin, Y. Shen, Z. Zheng, K. Watanabe, T. Taniguchi, S. Tongay, A. Zettl, and F. Wang, Identification of spin, valley and moiré quasi-angular momentum of interlayer excitons, *Nat. Phys.* 15(11), 1140 (2019)
68. J. He, K. Hummer, and C. Franchini, Stacking effects on the electronic and optical properties of bilayer transition metal dichalcogenides MoS_2, $MoSe_2$, WS_2, and WSe_2, *Phys. Rev. B* 89(7), 075409 (2014)
69. Q. Liu, L. Li, Y. Li, Z. Gao, Z. Chen, and J. Lu, Tuning electronic structure of bilayer MoS_2 by vertical electric field: A first-principles investigation, *J. Phys. Chem. C* 116(40), 21556 (2012)
70. P. K. Nayak, Y. Horbatenko, S. Ahn, G. Kim, J. U. Lee, K. Y. Ma, A. R. Jang, H. Lim, D. Kim, S. Ryu, H. Cheong, N. Park, and H. S. Shin, Probing evolution of twist-angle-dependent interlayer excitons in $MoSe_2/WSe_2$ van der Waals heterostructures, *ACS Nano* 11(4), 4041 (2017)
71. W. Choi, I. Akhtar, M. A. Rehman, M. Kim, D. Kang, J. Jung, Y. Myung, J. Kim, H. Cheong, and Y. Seo, Twist-angle-dependent optoelectronics in a few-layer transition-metal dichalcogenide heterostructure, *ACS Appl. Mater. Interfaces* 11(2), 2470 (2019)
72. J. Kunstmann, F. Mooshammer, P. Nagler, A. Chaves, F. Stein, N. Paradiso, G. Plechinger, C. Strunk, C. Schüller, G. Seifert, D. R. Reichman, and T. Korn, Momentum-space indirect interlayer excitons in transition-metal dichalcogenide van der Waals heterostructures, *Nat. Phys.* 14(8), 801 (2018)
73. G. Scuri, T. I. Andersen, Y. Zhou, D. S. Wild, J. Sung, R. J. Gelly, D. Bérubé, H. Heo, L. Shao, A. Y. Joe, A. M. Mier Valdivia, T. Taniguchi, K. Watanabe, M. Lončar, P. Kim, M. D. Lukin, and H. Park, Electrically tunable valley dynamics in twisted WSe_2/WSe_2 bilayers, *Phys. Rev. Lett.* 124(21), 217403 (2020)
74. S. Zheng, L. Sun, X. Zhou, F. Liu, Z. Liu, Z. Shen, and H. J. Fan, Coupling and interlayer exciton in twist-stacked WS_2 bilayers, *Adv. Opt. Mater.* 3(11), 1600 (2015)
75. A. A. Puretzky, L. Liang, X. Li, K. Xiao, B. G. Sumpter, V. Meunier, and D. B. Geohegan, Twisted $MoSe_2$ bilayers with variable local stacking and interlayer coupling revealed by low-frequency Raman spectroscopy, *ACS Nano* 10(2), 2736 (2016)
76. J. Zhang, J. Wang, P. Chen, Y. Sun, S. Wu, Z. Jia, X. Lu, H. Yu, W. Chen, J. Zhu, G. Xie, R. Yang, D. Shi, X. Xu, J. Xiang, K. Liu, and G. Zhang, Observation of strong interlayer coupling in MoS_2/WS_2 heterostructures, *Adv. Mater.* 28(10), 1950 (2016)
77. T. Jiang, H. Liu, D. Huang, S. Zhang, Y. Li, X. Gong, Y. R. Shen, W. T. Liu, and S. Wu, Valley and band structure engineering of folded MoS_2 bilayers, *Nat. Nanotechnol.* 9(10), 825 (2014)
78. K. Wang, B. Huang, M. Tian, F. Ceballos, M. W. Lin, M. Mahjouri-Samani, A. Boulesbaa, A. A. Puretzky, C. M. Rouleau, M. Yoon, H. Zhao, K. Xiao, G. Duscher, and D. B. Geohegan, Interlayer coupling in twisted WSe_2/WS_2 bilayer heterostructures revealed by optical spectroscopy, *ACS Nano* 10(7), 6612 (2016)
79. Z. Ji, H. Hong, J. Zhang, Q. Zhang, W. Huang, T. Cao, R. Qiao, C. Liu, J. Liang, C. Jin, L. Jiao, K. Shi, S. Meng, and K. Liu, Robust stacking-independent ultrafast charge transfer in MoS_2/WS_2 bilayers, *ACS Nano* 11(12), 12020 (2017)
80. L. Wu, C. Cong, J. Shang, W. Yang, Y. Chen, J. Zhou, W. Ai, Y. Wang, S. Feng, H. Zhang, Z. Liu, and T. Yu, Raman scattering investigation of twisted WS_2/MoS_2 heterostructures: Interlayer mechanical coupling versus charge transfer, *Nano Res.* 14(7), 2215 (2021)
81. X. Wang, K. Yasuda, Y. Zhang, S. Liu, K. Watanabe, T. Taniguchi, J. Hone, L. Fu, and P. Jarillo-Herrero, Interfacial ferroelectricity in rhombohedral-stacked bilayer transition metal dichalcogenides, *Nat. Nanotechnol.* 17, 367 (2022)
82. J. Sung, Y. Zhou, G. Scuri, V. Zólyomi, T. I. Andersen, H. Yoo, D. S. Wild, A. Y. Joe, R. J. Gelly, H. Heo, S. J. Magorrian, D. Bérubé, A. M. M. Valdivia, T. Taniguchi, K. Watanabe, M. D. Lukin, P. Kim, V. I. Fal'ko, and H. Park, Broken mirror symmetry in excitonic response of reconstructed domains in twisted $MoSe_2/MoSe_2$ bilayers, *Nat. Nanotechnol.* 15(9), 750 (2020)
83. J. Michl, C. C. Palekar, S. A. Tarasenko, F. Lohof, C. Gies, M. von Helversen, R. Sailus, S. Tongay, T. Taniguchi, K. Watanabe, T. Heindel, B. Rosa, M. Rödel, T. Shubina, S. Höfling, S. Reitzenstein, C. Anton-Solanas, and C. Schneider, Intrinsic circularly polarized exciton emission in a twisted van der Waals heterostructure, *Phys. Rev. B* 105(24), L241406 (2022)
84. J. Shi, Y. Li, Z. Zhang, W. Feng, Q. Wang, S. Ren, J. Zhang, W. Du, X. Wu, X. Sui, Y. Mi, R. Wang, Y. Sun, L. Zhang, X. Qiu, J. Lu, C. Shen, Y. Zhang, Q. Zhang, and X. Liu, Twisted-angle-dependent optical behaviors of intralayer excitons and trions in WS_2/WSe_2 heterostructure, *ACS Photonics* 6(12), 3082 (2019)
85. J. E. Zimmermann, M. Axt, F. Mooshammer, P. Nagler, C. Schüller, T. Korn, U. Höfer, and G. Mette, Ultrafast charge-transfer dynamics in twisted MoS_2/WSe_2 heterostructures, *ACS Nano* 15(9), 14725 (2021)
86. D. Luo, J. Tang, X. Shen, F. Ji, J. Yang, S. Weathersby, M. E. Kozina, Z. Chen, J. Xiao, Y. Ye, T. Cao, G. Zhang, X. Wang, and A. M. Lindenberg, Twist-angle-dependent ultrafast charge transfer in MoS_2-graphene van der Waals heterostructures, *Nano Lett.* 21(19), 8051 (2021)
87. A. M. van der Zande, J. Kunstmann, A. Chernikov, D.

A. Chenet, Y. You, X. Zhang, P. Y. Huang, T. C. Berkelbach, L. Wang, F. Zhang, M. S. Hybertsen, D. A. Muller, D. R. Reichman, T. F. Heinz, and J. C. Hone, Tailoring the electronic structure in bilayer molybdenum disulfide via interlayer twist, *Nano Lett.* 14(7), 3869 (2014)

88. S. Huang, X. Ling, L. Liang, J. Kong, H. Terrones, V. Meunier, and M. S. Dresselhaus, Probing the interlayer coupling of twisted bilayer MoS_2 using photoluminescence spectroscopy, *Nano Lett.* 14(10), 5500 (2014)
89. Y. Wang, Z. Su, W. Wu, S. Nie, N. Xie, H. Gong, Y. Guo, J. Hwan Lee, S. Xing, X. Lu, H. Wang, X. Lu, K. McCarty, S. Pei, F. Robles-Hernandez, V. G. Hadjiev, and J. Bao, Resonance Raman spectroscopy of G-line and folded phonons in twisted bilayer graphene with large rotation angles, *Appl. Phys. Lett.* 103(12), 123101 (2013)
90. C. C. Lu, Y. C. Lin, Z. Liu, C. H. Yeh, K. Suenaga, and P. W. Chiu, Twisting bilayer graphene superlattices, *ACS Nano* 7(3), 2587 (2013)
91. W. Ren, J. Chen, and G. Zhang, Phonon physics in twisted two-dimensional materials, *Appl. Phys. Lett.* 121, 140501 (2022)
92. Y. Dai, P. Qi, G. Tao, G. Yao, B. Shi, Z. Liu, Z. Liu, X. He, P. Peng, Z. Dang, L. Zheng, T. Zhang, Y. Gong, Y. Guan, K. Liu, and Z. Fang, Phonon-assisted upconversion in twisted two-dimensional semiconductors, *Light Sci. Appl.* 12(1), 6 (2023)
93. D. Huang, J. Choi, C. K. Shih, and X. Li, Excitons in semiconductor moiré superlattices, *Nat. Nanotechnol.* 17(3), 227 (2022)
94. D. Xiao, G. B. Liu, W. Feng, X. Xu, and W. Yao, Coupled spin and valley physics in monolayers of MoS_2 and other group-VI dichalcogenides, *Phys. Rev. Lett.* 108(19), 196802 (2012)
95. K. F. Mak, K. He, J. Shan, and T. F. Heinz, Control of valley polarization in monolayer MoS_2 by optical helicity, *Nat. Nanotechnol.* 7, 494 (2012)
96. G. Sallen, L. Bouet, X. Marie, G. Wang, C. R. Zhu, W. P. Han, Y. Lu, P. H. Tan, T. Amand, B. L. Liu, and B. Urbaszek, Robust optical emission polarization in MoS_2 monolayers through selective valley excitation, *Phys. Rev. B.* 86(8), 081301 (2012)
97. K. F. Mak, K. L. McGill, J. Park, and P. L. McEuen, The valley Hall effect in MoS_2 transistors, *Science* 344, 1489 (2014)
98. J. Lee, Z. Wang, H. Xie, K. F. Mak, and J. Shan, Valley magnetoelectricity in single-layer MoS_2, *Nat. Mater.* 16, 887 (2017)
99. A. Srivastava, M. Sidler, A. V. Allain, D. S. Lembke, A. Kis, and A. Imamoğlu, Valley Zeeman effect in elementary optical excitations of monolayer WSe_2, *Nat. Phys.* 11(2), 141 (2015)
100. Z. Gong, G. B. Liu, H. Yu, D. Xiao, X. Cui, X. Xu, and W. Yao, Magnetoelectric effects and valley-controlled spin quantum gates in transition metal dichalcogenide bilayers, *Nat. Commun.* 4(1), 2053 (2013)
101. A. Ebnonnasir, B. Narayanan, S. Kodambaka, and C. V. Ciobanu, Tunable MoS_2 bandgap in MoS_2-graphene heterostructures, *Appl. Phys. Lett.* 105, 031603 (2014)
102. P. Rivera, J. R. Schaibley, A. M. Jones, J. S. Ross, S. Wu, G. Aivazian, P. Klement, K. Seyler, G. Clark, N. J. Ghimire, J. Yan, D. G. Mandrus, W. Yao, and X. Xu, Observation of long-lived interlayer excitons in monolayer $MoSe_2$–WSe_2 heterostructures, *Nat. Commun.* 6(1), 6242 (2015)
103. P. Rivera, H. Yu, K. L. Seyler, N. P. Wilson, W. Yao, and X. Xu, Interlayer valley excitons in heterobilayers of transition metal dichalcogenides, *Nat. Nanotechnol.* 13(11), 1004 (2018)
104. J. R. Schaibley, H. Yu, G. Clark, P. Rivera, J. S. Ross, K. L. Seyler, W. Yao, and X. Xu, Valleytronics in 2D materials, *Nat. Rev. Mater.* 1(11), 16055 (2016)
105. K. F. Mak, D. Xiao, and J. Shan, Light–valley interactions in 2D semiconductors, *Nat. Photonics* 12(8), 451 (2018)
106. A. Singh, K. Tran, M. Kolarczik, J. Seifert, Y. Wang, K. Hao, D. Pleskot, N. M. Gabor, S. Helmrich, N. Owschimikow, U. Woggon, and X. Li, Long-lived valley polarization of intravalley trions in monolayer WSe_2, *Phys. Rev. Lett.* 117(25), 257402 (2016)
107. M. Ge, H. Wang, J. Wu, C. Si, J. Zhang, and S. Zhang, Enhanced valley splitting of WSe_2 in twisted van der Waals WSe_2/CrI_3 heterostructures, *npj Comput. Mater.* 8, 32 (2022)
108. W. Hu and J. Yang, Two-dimensional van der Waals heterojunctions for functional materials and devices, *J. Mater. Chem. C* 5(47), 12289 (2017)
109. V. O. Özçelik, J. G. Azadani, C. Yang, S. J. Koester, and T. Low, Band alignment of two-dimensional semiconductors for designing heterostructures with momentum space matching, *Phys. Rev. B* 94(3), 035125 (2016)
110. X. Hong, J. Kim, S. F. Shi, Y. Zhang, C. Jin, Y. Sun, S. Tongay, J. Wu, Y. Zhang, and F. Wang, Ultrafast charge transfer in atomically thin MoS_2/WS_2 heterostructures, *Nat. Nanotechnol.* 9(9), 682 (2014)
111. H. Zhu, J. Wang, Z. Gong, Y. D. Kim, J. Hone, and X. Y. Zhu, Interfacial charge transfer circumventing momentum mismatch at two-dimensional van der Waals heterojunctions, *Nano Lett.* 17(6), 3591 (2017)
112. A. F. Rigosi, H. M. Hill, Y. Li, A. Chernikov, and T. F. Heinz, Probing interlayer interactions in transition metal dichalcogenide heterostructures by optical spectroscopy: MoS_2/WS_2 and $MoSe_2/WSe_2$, *Nano Lett.* 15(8), 5033 (2015)
113. Y. Yu, S. Hu, L. Su, L. Huang, Y. Liu, Z. Jin, A. A. Purezky, D. B. Geohegan, K. W. Kim, Y. Zhang, and L. Cao, Equally efficient interlayer exciton relaxation and improved absorption in epitaxial and nonepitaxial MoS_2/WS_2 heterostructures, *Nano Lett.* 15(1), 486 (2015)
114. F. Liu, Q. Li, and X. Y. Zhu, Direct determination of momentum-resolved electron transfer in the photoexcited van der Waals heterobilayer WS_2/MoS_2, *Phys. Rev. B* 101(20), 201405 (2020)
115. P. Merkl, F. Mooshammer, P. Steinleitner, A. Girnghuber, K. Q. Lin, P. Nagler, J. Holler, C. Schüller, J. M. Lupton, T. Korn, S. Ovesen, S. Brem, E. Malic, and R. Huber, Ultrafast transition between exciton phases in van der Waals heterostructures, *Nat.*

Mater. 18(7), 691 (2019)
116. H. Wang, J. Bang, Y. Sun, L. Liang, D. West, V. Meunier, and S. Zhang, The role of collective motion in the ultrafast charge transfer in van der Waals heterostructures, *Nat. Commun.* 7(1), 11504 (2016)
117. S. K. Behura, A. Miranda, S. Nayak, K. Johnson, P. Das, and N. R. Pradhan, Moiré physics in twisted van der Waals heterostructures of 2D materials, *Emergent Mater.* 4(4), 813 (2021)
118. F. Wu, T. Lovorn, E. Tutuc, and A. H. MacDonald, Hubbard model physics in transition metal dichalcogenide moiré bands, *Phys. Rev. Lett.* 121(2), 026402 (2018)
119. H. Wang, S. Ma, S. Zhang, and D. Lei, Intrinsic superflat bands in general twisted bilayer systems, *Light Sci. Appl.* 11(1), 159 (2022)
120. Z. Ma, S. Li, M. M. Xiao, Y. W. Zheng, M. Lu, H. Liu, J. H. Gao, and X. C. Xie, Moiré flat bands of twisted few-layer graphite, *Front. Phys.* 18(1), 13307 (2023)
121. N. Zhang, A. Surrente, M. Baranowski, D. K. Maude, P. Gant, A. Castellanos-Gomez, and P. Plochocka, Moiré intralayer excitons in a $MoSe_2/MoS_2$ heterostructure, *Nano Lett.* 18(12), 7651 (2018)
122. B. Remez and N. R. Cooper, Leaky exciton condensates in transition metal dichalcogenide moiré bilayers, *Phys. Rev. Mater.* 4, L022042 (2022)
123. R. Bistritzer and A. H. MacDonald, Moiré bands in twisted double-layer graphene, *Proc. Natl. Acad. Sci. USA* 108(30), 12233 (2011)
124. G. Chen, L. Jiang, S. Wu, B. Lyu, H. Li, B. L. Chittari, K. Watanabe, T. Taniguchi, Z. Shi, J. Jung, Y. Zhang, and F. Wang, Evidence of a gate-tunable Mott insulator in a trilayer graphene moiré superlattice, *Nat. Phys.* 15(3), 237 (2019)
125. G. Chen, A. L. Sharpe, P. Gallagher, I. T. Rosen, E. J. Fox, L. Jiang, B. Lyu, H. Li, K. Watanabe, T. Taniguchi, J. Jung, Z. Shi, D. Goldhaber-Gordon, Y. Zhang, and F. Wang, Signatures of tunable superconductivity in a trilayer graphene moiré superlattice, *Nature* 572(7768), 215 (2019)
126. G. Chen, A. L. Sharpe, E. J. Fox, Y. H. Zhang, S. Wang, L. Jiang, B. Lyu, H. Li, K. Watanabe, T. Taniguchi, Z. Shi, T. Senthil, D. Goldhaber-Gordon, Y. Zhang, and F. Wang, Tunable correlated Chern insulator and ferromagnetism in a moiré superlattice, *Nature* 579(7797), 56 (2020)
127. R. Su, M. Kuiri, K. Watanabe, T. Taniguchi, and J. Folk, Superconductivity in twisted double bilayer graphene stabilized by WSe_2, *Nat. Mater.* 22(11), 1332 (2023)
128. L. Wang, E. M. Shih, A. Ghiotto, L. Xian, D. A. Rhodes, C. Tan, M. Claassen, D. M. Kennes, Y. Bai, B. Kim, K. Watanabe, T. Taniguchi, X. Zhu, J. Hone, A. Rubio, A. N. Pasupathy, and C. R. Dean, Correlated electronic phases in twisted bilayer transition metal dichalcogenides, *Nat. Mater.* 19(8), 861 (2020)
129. Y. Tang, L. Li, T. Li, Y. Xu, S. Liu, K. Barmak, K. Watanabe, T. Taniguchi, A. H. MacDonald, J. Shan, and K. F. Mak, Simulation of Hubbard model physics in WSe_2/WS_2 moiré superlattices, *Nature* 579(7799), 353 (2020)
130. Y. Xu, S. Liu, D. A. Rhodes, K. Watanabe, T. Taniguchi, J. Hone, V. Elser, K. F. Mak, and J. Shan, Correlated insulating states at fractional fillings of moiré superlattices, *Nature* 587(7833), 214 (2020)
131. Y. Shimazaki, I. Schwartz, K. Watanabe, T. Taniguchi, M. Kroner, and A. Imamoğlu, Strongly correlated electrons and hybrid excitons in a moiré heterostructure, *Nature* 580(7804), 472 (2020)
132. Y. Liu, C. Zeng, J. Yu, J. Zhong, B. Li, Z. Zhang, Z. Liu, Z. M. Wang, A. Pan, and X. Duan, Moiré superlattices and related moiré excitons in twisted van der Waals heterostructures, *Chem. Soc. Rev.* 50(11), 6401 (2021)
133. M. H. Naik, S. Kundu, I. Maity, and M. Jain, Origin and evolution of ultraflat bands in twisted bilayer transition metal dichalcogenides: Realization of triangular quantum dots, *Phys. Rev. B* 102(7), 075413 (2020)
134. L. Yuan, B. Zheng, J. Kunstmann, T. Brumme, A. B. Kuc, C. Ma, S. Deng, D. Blach, A. Pan, and L. Huang, Twist-angle-dependent interlayer exciton diffusion in WS_2–WSe_2 heterobilayers, *Nat. Mater.* 19(6), 617 (2020)
135. L. Zhang, Z. Zhang, F. Wu, D. Wang, R. Gogna, S. Hou, K. Watanabe, T. Taniguchi, K. Kulkarni, T. Kuo, S. R. Forrest, and H. Deng, Twist-angle dependence of moiré excitons in $WS_2/MoSe_2$ heterobilayers, *Nat. Commun.* 11(1), 5888 (2020)
136. Z. Li, X. Lu, D. F. Cordovilla Leon, Z. Lyu, H. Xie, J. Hou, Y. Lu, X. Guo, A. Kaczmarek, T. Taniguchi, K. Watanabe, L. Zhao, L. Yang, and P. B. Deotare, Interlayer exciton transport in $MoSe_2/WSe_2$ heterostructures, *ACS Nano* 15(1), 1539 (2021)
137. X. Zhao, J. Qiao, X. Zhou, H. Chen, J. Y. Tan, H. Yu, S. M. Chan, J. Li, H. Zhang, J. Zhou, J. Dan, Z. Liu, W. Zhou, Z. Liu, B. Peng, L. Deng, S. J. Pennycook, S. Y. Quek, and K. P. Loh, Strong moiré excitons in high-angle twisted transition metal dichalcogenide homobilayers with robust commensuration, *Nano Lett.* 22(1), 203 (2022)
138. R. Ribeiro-Palau, C. Zhang, K. Watanabe, T. Taniguchi, J. Hone, and C. R. Dean, Twistable electronics with dynamically rotatable heterostructures, *Science* 361(6403), 690 (2018)
139. A. Weston, Y. Zou, V. Enaldiev, A. Summerfield, N. Clark, V. Zólyomi, A. Graham, C. Yelgel, S. Magorrian, M. Zhou, J. Zultak, D. Hopkinson, A. Barinov, T. H. Bointon, A. Kretinin, N. R. Wilson, P. H. Beton, V. I. Fal'ko, S. J. Haigh, and R. Gorbachev, Atomic reconstruction in twisted bilayers of transition metal dichalcogenides, *Nat. Nanotechnol.* 15(7), 592 (2020)
140. M. R. Rosenberger, H. J. Chuang, M. Phillips, V. P. Oleshko, K. M. McCreary, S. V. Sivaram, C. S. Hellberg, and B. T. Jonker, Twist angle-dependent atomic reconstruction and moiré patterns in transition metal dichalcogenide heterostructures, *ACS Nano* 14(4), 4550 (2020)
141. T. I. Andersen, G. Scuri, A. Sushko, K. De Greve, J. Sung, Y. Zhou, D. S. Wild, R. J. Gelly, H. Heo, D. Bérubé, A. Y. Joe, L. A. Jauregui, K. Watanabe, T. Taniguchi, P. Kim, H. Park, and M. D. Lukin, Excitons in a reconstructed moiré potential in twisted WSe_2/WSe_2 homobilayers, *Nat. Mater.* 20(4), 480 (2021)

142. J. Quan, L. Linhart, M. L. Lin, D. Lee, J. Zhu, C. Y. Wang, W. T. Hsu, J. Choi, J. Embley, C. Young, T. Taniguchi, K. Watanabe, C. K. Shih, K. Lai, A. H. MacDonald, P. H. Tan, F. Libisch, and X. Li, Phonon renormalization in reconstructed MoS_2 moiré superlattices, *Nat. Mater.* 20(8), 1100 (2021)
143. B. H. Lin, Y. C. Chao, I. T. Hsieh, C. P. Chuu, C. J. Lee, F. H. Chu, L. S. Lu, W. T. Hsu, C. W. Pao, C. K. Shih, J. J. Su, and W. H. Chang, Remarkably deep moiré potential for intralayer excitons in $MoSe_2/MoS_2$ twisted heterobilayers, *Nano Lett.* 23(4), 1306 (2023)
144. S. Li, H. Zheng, J. Ding, B. Wu, J. He, Z. Liu, and Y. Liu, Dynamic control of moiré potential in twisted WS_2–WSe_2 heterostructures, *Nano Res.* 15(8), 7688 (2022)
145. B. Wu, H. Zheng, S. Li, J. Ding, Y. Zeng, Z. Liu, and Y. Liu, Observation of moiré excitons in the twisted WS_2/WS_2 homostructure, *Nanoscale* 14(34), 12447 (2022)
146. E. M. Alexeev, D. A. Ruiz-Tijerina, M. Danovich, M. J. Hamer, D. J. Terry, P. K. Nayak, S. Ahn, S. Pak, J. Lee, J. I. Sohn, M. R. Molas, M. Koperski, K. Watanabe, T. Taniguchi, K. S. Novoselov, R. V. Gorbachev, H. S. Shin, V. I. Fal'ko, and A. I. Tartakovskii, Resonantly hybridized excitons in moiré superlattices in van der Waals heterostructures, *Nature* 567(7746), 81 (2019)
147. K. Tran, G. Moody, F. Wu, X. Lu, J. Choi, K. Kim, A. Rai, D. A. Sanchez, J. Quan, A. Singh, J. Embley, A. Zepeda, M. Campbell, T. Autry, T. Taniguchi, K. Watanabe, N. Lu, S. K. Banerjee, K. L. Silverman, S. Kim, E. Tutuc, L. Yang, A. H. MacDonald, and X. Li, Evidence for moiré excitons in van der Waals heterostructures, *Nature* 567(7746), 71 (2019)
148. Y. Tang, J. Gu, S. Liu, K. Watanabe, T. Taniguchi, J. Hone, K. F. Mak, and J. Shan, Tuning layer-hybridized moiré excitons by the quantum-confined Stark effect, *Nat. Nanotechnol.* 16(1), 52 (2021)
149. S. Brem, K. Q. Lin, R. Gillen, J. M. Bauer, J. Maultzsch, J. M. Lupton, and E. Malic, Hybridized intervalley moiré excitons and flat bands in twisted WSe_2 bilayers, *Nanoscale* 12, 11088 (2020)
150. D. A. Ruiz-Tijerina and V. I. Fal'ko, Interlayer hybridization and moiré superlattice minibands for electrons and excitons in heterobilayers of transition-metal dichalcogenides, *Phys. Rev. B* 99(12), 125424 (2019)
151. C. Jin, E. C. Regan, A. Yan, M. Iqbal Bakti Utama, D. Wang, S. Zhao, Y. Qin, S. Yang, Z. Zheng, S. Shi, K. Watanabe, T. Taniguchi, S. Tongay, A. Zettl, and F. Wang, Observation of moiré excitons in WSe_2/WS_2 heterostructure superlattices, *Nature* 567(7746), 76 (2019)
152. H. Zheng, B. Wu, S. Li, J. He, K. Chen, Z. Liu and Y. Liu. Evidence for interlayer coupling and moiré excitons in twisted WS_2/WS_2 homostructure superlattices. *Nano Res.* 16(2), 3429 (2023)
153. O. Karni, E. Barré, V. Pareek, J. D. Georgaras, M. K. L. Man, C. Sahoo, D. R. Bacon, X. Zhu, H. B. Ribeiro, A. L. O'Beirne, J. Hu, A. Al-Mahboob, M. M. M. Abdelrasoul, N. S. Chan, A. Karmakar, A. J. Winchester, B. Kim, K. Watanabe, T. Taniguchi, K. Barmak, J. Madéo, F. H. da Jornada, T. F. Heinz, and K. M. Dani, Structure of the moiré exciton captured by imaging its electron and hole, *Nature* 603(7900), 247 (2022)
154. M. Dandu, G. Gupta, P. Dasika, K. Watanabe, T. Taniguchi, and K. Majumdar, Electrically tunable localized versus delocalized intralayer moiré excitons and trions in a twisted MoS_2 bilayer, *ACS Nano* 16(6), 8983 (2022)
155. S. Brem and E. Malic, Bosonic delocalization of dipolar moiré excitons, *Nano Lett.* 23(10), 4627 (2023)
156. C. Lagoin and F. Dubin, Key role of the moiré potential for the quasicondensation of interlayer excitons in van der Waals heterostructures, *Phys. Rev. B* 103(4), L041406 (2021)
157. N. Götting, F. Lohof, and C. Gies, Moiré-Bose-Hubbard model for interlayer excitons in twisted transition metal dichalcogenide heterostructures, *Phys. Rev. B* 105(16), 165419 (2022)
158. J. Choi, W. T. Hsu, L. S. Lu, L. Sun, H. Y. Cheng, M. H. Lee, J. Quan, K. Tran, C. Y. Wang, M. Staab, K. Jones, T. Taniguchi, K. Watanabe, M. W. Chu, S. Gwo, S. Kim, C. K. Shih, X. Li, and W. H. Chang, Moiré potential impedes interlayer exciton diffusion in van der Waals heterostructures, *Sci. Adv.* 6(39), eaba8866 (2020)
159. F. Mahdikhanysarvejahany, D. N. Shanks, C. Muccianti, B. H. Badada, I. Idi, A. Alfrey, S. Raglow, M. R. Koehler, D. G. Mandrus, T. Taniguchi, K. Watanabe, O. L. A. Monti, H. Yu, B. J. LeRoy, and J. R. Schaibley, Temperature dependent moiré trapping of interlayer excitons in $MoSe_2$–WSe_2 heterostructures, *npj 2D Mater. Appl.* 5, 67 (2021)
160. J. Choi, M. Florian, A. Steinhoff, D. Erben, K. Tran, D. S. Kim, L. Sun, J. Quan, R. Claassen, S. Majumder, J. A. Hollingsworth, T. Taniguchi, K. Watanabe, K. Ueno, A. Singh, G. Moody, F. Jahnke, and X. Li, Twist angle-dependent interlayer exciton lifetimes in van der Waals heterostructures, *Phys. Rev. Lett.* 126(4), 047401 (2021)
161. H. Cai, A. Rasmita, Q. Tan, J. M. Lai, R. He, X. Cai, Y. Zhao, D. Chen, N. Wang, Z. Mu, Z. Huang, Z. Zhang, J. J. H. Eng, Y. Liu, Y. She, N. Pan, Y. Miao, X. Wang, X. Liu, J. Zhang, and W. Gao, Interlayer donor-acceptor pair excitons in $MoSe_2/WSe_2$ moiré heterobilayer, *Nat. Commun.* 14(1), 5766 (2023)
162. H. Zheng, B. Wu, C. T. Wang, S. Li, J. He, Z. Liu, J. T. Wang, J. Duan, and Y. Liu, Exploring the regulatory effect of stacked layers on moiré excitons in twisted $WSe_2/WSe_2/WSe_2$ homotrilayer, *Nano Res.* 16(7), 10573 (2023)
163. H. Zheng, B. Wu, S. Li, J. Ding, J. He, Z. Liu, C. T. Wang, J. T. Wang, A. Pan, and Y. Liu, Localization-enhanced moiré exciton in twisted transition metal dichalcogenide heterotrilayer superlattices, *Light Sci. Appl.* 12(1), 117 (2023)
164. L. Zhang, R. Gogna, G. W. Burg, J. Horng, E. Paik, Y. H. Chou, K. Kim, E. Tutuc, and H. Deng, Highly valley-polarized singlet and triplet interlayer excitons in van der Waals heterostructure, *Phys. Rev. B* 100(4), 041402 (2019)
165. M. Brotons-Gisbert, H. Baek, A. Molina-Sánchez, A. Campbell, E. Scerri, D. White, K. Watanabe, T.

Taniguchi, C. Bonato, and B. D. Gerardot, Spin-layer locking of interlayer excitons trapped in moiré potentials, *Nat. Mater.* 19(6), 630 (2020)

166. X. Wang, J. Zhu, K. L. Seyler, P. Rivera, H. Zheng, Y. Wang, M. He, T. Taniguchi, K. Watanabe, J. Yan, D. G. Mandrus, D. R. Gamelin, W. Yao, and X. Xu, Moiré trions in $MoSe_2/WSe_2$ heterobilayers, *Nat. Nanotechnol.* 16(11), 1208 (2021)
167. Y. Bai, L. Zhou, J. Wang, W. Wu, L. J. McGilly, D. Halbertal, C. F. B. Lo, F. Liu, J. Ardelean, P. Rivera, N. R. Finney, X. C. Yang, D. N. Basov, W. Yao, X. Xu, J. Hone, A. N. Pasupathy, and X. Y. Zhu, Excitons in strain-induced one-dimensional moiré potentials at transition metal dichalcogenide heterojunctions, *Nat. Mater.* 19(10), 1068 (2020)
168. W. Zhao, E. C. Regan, D. Wang, C. Jin, S. Hsieh, Z. Wang, J. Wang, Z. Wang, K. Yumigeta, M. Blei, K. Watanabe, T. Taniguchi, S. Tongay, N. Y. Yao, and F. Wang, Dynamic tuning of moiré excitons in a WSe_2/WS_2 heterostructure via mechanical deformation, *Nano Lett.* 21(20), 8910 (2021)
169. M. Anđelković, S. P. Milovanović, L. Covaci, and F. M. Peeters, Double moiré with a twist: Supermoiré in encapsulated graphene, *Nano Lett.* 20(2), 979 (2020)
170. F. Tagarelli, E. Lopriore, D. Erkensten, R. Perea-Causín, S. Brem, J. Hagel, Z. Sun, G. Pasquale, K. Watanabe, T. Taniguchi, E. Malic, and A. Kis, Electrical control of hybrid exciton transport in a van der Waals heterostructure, *Nat. Photonics* 17(7), 615 (2023)
171. Z. Lian, D. Chen, Y. Meng, X. Chen, Y. Su, R. Banerjee, T. Taniguchi, K. Watanabe, S. Tongay, C. Zhang, Y. T. Cui, and S. F. Shi, Exciton superposition across moiré states in a semiconducting moiré superlattice, *Nat. Commun.* 14(1), 5042 (2023)
172. L. Li and M. Wu, Binary compound bilayer and multilayer with vertical polarizations: Two-dimensional ferroelectrics, multiferroics, and nanogenerators, *ACS Nano* 11(6), 6382 (2017)
173. F. Li, J. Fu, M. Xue, Y. Li, H. Zeng, E. Kan, T. Hu, and Y. Wan, Room-temperature vertical ferroelectricity in rhenium diselenide induced by interlayer sliding, *Front. Phys.* 18(5), 53305 (2023)
174. Y. Wang, C. Cong, W. Yang, J. Shang, N. Peimyoo, Y. Chen, J. Kang, J. Wang, W. Huang, and T. Yu, Strain-induced direct–indirect bandgap transition and phonon modulation in monolayer WS_2, *Nano Res.* 8(8), 2562 (2015)
175. X. He, H. Li, Z. Zhu, Z. Dai, Y. Yang, P. Yang, Q. Zhang, P. Li, U. Schwingenschlogl, and X. Zhang, Strain engineering in monolayer WS_2, MoS_2, and the WS_2/MoS_2 heterostructure, *Appl. Phys. Lett.* 109(17), 173105 (2016)
176. J. Feng, X. Qian, C. W. Huang, and J. Li, Strain-engineered artificial atom as a broad-spectrum solar energy funnel, *Nat. Photonics* 6(12), 866 (2012)
177. A. Castellanos-Gomez, R. Roldán, E. Cappelluti, M. Buscema, F. Guinea, H. S. J. van der Zant, and G. A. Steele, Local strain engineering in atomically thin MoS_2, *Nano Lett.* 13(11), 5361 (2013)
178. W. Wang and X. Ma, Strain-induced trapping of indirect excitons in $MoSe_2/WSe_2$ heterostructures, *ACS Photon.* 7, 2460 (2020)
179. X. Liu and J. Zeng, Gap solitons in parity–time symmetric moiré optical lattices, *Photon. Res.* 11(2), 196 (2023)
180. Y. Liu, C. Ouyang, Q. Xu, X. Su, Q. Yang, J. Ma, Y. Li, Z. Tian, J. Gu, L. Liu, J. Han, Y. Shi, and W. Zhang, Moiré-driven electromagnetic responses and magic angles in a sandwiched hyperbolic metasurface, *Photon. Res.* 10(9), 2056 (2022)
181. E. C. Regan, D. Wang, C. Jin, M. I. Bakti Utama, B. Gao, X. Wei, S. Zhao, W. Zhao, Z. Zhang, K. Yumigeta, M. Blei, J. D. Carlström, K. Watanabe, T. Taniguchi, S. Tongay, M. Crommie, A. Zettl, and F. Wang, Mott and generalized Wigner crystal states in WSe_2/WS_2 moiré superlattices, *Nature* 579(7799), 359 (2020)
182. J. G. Bednorz and K. A. Müller, Possible high T_c superconductivity in the Ba–La–Cu–O system, *Zeitschrift für Physik B Condensed Matter* 64, 189 (1986)
183. T. Li, S. Jiang, L. Li, Y. Zhang, K. Kang, J. Zhu, K. Watanabe, T. Taniguchi, D. Chowdhury, L. Fu, J. Shan, and K. F. Mak, Continuous Mott transition in semiconductor moiré superlattices, *Nature* 597(7876), 350 (2021)
184. S. Miao, T. Wang, X. Huang, D. Chen, Z. Lian, C. Wang, M. Blei, T. Taniguchi, K. Watanabe, S. Tongay, Z. Wang, D. Xiao, Y. T. Cui, and S. F. Shi, Strong interaction between interlayer excitons and correlated electrons in WSe_2/WS_2 moiré superlattice, *Nat. Commun.* 12(1), 3608 (2021)
185. D. Chen, Z. Lian, X. Huang, Y. Su, M. Rashetnia, L. Yan, M. Blei, T. Taniguchi, K. Watanabe, S. Tongay, Z. Wang, C. Zhang, Y. T. Cui, and S. F. Shi, Tuning moiré excitons and correlated electronic states through layer degree of freedom, *Nat. Commun.* 13(1), 4810 (2022)
186. M. H. Naik, E. C. Regan, Z. Zhang, Y. H. Chan, Z. Li, D. Wang, Y. Yoon, C. S. Ong, W. Zhao, S. Zhao, M. I. B. Utama, B. Gao, X. Wei, M. Sayyad, K. Yumigeta, K. Watanabe, T. Taniguchi, S. Tongay, F. H. da Jornada, F. Wang, and S. G. Louie, Intralayer charge-transfer moiré excitons in van der Waals superlattices, *Nature* 609(7925), 52 (2022)
187. X. Wang, C. Xiao, H. Park, J. Zhu, C. Wang, T. Taniguchi, K. Watanabe, J. Yan, D. Xiao, D. R. Gamelin, W. Yao, and X. Xu, Light-induced ferromagnetism in moiré superlattices, *Nature* 604(7906), 468 (2022)
188. Z. Zhang, E. C. Regan, D. Wang, W. Zhao, S. Wang, M. Sayyad, K. Yumigeta, K. Watanabe, T. Taniguchi, S. Tongay, M. Crommie, A. Zettl, M. P. Zaletel, and F. Wang, Correlated interlayer exciton insulator in heterostructures of monolayer WSe_2 and moiré WS_2/WSe_2, *Nat. Phys.* 18(10), 1214 (2022)
189. G. Rohringer, H. Hafermann, A. Toschi, A. A. Katanin, A. E. Antipov, M. I. Katsnelson, A. I. Lichtenstein, A. N. Rubtsov, and K. Held, Diagrammatic routes to nonlocal correlations beyond dynamical mean field theory, *Rev. Mod. Phys.* 90(2), 025003 (2018)
190. J. Quintanilla and C. A. Hooley, The strong-correlations

puzzle, *Physics World* 22(06), 32 (2009)
191. A. Ghiotto, E. M. Shih, G. S. S. G. Pereira, D. A. Rhodes, B. Kim, J. Zang, A. J. Millis, K. Watanabe, T. Taniguchi, J. C. Hone, L. Wang, C. R. Dean, and A. N. Pasupathy, Quantum criticality in twisted transition metal dichalcogenides, *Nature* 597(7876), 345 (2021)
192. A. Szasz, J. Motruk, M. P. Zaletel, and J. E. Moore, Chiral spin liquid phase of the triangular lattice Hubbard model: A density matrix renormalization group study, *Phys. Rev. X* 10(2), 021042 (2020)
193. T. Senthil, Theory of a continuous Mott transition in two dimensions, *Phys. Rev. B* 78(4), 045109 (2008)
194. M. Imada, A. Fujimori, and Y. Tokura, Metal–insulator transitions, *Rev. Mod. Phys.* 70(4), 1039 (1998)
195. A. M. Jones, H. Yu, J. S. Ross, P. Klement, N. J. Ghimire, J. Yan, D. G. Mandrus, W. Yao, and X. Xu, Spin–layer locking effects in optical orientation of exciton spin in bilayer WSe_2, *Nat. Phys.* 10(2), 130 (2014)
196. R. Xiong, J. Nie, S. Brantly, P. Hays, R. Sailus, K. Watanabe, T. Taniguchi, S. Tongay, and C. Jin, Correlated insulator of excitons in WSe_2/WS_2 moiré superlattices, *Science* 380(6647), 860 (2023)
197. S. Brem, C. Linderälv, P. Erhart, and E. Malic, Tunable phases of moiré excitons in van der Waals heterostructures, *Nano Lett.* 20(12), 8534 (2020)
198. Z. Zhang, Y. Wang, K. Watanabe, T. Taniguchi, K. Ueno, E. Tutuc, and B. J. LeRoy, Flat bands in twisted bilayer transition metal dichalcogenides, *Nat. Phys.* 16(11), 1093 (2020)
199. Q. Hu, Z. Zhan, H. Cui, Y. Zhang, F. Jin, X. Zhao, M. Zhang, Z. Wang, Q. Zhang, K. Watanabe, T. Taniguchi, X. Cao, W. M. Liu, F. Wu, S. Yuan, and Y. Xu, Observation of Rydberg moiré excitons, *Science* 380(6652), 1367 (2023)
200. Q. Tan, A. Rasmita, Z. Zhang, K. S. Novoselov, and W. Gao, Signature of cascade transitions between interlayer excitons in a moiré superlattice, *Phys. Rev. Lett.* 129(24), 247401 (2022)
201. D. Halbertal, N. R. Finney, S. S. Sunku, A. Kerelsky, C. Rubio-Verdú, S. Shabani, L. Xian, S. Carr, S. Chen, C. Zhang, L. Wang, D. Gonzalez-Acevedo, A. S. McLeod, D. Rhodes, K. Watanabe, T. Taniguchi, E. Kaxiras, C. R. Dean, J. C. Hone, A. N. Pasupathy, D. M. Kennes, A. Rubio, and D. N. Basov, Moiré metrology of energy landscapes in van der Waals heterostructures, *Nat. Commun.* 12(1), 242 (2021)
202. H. Li, S. Li, E. C. Regan, D. Wang, W. Zhao, S. Kahn, K. Yumigeta, M. Blei, T. Taniguchi, K. Watanabe, S. Tongay, A. Zettl, M. F. Crommie, and F. Wang, Imaging two-dimensional generalized Wigner crystals, *Nature* 597(7878), 650 (2021)
203. C. H. Stansbury, M. I. B. Utama, C. G. Fatuzzo, E. C. Regan, D. Wang, Z. Xiang, M. Ding, K. Watanabe, T. Taniguchi, M. Blei, Y. Shen, S. Lorcy, A. Bostwick, C. Jozwiak, R. Koch, S. Tongay, J. Avila, E. Rotenberg, F. Wang, and A. Lanzara, Visualizing electron localization of WS_2/WSe_2 moiré superlattices in momentum space, *Sci. Adv.* 7(37), eabf4387 (2021)
204. Y. Z. Chen, S. G. Yu, T. Jiang, X. J. Liu, X. B. Cheng, and D. Huang, Optical two-dimensional coherent spectroscopy of excitons in transition-metal dichalcogenides, *Front. Phys.* 19, 23301 (2024)
205. V. V. Enaldiev, F. Ferreira, S. J. Magorrian, and V. I. Fal'ko, Piezoelectric networks and ferroelectric domains in twistronic superlattices in WS_2/MoS_2 and $WSe_2/MoSe_2$ bilayers, *2D Mater.* 8, 025030 (2021)
206. F. Xiao, K. Chen, and Q. Tong, Magnetization textures in twisted bilayer CrX_3 (X = Br, I), *Phys. Rev. Research.* 3, 013027 (2021)